MODELING, CONTROL, AND DESIGN OF HYBRID ELECTRICAL AND THERMAL
ENERGY STORAGE SYSTEMS

BY

CARY LAIRD

THESIS

Submitted in partial fulfillment of the requirements
for the degree of Master of Science in Mechanical Engineering
in the Graduate College of the
University of Illinois at Urbana-Champaign, 2021

Urbana, Illinois

Adviser:

Professor Andrew Alleyne

ABSTRACT

Advances in power density, energy storage technology, and thermal management are crucial to the increased electrification of vehicles, including those with high ramp rate loads such as heavy construction and military vehicles. In this thesis, a hybrid electro-thermal energy storage system is introduced which offers a power-dense electro-thermal energy storage solution for future electrified vehicles. This energy storage system includes energy-dense batteries and power-dense ultracapacitors for electrical energy storage, and phase change material thermal energy storage modules and coolant loops for thermal energy storage. Multi-domain graph-based modeling techniques are used to facilitate modeling, control, and design optimization of the energy storage system. Graph-based models capture multi-domain dynamics in a unified framework. A heuristic control strategy is used, which seeks to protect the energy storage elements while maintaining reference signals. Sizing and control parameters of the electro-thermal energy storage system are optimized using a graph-based optimization framework. Optimized designs demonstrate significant reductions in size while retaining a high level of performance, leading to improvements in power density. A multi-domain optimization formulation is compared to optimization subroutines which individually optimize parameters pertaining to the electrical and thermal domains. Additionally, the multi-domain sizing and control optimization study is compared to a similar study in which the control parameters are not optimized. The results accentuate the importance of considering multi-domain dynamics as well as control in the design process for dynamic systems.

ACKNOWLEDGMENTS

This thesis would not have been possible without the help of my mentors, colleagues, family, and friends. I am immensely grateful to the following individuals for their guidance and support.

First, I want to thank my adviser, Professor Andrew Alleyne, for his instruction, guidance, support, and encouragement. Thank you for prioritizing your students and for being so strongly committed to our professional and personal development. I'm so glad to have such a helpful and understanding adviser and I thank you for the tremendous impact you've already had on my development as a researcher.

I'm blessed to have a very supportive family who has provided me with a strong foundation for success and molded me into the person I am today. My biggest supporters have always been my parents and I can't thank them enough for giving me the resources and upbringing to be successful. I'm deeply grateful for your encouragement to further my education. Thank you for instilling in me an appreciation for hard work, for taking pride in what I do, and for pushing me to be the best person I can be.

I'm also very grateful for the support of my undergraduate research advisors and mentors, Dr. Richard Williams, Professor Nicholas Giordano, and Dr. Thomas Burch. Thanks for inspiring me to pursue graduate school and for all the help you provided along the way.

To my colleagues in the Alleyne Research Group, I am so grateful for your mentorship, research insights, and friendship. To senior and former lab members Herschel, Donald, Chris A., Spencer, and Pamela, thank you for ramping up my trajectory as a researcher early on by teaching and mentoring me. In addition to these folks, I want to thank Ashley, Oyuna, Mindy, Frank, Reid,

Phil, Kayla, Chris U., Dylan, and Kurt, for their friendship and support. It's been a joy to work with you all in the Alleyne Research Group and I look forward to more collaboration and transformative research in the future.

I would also like to thank the faculty, staff, and students of the Center for Power Optimization of Electro-Thermal Systems. Getting to work with you all has been an incredible experience that has made a huge impact on my research and professional development. I would especially like to thank Jodi Gritten for always brightening up the office (or Skype call) with your smile and positive attitude.

I am so grateful to my husband, Austin, for his steadfast support, encouragement, and love. Thank you for making me laugh when I don't feel like it, and for being my rock when I feel stressed and anxious. I can't imagine going through grad school without you by my side, and I am so thankful that I don't have to. I love you.

To my family, friends, and teachers

TABLE OF CONTENTS

LIST OF FIGURES

LIST OF TABLES

CHAPTER 1. INTRODUCTION

1.1 Background

In response to worldwide concerns about climate change and air quality, governments across the globe are striving to reduce environmental hazards by introducing and strengthening regulations for vehicle emissions. With some countries targeting net-zero greenhouse gas emissions in the next few decades [1], [2], these regulations have led to rapid growth of electrified vehicle industries. Between 2010 and 2019, the number of battery electric vehicles worldwide increased from 0.02 million to 4.79 million [3], as shown in Figure 1.1. Other segments of the electrified mobility market, such as hybrid vehicles, light commercial vehicles, electric buses, construction vehicles, ships, and aircraft, have also experienced a marked increase.
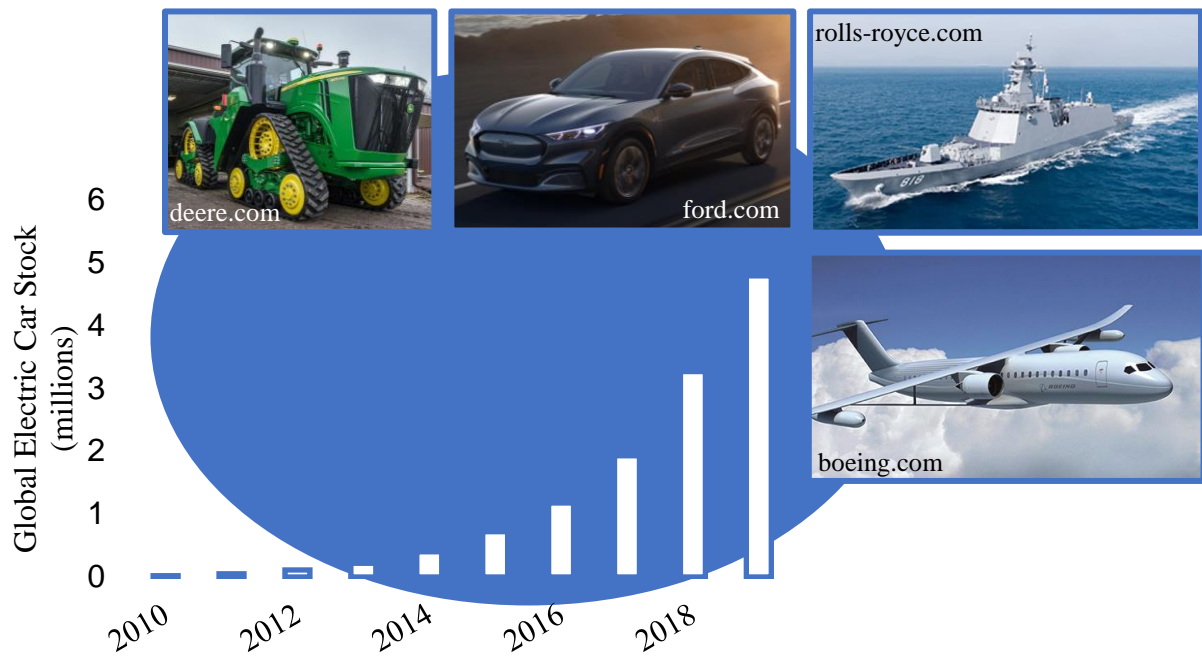
Figure 1.1: Electrified vehicle stock (data from [3]**) and applications.**

However, the fledgling electric vehicle industry is plagued by several challenges that have hindered the widespread adoption of electric vehicles. One of the most prominent of these challenges is the need for increased power density by nearly an order of magnitude [4] in order for electrified vehicles to achieve sustained success. In a similar vein, the shortcomings of batteries as the prime energy source present another significant hurdle towards widespread electric vehicle adoption. Particularly, vehicle range and battery lifetime are reported among the primary areas of concern for potential EV buyers [5]. While range is determined largely by battery energy density, battery lifetime is influenced by several factors, such as the magnitude of instantaneous power drawn by the battery and battery operating temperature [6]. Due to their relatively low power density, batteries can be damaged by high discharge rates, resulting in reduced lifetimes. However, the successful operation of many vehicles, such as city buses and heavy-duty construction vehicles, relies on intermittent large bursts of power that can be detrimental for battery lifetime. Additionally, inherent electrical inefficiencies in battery cells lead to significant heat generation, and improper thermal management can reduce battery lifetime or cause premature failure via thermal runaway. Thus, in order to enable widespread adoption of electric vehicles across the transportation and mobility sector, significant technological improvements are necessary to increase power density across vehicle systems, and specifically power density of onboard energy storage.

1.2   Motivation

To address the need for power- and energy-dense electrical energy storage, hybrid energy storage systems have often been considered. These systems combine multiple, dissimilar storage elements in a single system, leveraging the respective strengths of the individual components for improved system performance [7]–[9]. Particularly, battery-ultracapacitor hybrid energy storage

2

systems (HESSs) are commonly considered for vehicle applications with exceptionally high ratios of peak to average power [10]–[12]. Combining power-dense ultracapacitor cells with energy-dense battery cells yields a hybrid system that is simultaneously energy- and power-dense, as demonstrated in Figure 1.2. However, these HESSs are subject to their own set of challenges. Battery-ultracapacitor HESSs necessitate control strategies which respect the operating requirements of the individual elements. Namely, batteries should be protected from excessively high discharge rates, and ultracapacitors, though subject to large voltage swings, must have their voltage remain within a certain range. Additionally, design of these systems is far from straightforward due to the inherent dissimilarities of the storage elements and the need for closed-loop control in vehicle platforms that are subject to highly variable conditions.
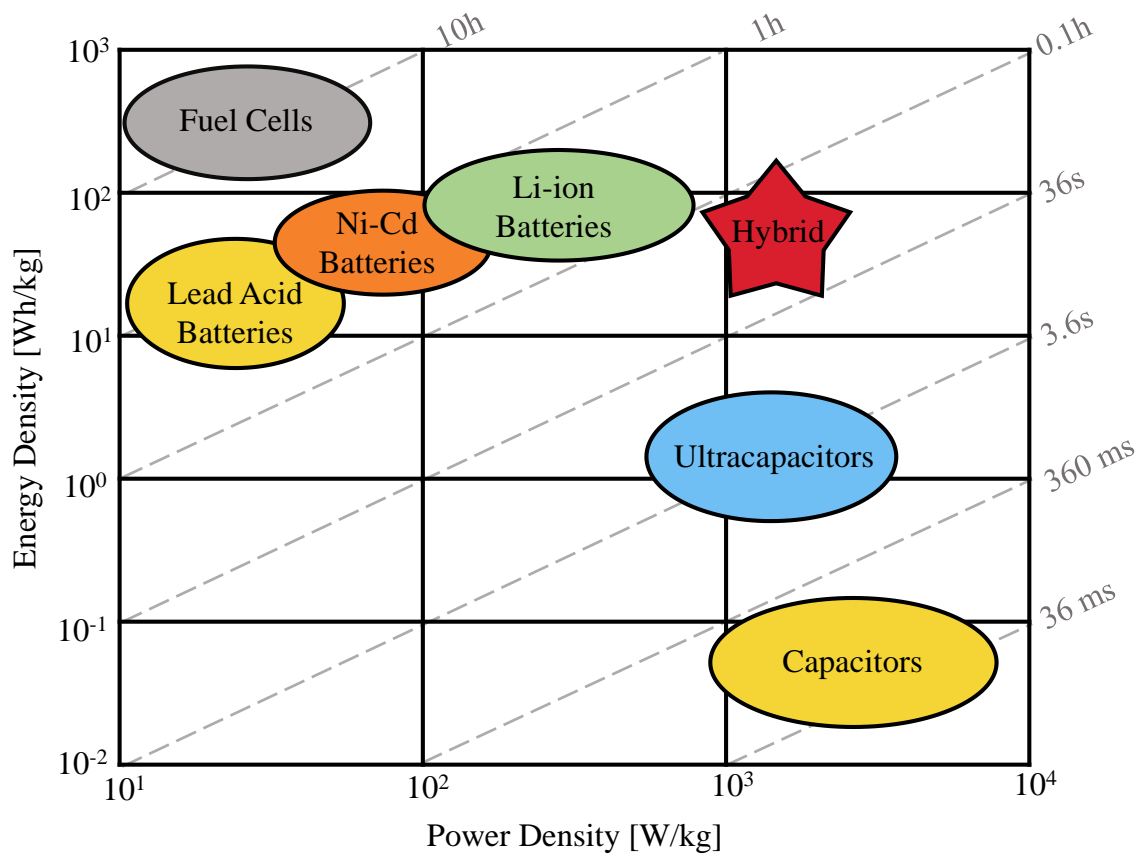
Figure 1.2: Ragone plot of various energy storage elements (adapted from [13]**).**

Regardless of the storage element, electronic components inevitably generate heat, and thermal requirements of the batteries, ultracapacitors, and included power electronics in an HESS may be vastly different, requiring special attention to be paid to the design of thermal management systems. In addition to the variation in thermal requirements between components, the variation in magnitude of thermal loads during a single drive cycle can be significant. In certain applications, such as city buses, heavy construction vehicles, and military vehicles, this variation can be even more extreme. Consider the example of load, haul, dump (LHD) loaders used in mining applications. These vehicles command a very high amount of power for brief periods while lifting and moving large payloads, as demonstrated below in Figure 1.3. These large power requirements, while present only during certain segments of the loading cycle, lead to large, intermittent thermal loads which can damage electronics and reduce operability of the vehicle platform.

	Loading Cycle Stages
1	Bucket filling
2	Leaving bank
3	Retardation
4	Reversing
5	Towards load receiver
6	Bucket emptying
7	Leaving load reciever
8	Retardation and reversing
9	Towards bank
10	Retardation at bank
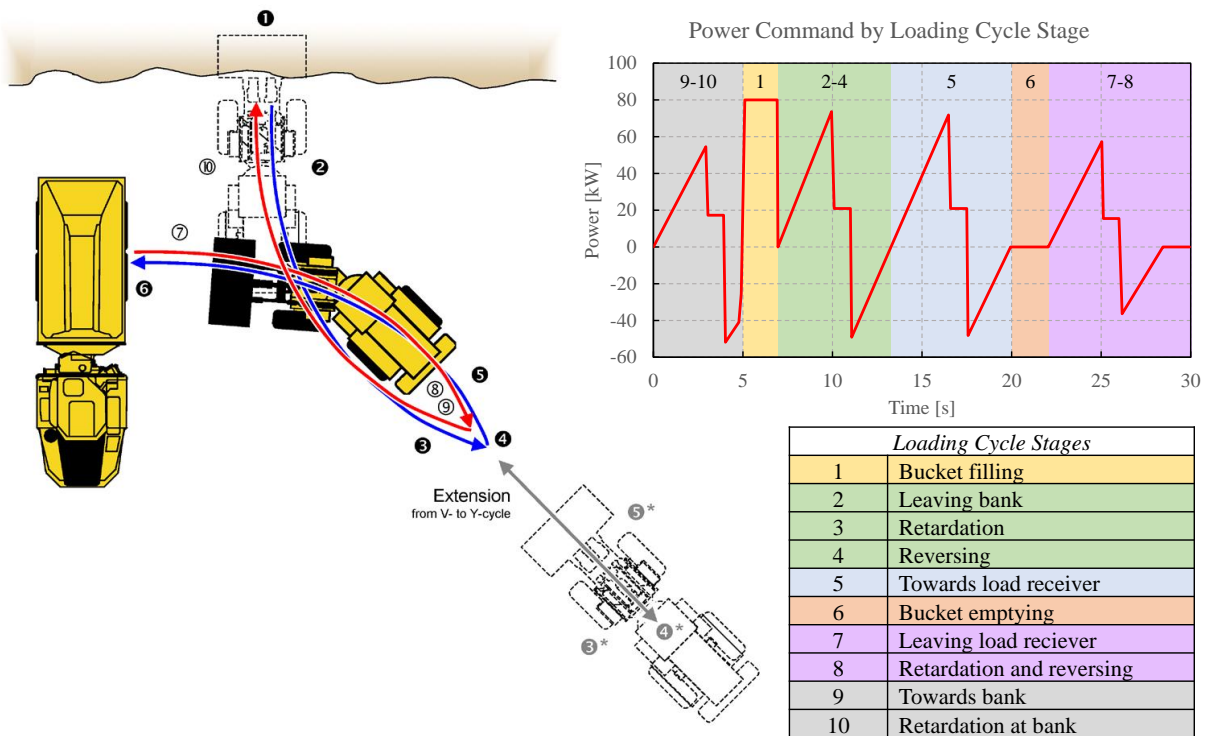
Figure 1.3: Loading cycle stages of wheel loader (illustration from [14]**, power command data from** [15]**).**

4

Thus thermal management systems are critical for these applications, and there are several routes to designing thermal management systems that address this issue of high peak thermal loads. One route could be to simply increase the size of the thermal management system so that it can handle the maximum thermal load expected for the given mission. However this method can lead to an unwieldy thermal management system, as the mass of thermal management components like pumps and heat exchangers can be substantial. Another alternative to address this is the incorporation of thermal energy storage within the thermal management system. Specifically, a phase change material (PCM) such as paraffin wax can be used to absorb thermal energy from electronics subsystems during mission segments with high thermal loads, then reject this stored energy to a thermal management system during dormant mission segments. Utilizing the solid-liquid phase transformation, these large bursts of thermal energy can be rapidly stored in the PCM with minimal temperature increase. Due to the low gravimetric density of PCMs such as paraffin wax compared to the materials used to make traditional thermal management components, thermal energy storage can provide a lightweight solution to account for peak thermal loads [16]. However, the ability of a solid-liquid PCM to rapidly store energy in latent form relies on the PCM remaining in a two-phase state; if the PCM fully melts, it will continue to store energy sensibly at a slower rate. After full melting, prolonged sensible heating will potentially lead to overheating of electronics and ensuing failures. Hence, when designing thermal management systems with PCM thermal energy storage, one must consider not only the differing thermal requirements of the various electronic components, but also the problem of actively regulating the amount of energy stored in the PCM using closed loop control.

The previous discussion of electrical and thermal energy storage systems highlights two specific options to increase power density of certain vehicle subsystems, but in order to achieve

an increase in power density by an order of magnitude, significant changes must be made to improve upon traditional methods for system-level vehicle design. These traditional design methods inhibit system-level power density improvement due to their sequential nature. For example, a novel aircraft design might sequentially progress from structural design to mechanical powertrain development to electronics equipment selection to thermal management design before finally ending up in the control design phase. Each of these design phases will be limited by the requirements and outcomes of the preceding step, so that the control designer is left with little wiggle room to improve and optimize power density-related metrics. Thus, multidisciplinary system-level design techniques offer the potential to significantly increase power density of next generation vehicles by considering all of these domains, and the controller, simultaneously [17].

However, multidisciplinary techniques incur several challenges that are avoided in traditional design methods. Multidisciplinary design techniques rely on system models that span multiple domains, such as mechanical, electrical, and thermal energy domains. Developing models that can accurately simulate system dynamics in multiple domains, which may have timescales that vary by orders of magnitude, is a daunting task. Additionally, in order to optimize designs over multiple domains, a method to systematically vary system parameters is needed, and this is far from straightforward for complex, multi-domain models. Furthermore, inclusion of closed-loop control in these systems is complicated by timescale separation and multi-domain coupling. As a result, when system parameters are varied to explore the design space, the performance of a controller may be detrimentally affected if this controller is designed for the nominal case.

1.3   Literature Review

There is a vast body of work in the area of multidisciplinary design optimization (MDO). Since originating in the field of structural optimization, MDO has expanded to find applications in

6

land, air, and sea vehicles, as well as stationary applications such as buildings and bridges [18]. While in some applications MDO approaches appropriately rely on static analyses to perform system-level optimization, many applications require careful treatment of the dynamic interactions within and between disciplines. If one wanted to optimize, or at the very least manipulate, these dynamic interactions in order to achieve improved system performance, a natural solution would be to incorporate a control strategy within the system as well as some method to manipulate the control strategy to optimize performance metrics. For this reason, control co-design has emerged in recent years as a subset of MDO in which combined optimization of the physical plant and controller is performed [19]. This optimization of the plant and controller can benefit system design on multiple fronts. For instance, in vehicle applications, plant design optimization can lead to improvements in size, weight, and cost, while controller design optimization can lead to improvements in reliability, performance, and efficiency. By combining these processes, control co-design optimization can provide simultaneous improvements in all of these fronts.

However, the process of setting up control co-design studies, especially studies spanning multiple domains, is not straightforward. Broadly speaking, a control co-design methodology consists of three general steps: modeling, controller development, and optimization. Selecting an appropriate modeling strategy is perhaps the most critical step because the subsequent phases of controller development and optimization depend heavily on model selection. An improper modeling strategy will incur challenges such as fidelity mismatch, neglect or improper treatment of relevant dynamics, communication difficulties between domains, and long computation times, which can make controller development and optimization infeasible due to overwhelming computational demands. An appropriate modeling strategy should be able to easily handle dynamics within each domain as well as cross-domain dynamics, should be reconfigurable and

readily modifiable to enable changing designs, and should be computationally efficient. Among the vast body of control co-design literature, graph-based modeling techniques address many of these needs while offering additional benefits for vehicle design optimization, such as modularity and scalability [20]–[23]. Additionally, these works demonstrate that graph-based methods are particularly well-suited for multi-domain controller development and design optimization for many of the same reasons.

The problem of control and design optimization of a hybrid electrical and thermal energy storage system as a case study for multi-domain control co-design is presented in this thesis. Several researchers have separately examined the optimization of similar electrical and thermal subsystems. There are several studies considering the optimal sizing of electrical energy storage elements within a hybrid electrical energy storage system [24]–[33], many of which also examine control optimization. On the other hand, there are some studies which consider design [34]–[38] and energy management optimization [39]–[42] for thermal energy storage. However, optimization of an integrated electro-thermal energy storage system has received little attention in the literature, especially in the context of vehicle energy storage. Some have considered the problem of electrical and thermal energy storage for building applications [43]–[45]. While several of these studies have considered design and control optimization, these studies consider the electro-thermal design optimization problem from a different perspective, neglecting the existence of electro-thermal coupling by treating the electrical and thermal storage as physically separate entities working together to lower electricity costs. Additionally, the methods presented within these studies consider much longer dynamic timescales on the order of several hours, rather than the seconds- or sub-seconds-long timescales on which vehicle dynamics evolve. Thus, a careful

treatment of the combined electrical and thermal performance of a hybrid electro-thermal energy storage system for electrified mobility through design and control optimization is missing.

1.4   Outline

This thesis seeks to address the problem of optimizing the sizing and control parameters of a hybrid electro-thermal energy storage system by incorporating and generalizing existing graph-based modeling, control, and design optimization techniques. To accomplish this multi-domain optimization, the electro-thermal system is first split into electrical and thermal subsystems, for which respective control and design optimization strategies are applied. Then, control and design optimization strategies for the full electro-thermal system are developed, which seek to improve power density of the storage system while maintaining system performance. The solutions of the system-level design and control optimization study are then compared to those resulting from the subsystem optimization routines. By applying and generalizing this graph-based framework to solve a multi-objective optimization problem, we aim to demonstrate the merits of the framework for multi-domain design and control optimization.

The outline of the thesis is as follows. Chapter 2 summarizes the graph-based modeling techniques used in this work, with special attention paid to the energy storage elements considered herein. Chapter 3 describes the control architectures of the electrical and thermal systems. Chapter 4 describes the optimization framework and its implementation for sizing and control parameter optimization of the electro-thermal energy storage system. Chapter 5 concludes the thesis and discusses directions for future work.

CHAPTER 2.   MODELING

2.1   Candidate System

The system under study in this work is a hybrid electro-thermal energy storage system. The particular architecture chosen for the electro-thermal system is well suited to meet the power and energy demands of vehicle systems with high ramp rate electrical and thermal loading, such as an electromagnetic aircraft launcher that might be found on a naval ship [46]. The load profile applied to the energy storage system in this work is representative of an electromagnetic UAV launcher, as an example of a high ramp rate system.

Before introducing the full electro-thermal system, the electrical and thermal subsystems will be described, starting with the electrical subsystem. The electrical subsystem, which will be referred to here as the hybrid energy storage system (HESS), is a battery-ultracapacitor hybrid energy storage system. Particularly, the HESS contains a battery pack, ultracapacitor pack, and two DC-DC power electronic converters, which interface with a shared voltage bus, as shown in Figure 2.1. This particular HESS configuration, known as the parallel active topology [47], allows independent control of the two storage elements. It allows the HESS to leverage the power dense ultracapacitor to supply transient high ramp rate power demands and the energy dense battery to supply the average power demands of the load. In addition to the high ramp rate load representing a UAV launcher, the hybrid energy storage system is assumed to be used to power other electronic systems with significantly slower ramp rates. With the emphasis of the work herein restricted to the energy storage system, the high ramp rate UAV launch load profile and other load profiles are aggregated into a single current load acting at the voltage bus.
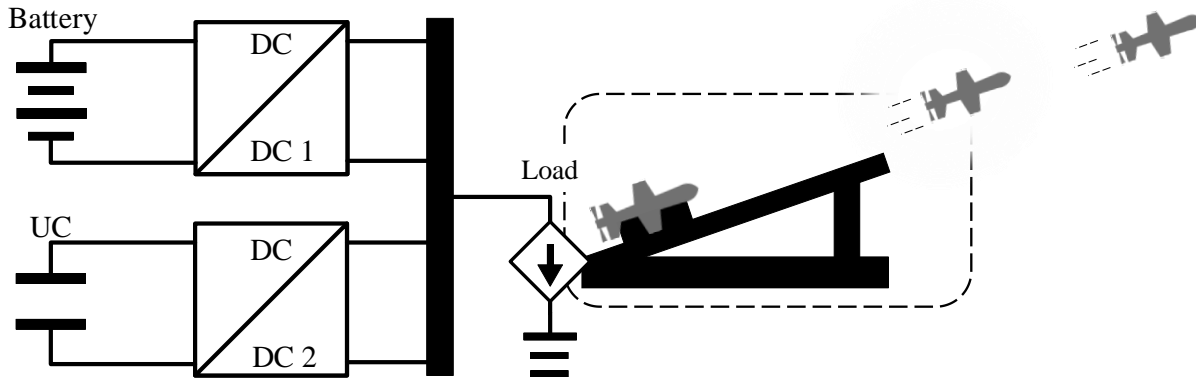
Figure 2.1: HESS schematic.

The thermal subsystem, referred to hereafter as the thermal energy storage system (TESS), is a single-phase liquid coolant thermal management system with phase change material thermal energy storage (TES) modules. We note that, like the HESS, the TESS is also hybridized, in the sense that it consists of two different thermal energy storage mechanisms, one which stores thermal energy through a change of phase and the other which stores energy through sensible heating of coolant. Hybridizing the thermal management in this way parallels the hybridization of the HESS; the TES module is able to quickly store thermal energy from high ramp rate thermal loads, while the heat exchanger is able to reject thermal energy at a limited rate which is appropriate for the average thermal loads without high ramp rate variations. The coolant loop contains a liquid-liquid heat exchanger, fluid reservoir, pump, continuously variable valve, and two cold plate heat exchangers. Thermal loads generated by components of the HESS are applied directly to TES modules, one of which is attached to each cold plate heat exchanger. When considering the TESS on its own, the loads applied to the TES modules are defined to act as surrogates for the thermal loads generated by the HESS under standard operation. In this case, the load applied to TES1 is a surrogate for heat generated by the battery, ultracapacitor, and converters, and the load applied to TES2 is a surrogate for heat generated by the electrical load shown in Figure 2.1. With the selected

architecture shown in Figure 2.2, coolant flow in the thermal management system is split between two sections corresponding to the two TES modules. This allows independent control of coolant flow rate though each cold plate, and hence allows control of the heat transfer rate from the cold plates. Because of their direct influence on temperature dynamics, which will be shown in the latter half of Section 2.3, the mass flow rates in the TESS are treated as controllable inputs.
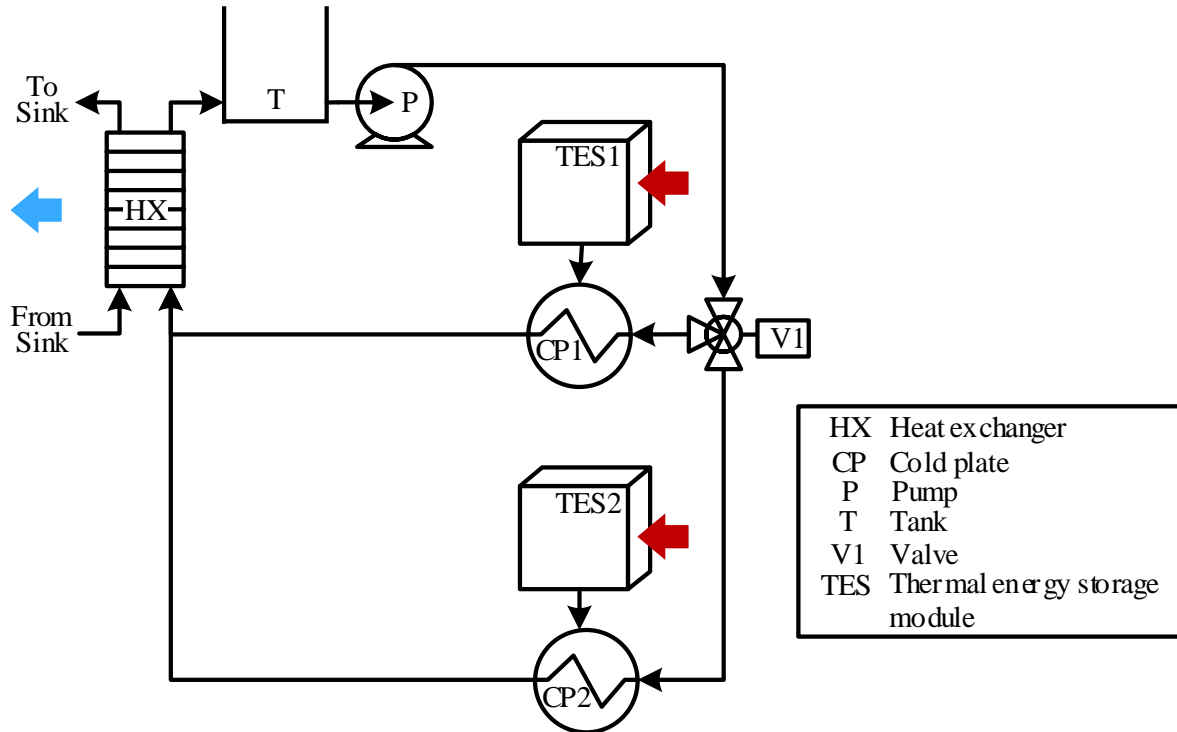
Figure 2.2: TESS schematic.

The hybrid electro-thermal energy storage system (HETESS) combines the HESS and TESS resulting in the architecture shown in Figure 2.3. The HESS configuration is unchanged from the above description. The TESS configuration is slightly modified to introduce a third cold plate and TES module in one of the flow sections. Then, thermal loads generated by the HESS are split between the three TES modules such that the heat generated by the energy storage elements is applied to TES1, the heat generated by the electrical load is applied to TES2, and the heat generated by the converters is applied to TES3. This configuration allows the energy storage

components, which are generally more sensitive to temperature fluctuations, to be separated

thermally from the power converters, which are expected to undergo more significant temperature

fluctuations. These electro-thermal couplings are illustrated by the shaded red regions and arrows

in Figure 2.3.
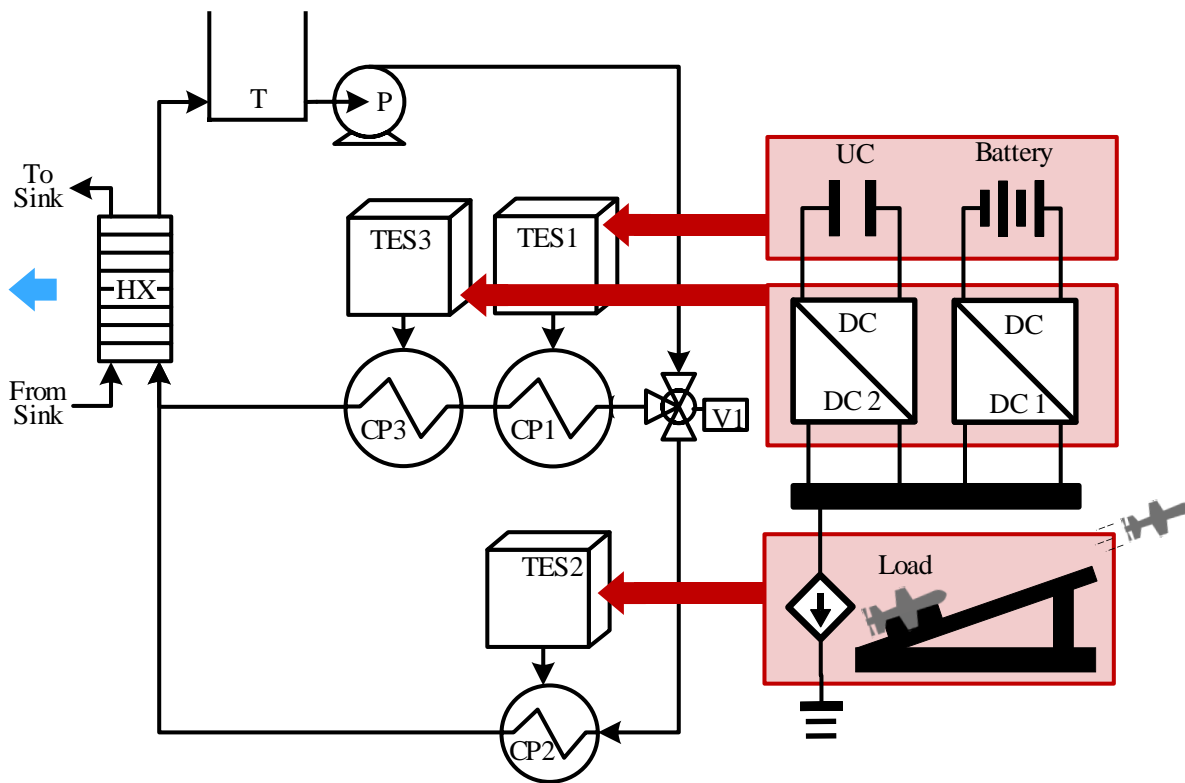
Figure 2.3: HETESS schematic.

2.2   Graph-Based Modeling Basics

The modeling strategy used in this thesis employs graph theoretic techniques to visualize

and mathematically represent energy transfer within a power system. There are many advantages

of using graph-based techniques to represent the dynamics of power systems. To start, graph-based

models allow for the development of modular component models, which can be readily inserted

into and removed from a larger graph. Modular component models are also self-contained in the

sense that component models can be tested individually under known environmental conditions to

verify that the model behavior is true to the physical component behavior. Additionally, graph-based models can have varying levels of fidelity, since any vertex in an energy-based graph model can be refined by dividing the vertex into a cluster of connected vertices to obtain higher resolution in the relevant quantities. At the same time, by clustering vertices, graph models can readily be reduced to only the most relevant physical quantities in order to maximize computational efficiency. The graph models used in this work are also inherently domain agnostic due to their basis in conservation of energy, which is invariant across different domains, such as electrical, thermal, mechanical, and hydraulic energy domains. Finally, a key feature of graph-based modeling upon which this work relies is its scalability. The particular graph-based modeling framework used herein allows for representation of components with varying scales, which enables studies on optimal sizing of components. Previous work has shown the strengths of this modeling scheme for thermal, hydraulic, electrical, and mechanical systems [48]–[53]. A brief introduction to the graph-based modeling strategy is given here, in the context of power systems, and the interested reader is referred to [48], [51], [54] for more details.

This modeling framework captures power interactions and interconnections as a directed graph $\mathcal{G}$ of order N_v and size N_e (i.e., having N_v vertices and N_e edges), such as the notional graph shown in Figure 2.4. Denoting by $\mathcal{V}$ the set of vertices and by $\mathcal{E}$ the set of edges, such a graph is denoted $\mathcal{G} = (\mathcal{V}, \mathcal{E})$. Each vertex $v_i \in \mathcal{V}$ represents an energy storage element with an associated state x_i, while each edge $e_j \in \mathcal{E}$ represents an associated transfer of power P_j, hereafter referred to as a "power flow", between two vertices. The orientation of edge e_j indicates the assumed direction of positive power flow from the "tail" vertex v_j^{tail} to the "head" vertex v_J^{head}. Note that power flows can travel bidirectionally, and this assumption of positive power flow is

14

merely a convention. Applying conservation of energy to the state x_i associated with vertex v_i yields the following equation

$$C_i \dot{x}_i = \sum_{\{j:e_j \in \mathcal{E}_i^{head}\}} P_j - \sum_{\{j:e_j \in \mathcal{E}_i^{tail}\}} P_j , \tag{2.1}$$

where $C_i \geq 0$ is the energy storage capacitance of the state, $\mathcal{E}_i^{head}$ is the set of edges for which v_i is the head vertex (i.e., edges oriented into v_i), and $\mathcal{E}_i^{tail}$ is the set of edges for which v_i is the tail vertex (i.e., edges oriented out of v_i). In the special case for which $C_i = 0$, the associated state x_i cannot be defined by a dynamic relationship, but rather an algebraic relationship between the incident power flows. A state having this property is referred to as an algebraic state.
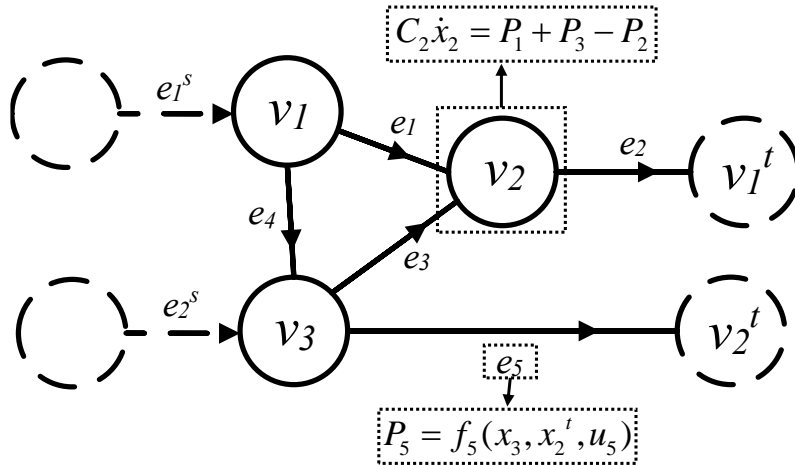
Figure 2.4: Notional graph-based model (modified from [48], [51], [54]**).**

The associated power flow P_j for edge e_j is defined as a function of the head and tail vertices as well as an input signal u_j associated with that edge.

$$P_j = f_j(x_j^{tail}, x_j^{head}, u_j) \tag{2.2}$$

These functions can be linear or nonlinear, depending on the linearity of the underlying physical mechanisms. Due to the nature of the electro-thermal systems under study, these functions often

consist of similar terms. Collecting all the common terms that arise within these systems, the following generic formulation can be introduced for the general form of the power flows

$$P_j = g_j(x_t, x_h, u_j) \ (c_1 x_t \quad +c_2 x_h \quad +c_3 x_h x_t \quad +c_4 x_t^2 \quad +c_5 x_h x_t^2$$
$$+c_6 x_t u_j \ +c_7 x_h u_j \ +c_8 x_h x_t u_j \ +c_9 x_t^2 u_j \ +c_{10} x_h x_t^2 u_j \qquad (2.3)$$
$$+c_{11}),$$

where x_t, x_h, and u_j are a shorthand notation for the tail state, head state, and input acting on

edge j respectively, g_j is a nonlinear function of x_t, x_h, and u_j, and c_i, $i = 1, \ldots, 11$, denote

constant coefficients for each of the 11 terms.

Disturbances to the system, or interactions with its environment, are included in the

framework as "sink" vertices or "source" edges. A given graph has N_t sink vertices, shown as

vertices with dashed edges in Figure 2.4, representing external states x^t that correspond to states

of neighboring components. Depending on the values of the states corresponding to a sink vertex

and its neighboring vertex, a sink vertex can either supply power to the system (e.g., an electrical

current source) or draw power from the system (e.g., a sink fluid which absorbs excess heat from

the system). As external signals, the dynamics of the sink states corresponding to sink vertices are

excluded from the system analysis, and so these states are not included in the state vector

$x = [x_1, \ldots, x_{N_v}]^T$ defined by (2.1).

Source edges, shown in Figure 2.4 as dashed edges whose tail vertices have dashed

outlines, represent power flows that are directly drawn from or injected into the system (e.g., a

heat load applied to a thermal component). Each of the N_s source edges has a corresponding

power flow P_j^s representing a power interaction between the system and its environment.

With states, power flows, sink states, and source power flows defined in this manner, the

system dynamics can be represented in a compact matrix form. In order to do so, the structure of

the graph must be formulated mathematically. This is accomplished using matrices M and D which define the graph structure in terms of connections between vertices and edges. The incidence matrix $M = [m_{ij}] \in \mathbb{R}^{N_v \times N_e}$ defines vertex and edge interconnections according to the following convention

$$m_{ij} = \begin{cases} 1 & \text{if } v_i \text{ is the tail of } e_j, \\ -1 & \text{if } v_i \text{ is the head of } e_j, \\ 0 & \text{else.} \end{cases} \tag{2.4}$$

As mentioned previously, external state dynamics are not excluded in the system analysis, so the incidence matrix can be partitioned as

$$M = \begin{bmatrix} \bar{M} \\ \underline{M} \end{bmatrix}, \tag{2.5}$$

with $\bar{M} \in \mathbb{R}^{(N_v - N_t) \times N_e}$, such that $\bar{M}$ gives the mapping of power flows to system states x and $\underline{M}$ gives the mapping of power flows to sink states x^t.

Analogously, the matrix $D = [d_{ij}] \in \mathbb{R}^{(N_v - N_t) \times N_s}$ defines mappings between vertices and source edges. Elements of the matrix D are given by the following relation

$$d_{ij} = \begin{cases} 1 & \text{if } v_i \text{ is the head of } e_j^s, \\ 0 & \text{else.} \end{cases} \tag{2.6}$$

Finally, defining the matrix C to be a diagonal matrix containing the capacitances of the system states x, the system dynamics of a generic graph-based model can be represented in the following form

$$C\dot{x} = -\bar{M}P + DP^s. \tag{2.7}$$

As a result of the domain-agnostic nature of this formulation, this framework has proven well-suited to capture various multi-domain dynamics, including electrical, thermal, mechanical,

and hydraulic dynamics. A detailed discussion of the treatment of multi-domain models is given in [48]. A brief discussion of multi-domain models, specifically pertaining to the electrical and thermal domains considered herein, is provided here, and the interested reader is referred to [48] for a more thorough discussion.

In a given energy domain, it is instructive to quantify energy storage elements (states x of the system) in terms of physically relevant quantities. For instance, electrical energy can be stored in the form of a capacitor voltage or an inductor current, so electrical graph models often consist of voltage and current states which quantify energy stored in capacitors and inductors. In the thermal domain, energy can be stored sensibly in the form of an increase in temperature of a thermal mass, so a thermal graph model might consist of temperature states representing temperatures of various thermal masses. Because energy states may represent vastly different physical quantities, vertices are classified by their type to distinguish the various types of energy storage occurring within a system. In subsequent schematics, vertex color will be used to distinguish the vertices by their type according to the following general scheme: voltage states are shaded in green, current states in yellow, and temperature states in pink.

The formulation for the capacitance of a given state will depend on the type of its corresponding vertex, and for some vertex types considered in this thesis the capacitance may be a function of the state. Considering the capacitor example, the energy storage dynamic is given by $CV\dot{V} = P_{in} - P_{out}$, in terms of the capacitance C, voltage V, and electrical power P entering and leaving the capacitive element. In the graph-based framework, this is represented by a voltage-type vertex with corresponding state variable $x_i = V$ and state-dependent capacitance $C_i = CV$. Similarly, an inductor is represented as a current-type vertex with state variable $x_i = I$ quantifying the current and state-dependent capacitance $C_i = LI$, where L is the inductance. On the other hand,

considering the example of a thermal mass, the energy storage dynamic is given by $C_T \dot{T} = \dot{Q}_{in} - \dot{Q}_{out}$, in terms of the sensible heat capacity C_T of the thermal mass and the heat $\dot{Q}$ transferred into/out of the thermal mass. This is represented in the graph-based framework as a single vertex with state $x_i = T$ and state-independent capacitance C_T. State-dependent capacitances, such as the capacitances for voltage and current states discussed above, can complicate the tasks of simulation and analysis. However, it is often the case that the capacitances and dynamics of these states can be represented in a simplified manner by eliminating the state dependence. One method of eliminating these state dependencies, referred to as a modified graph formulation, is discussed at length in [48]. The modified graph formulation is used to eliminate state-dependent vertex capacitances in this thesis.

2.3   Graph-based Component Models

In order to develop the full graph-based model of the hybrid electro-thermal energy storage system, graph-based models are developed for each of the component models. The component models used in the candidate system are presented in this section, starting with the electrical components. For the HESS, graph-based models are presented for the battery pack, ultracapacitor pack, power electronics, and electrical bus. A more thorough discussion is provided for the battery and ultracapacitor pack to emphasize the impacts of the sizing variables on these component models, which will be relevant in subsequent chapters of this thesis.

The component models for the electrical subsystem are followed by those for the TESS. Within this subsystem, thermal models are considered only for those components with significant temperature effects: TES modules, cold plates, heat exchanger, and tank. The remaining components – pump, valves, and pipes – are assumed to have negligible effects on the thermal dynamics. However, we note that modeling of the hydraulic dynamics introduced by some of these

components (most significantly, the pump) is crucial to ensuring that the thermal system is actuated with admissible flow rates. With hydraulic dynamics falling outside the scope of this thesis, we use the hydraulic dynamic equations as described in [53] while omitting the discussion of these hydraulic dynamics. Of the thermal components discussed in this section, emphasis is placed on the TES module model, as this model is a contribution of this thesis and the model's incorporation of sizing variables will be relevant in subsequent chapters.

2.3.1 Battery Model

The battery in this system acts as the main power source, providing the average or filtered load demands. The graph-based model of the battery pack is derived from an equivalent circuit model, as is typical for control-oriented battery models [55]. The particular circuit chosen to model the dynamics of the battery pack, shown in Figure 2.5 a), offers sufficient levels of fidelity and computational simplicity for the control and design optimization purposes considered herein. The graph model associated with this circuit is introduced in [48], and is reproduced here for completeness. Consisting of two RC pairs, this model captures both fast and slow electrical dynamics. Additionally, the thermal dynamics of the battery are modeled using the thermal circuit shown in Figure 2.5 b.), which gives the surface and core temperatures of the battery. These circuit models capture electro-thermal coupling within the battery. Thermal dynamics affect the electrical circuit through electrical parameters such as resistance and capacitance values which are determined as temperature-dependent maps, while electrical losses are input to the thermal circuit as heat generation.
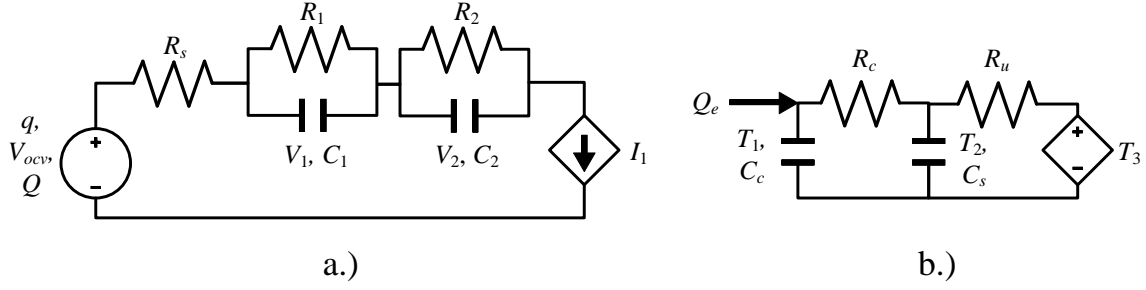
Figure 2.5: a.) Battery electrical circuit and b.) thermal circuit models.

The graph model of the electrical circuit in Figure 2.5 a.) is derived by analyzing the electrical dynamics in the circuit. The voltage dynamics are given by the following.

$$C_1 V_1 \dot{V}_1 = -\frac{V_1^2}{R_1} + V_1 I_1 \tag{2.8}$$

$$C_2 V_2 \dot{V}_2 = -\frac{V_2^2}{R_2} + V_2 I_2 \tag{2.9}$$

$$Q V_{ocv} \dot{q} = -V_{ocv} I_1 \tag{2.10}$$

In these equations, C_1, C_2 are the capacitances of the respective capacitors, V_1, V_2 are their respective voltages, R_1, R_2 are the respective resistances of the RC pairs, q is the state-of-charge (SOC) of the battery, Q is the capacity of the battery, I_1 is the battery current, and $V_{ocv} = V_{ocv}(q)$ is the open circuit voltage of the battery pack, dependent on its SOC. The terminal voltage of the pack is then given by

$$V_T = V_{ocv} - V_1 - V_2 - I_1 R_s. \tag{2.11}$$

The heat generated by the battery due to resistor losses is given by $Q_e = R_s I_1^2 + V_1^2 / R_1 + V_2^2 / R_2$. In response to this heat generation, the thermal dynamics of the battery cell are determined using the following

$$C_c \dot{T}_1 = Q_e - \frac{1}{R_c}(T_1 - T_2), \tag{2.12}$$

$$C_s \dot{T}_2 = \frac{1}{R_c}(T_1 - T_2) - \frac{1}{R_u}(T_1 - T_3), \tag{2.13}$$

where C_c, C_s are the thermal capacitances of the battery core and shell respectively, T_1, T_2 are the temperatures of the core and shell respectively, T_3 is the temperature of a thermal sink to which the battery rejects heat, R_c is the battery's internal conduction resistance, and R_u is the thermal resistance between the battery and its thermal sink.

These dynamic equations are translated into the graph-based modeling framework, resulting in the graph-based battery model shown in Figure 2.6. Additionally, the state vector and capacitance vector are given below.

$$x = [q \ V_1 \ V_2 \ T_1 \ T_2]^T \tag{2.14}$$

$$C = [QV_{ocv} \ C_1 V_1 \ C_2 V_2 \ C_c \ C_s]^T \tag{2.15}$$
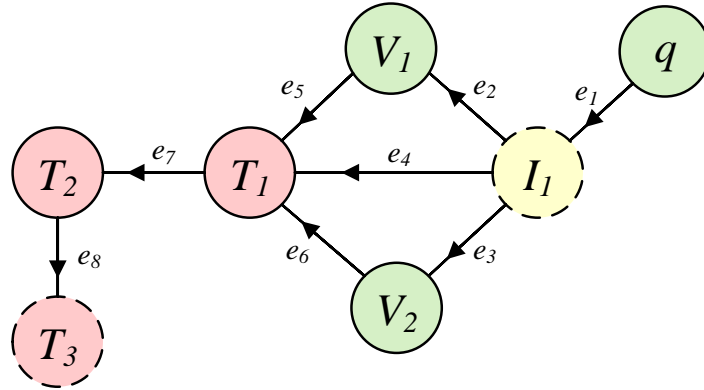
Figure 2.6: Battery graph model.

The preceding equations give the dynamics of a battery cell and, under certain assumptions, are readily adapted to model a battery pack consisting of multiple cells in series and parallel. Assuming that the pack is balanced and that the current in each cell is equal, the voltage dynamics

22

of each battery cell will be given by (2.8)-(2.9), with the respective resistance and capacitance parameters now given by $R'_{1,2} = R_{1,2}/N_p$ and $C'_{1,2} = N_pC_{1,2}$, where N_p is the number of cells in parallel. The SOC of the pack is given by (2.10), where the pack capacity is $Q' = N_pQ$ and the open circuit voltage is $V'_{ocv} = N_sV_{ocv}$, where N_s is the number of cells in series. Defining $R'_s = N_sR_s/N_p$, the terminal voltage of the pack is then given by $V'_T = N_sV_T$. The heat generated by the battery pack is then $Q'_e = N_sQ_e$. The thermal dynamics are again given by (2.12)-(2.13), with the internal resistance and capacitance parameters modified as $R'_c = R_c/(N_sN_p)$ and $C'_{c,s} = N_sN_pC_{c,s}$.

2.3.2 Ultracapacitor Model

The ultracapacitor in this study acts as a supplementary power source to the battery, supplying power at high magnitudes in order to protect the battery from damagingly high discharge rates. Ultracapacitors are similar to capacitors in many regards, but one aspect that differentiates them from standard linear capacitors is their nonlinear voltage dynamics. At low currents, the effects of these nonlinearities may be negligible, but as current levels increase, their impact becomes more significant. In this work, two different models are considered for the electrical dynamics of the ultracapacitor. The first of these models neglects the inherent nonlinearities by treating the ultracapacitor as an ideal linear capacitor. In this case the graph-based model of the ultracapacitor reduces trivially to a single voltage state with capacitance CV, where C is the ultracapacitor cell's capacitance in Farads (assumed constant) and V is the instantaneous voltage across the cell. The second model captures the nonlinearities in the ultracapacitor voltage response using the equivalent circuit model developed and validated experimentally in [56]. The electrical dynamics of each ultracapacitor cell are modeled by an electrical circuit consisting of three RC

23

branches and a parallel leakage resistance, as shown in Figure 2.7 a.). The thermal dynamics of the ultracapacitor are captured by the lumped first-order thermal circuit shown in Figure 2.7 b.).
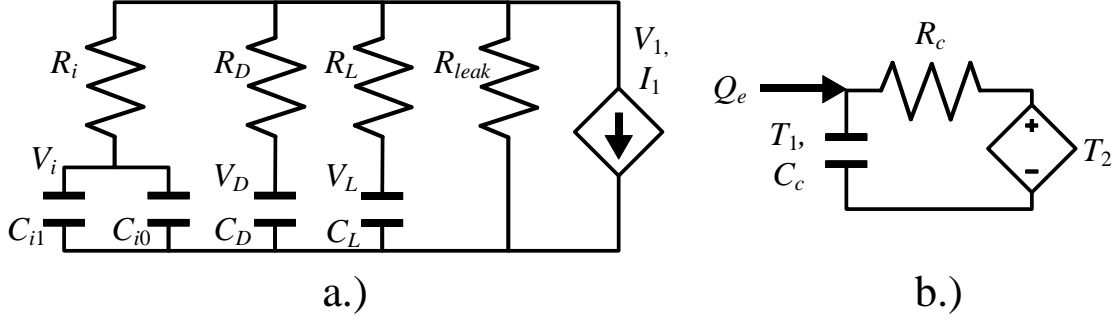
Figure 2.7: a.) Ultracapacitor electrical circuit and b.) thermal circuit models.

The RC branches of the electrical circuit represent immediate, delayed, and long-term time scales, with time constants on the order of a few seconds, a few minutes, and 10 minutes respectively. The time constants of these branches are chosen such that the equivalent circuit model accurately captures the behavior of the ultracapacitor over a 30-minute time range [56]. The immediate branch contains a nonlinear capacitor whose capacitance is given by

$$C_{i1} = KV_i \qquad (2.16)$$

where K is an experimentally determined constant and V_i is the voltage across the capacitor in the immediate branch. All other capacitors in this equivalent circuit model are considered to be ideal capacitors. The dynamics of the voltages across these capacitors are given by

$$C_i V_i \dot{V}_i = -V_i I_i, \qquad (2.17)$$

$$C_D V_D \dot{V}_D = -V_D I_D, \qquad (2.18)$$

$$C_L V_L \dot{V}_L = -V_L I_L, \qquad (2.19)$$

where $C_i = C_{i0} + C_{i1}$, C_D, and C_L are the capacitances of the immediate, delayed, and long-term branches respectively, V_D and V_L are the voltages across the capacitors in the delayed and long-

term branches respectively, and I_i, I_D, and I_L are the currents the respective branches. These currents are determined by the following algebraic functions of the capacitor voltages in each branch

$$I_i = \frac{V_i - V_1}{R_i}, \tag{2.20}$$

$$I_D = \frac{V_D - V_1}{R_D}, \tag{2.21}$$

$$I_L = \frac{V_L - V_1}{R_L}, \tag{2.22}$$

where R_i, R_D, and R_L are the resistances in the respective branches and V_1 is the terminal voltage of the cell. The terminal voltage is given by

$$V_1 = \frac{R_{leak}(V_i/R_i + V_D/R_D + V_L/R_L - I_1)}{1 + R_{leak}(1/R_i + 1/R_D + 1/R_L)}, \tag{2.23}$$

where R_{leak} is the leak resistance and I_1 is the current demand of the ultracapacitor cell.

The particular ultracapacitor cell considered in this study was a 100F, 2.7V Nesscap cell, the electrical parameters of which were parameterized by performing a constant current charging test [12]. These parameters are given in Table 2.1. The time constants of each branch in this parameterized model, calculated as $\tau = RC$, are in agreement with the desired orders specified previously for each branch. Note that, since the capacitance of the immediate branch varies with voltage V_i as defined in (2.16), the time constant in the immediate branch is variable, but remains considerably smaller than the time constants of the other branches. Because of this, the current in the immediate branch provides a significantly larger portion of the total current demand than current in the other branches. In Table 2.1, the time constant of this branch is approximated by evaluating its value at $V_i = 1.35V$, which is half of the maximum value of the cell terminal voltage.

25

Table 2.1: Ultracapacitor circuit parameters.

Parameter	Value	Associated Time Constant
R_i	22.1mΩ	
C_{i0}	74.6F	$\tau_i \approx 1.76s$
C_{i1}	3.81F/V	
R_D	49Ω	
C_D	8.14F	$\tau_D = 6.65\,\text{min}$
R_L	258Ω	
C_L	6.60F	$\tau_L = 28.3\,\text{min}$
R_{leak}	1.59kΩ	

The heat generated by the ultracapacitor is then determined by the following

$$Q_e = I_i^2 R_i + I_D^2 R_D + I_L^2 R_L + I_{leak}^2 R_{leak} \tag{2.24}$$

where I_{leak} is the leakage current, determined by $I_{leak} = V_1 / R_{leak}$. With this, the temperature dynamics of the ultracapacitor are given by

$$C_c \dot{T}_1 = Q_e - \frac{T_1 - T_2}{R_c}, \tag{2.25}$$

where C_c is the thermal capacitance of the cell, T_1 is the temperature of the cell, T_2 is the temperature of the thermal sink for the ultracapacitor, and R_c is the thermal resistance between the cell and thermal sink.

These dynamic equations are readily translated into the graph-based modeling framework, resulting in the graph-based ultracapacitor model shown in Figure 2.8. Additionally, the state vector and capacitance vector are given below

$$x = [V_i \ V_D \ V_L \ T_1 \ I_i \ I_D \ I_L \ I_{leak} \ V_1]^T \tag{2.26}$$

$$C = [C_i V_i \ C_D V_D \ C_L V_L \ C_c T_1 \ L_i I_i \ L_D I_D \ L_L I_L \ L_{leak} I_{leak} \ C_1 V_1]^T \tag{2.27}$$

where we note that the states I_i, I_D, I_L, I_{leak}, and V_1 are given by algebraic relationships of the other states, and hence their associated capacitances and inductances are zero $(L_i = L_D = L_L = L_{leak} = C_1 = 0)$.
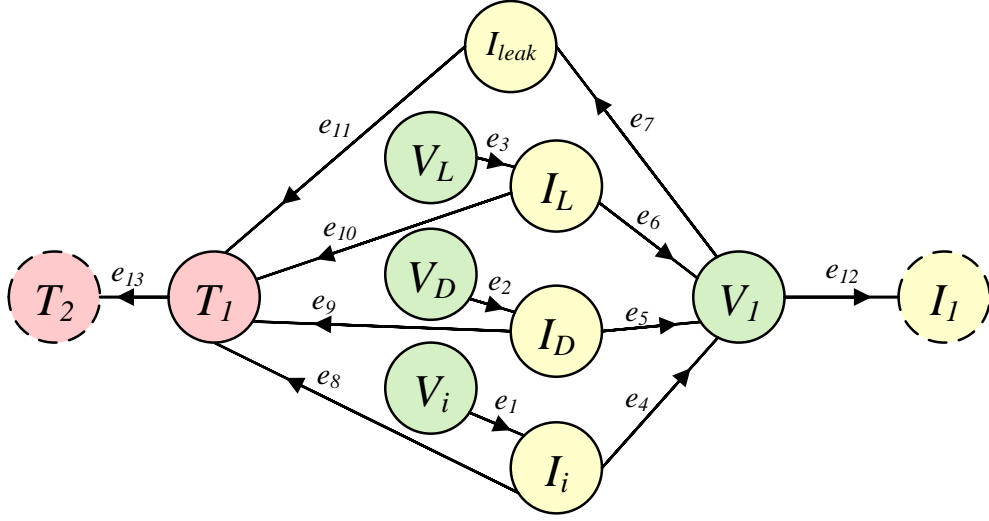
Figure 2.8: Ultracapacitor graph model.

For the ultracapacitor packs considered in this work, the parameters mentioned above are adjusted to reflect the number of cells combined in series/parallel following the same conventions as the battery. Assuming once more that the pack is balanced and the current in each cell is equal, the voltage dynamics of each cell are given by (2.17)-(2.19) with adjusted parameters $R'_{i,D,L,leak} = R_{i,D,L,leak} / N_p$ and $C'_{i,D,L} = N_p C_{i,D,L}$, where N_p is the number of parallel ultracapacitor cells. The cell currents are given by (2.20)-(2.22), with the cell terminal voltage given by (2.23), and the terminal voltage of the pack is then given by $V_T = N_s V_1$ where N_s is the number of series ultracapacitor cells. The thermal parameters are adjusted similarly to those of the battery pack, with $R'_c = R_c / (N_s N_p)$ and $C'_c = N_s N_p C_c$.

27

2.3.3 DC-DC Power Converter Model

The DC-DC power converters allow the electrical storage elements to interface with the shared voltage bus while providing the mechanisms to actuate the electrical system. The model used to represent the behavior of these converters is a time-averaged graph-based model from [48], which is reproduced here for completeness. The electrical circuit schematic for this component is shown in Figure 2.9 a.). In this work, the power converters are operated strictly in buck mode, with the time-averaged response given by

$$L_1 I_1 \dot{I}_1 = 0 = u V_2 I_1 - u R_s I_1^2 - R_L I_1^2 - (1-u) V_3 I_1 - (1-D) R_D I_1^2 - V_1 I_1 \tag{2.28}$$

where V_1, V_2, and V_3 are the output, input, and diode voltages respectively, I_1 and I_2 are the inductor current and output current respectively, R_s, R_D, and R_L are the resistances of the switch, diode, and inductor respectively, L_1 is the inductance, and u is the duty cycle of the converter. This duty cycle is the mechanism for actuation of the converter and allows control of the electrical system.

The thermal circuit of the converter takes the same form as the circuit model shown in Figure 2.7 b.) for the ultracapacitor. With converter heat generation given by

$$Q_e = R_L I_1^2 + u R_s I_1^2 + (1-u) R_D I_1^2, \tag{2.29}$$

the temperature dynamics of the converter are as follows

$$C_c \dot{T}_1 = Q_e - \frac{1}{R_u}(T_1 - T_2), \tag{2.30}$$

where C_c is the heat capacity of the converter, T_1 is the lumped temperature of the converter, T_2 is the temperature of the converter's thermal sink, and R_u is the thermal resistance between the converter and its thermal sink.

The graph-based model of the DC-DC converter is shown in Figure 2.9 b.). The state and capacitance vector for the converter is provided below

$$x = [I_1 \ V_1 \ T_1]^T \tag{2.31}$$

$$C = [L_1 I_1 \ C_1 V_1 \ C_c]^T \tag{2.32}$$

where $C_1 = L_1 = 0$ for the time-averaged case considered herein. Hence I_1 and V_1 are treated as algebraic states in this work.
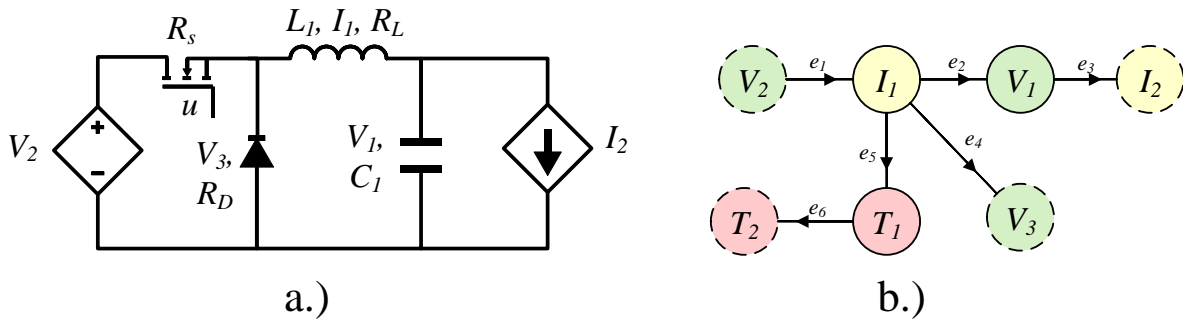
Figure 2.9: a.) DC-DC converter circuit and b.) graph model.

2.3.4 Voltage Bus Model

The last of the electrical components is a voltage bus which supplies power from the storage elements to the load as shown in Figure 2.1. The model used here for the voltage bus derives from the generic electrical bus model introduced in [48]. In this section, the HESS-specific version of this generic electrical bus model is presented. The circuit diagram of this version is shown in Figure 2.10 a.). The electrical dynamics for this component are given by

$$L_1 I_1 \dot{I}_1 = V_2 I_1 - R I_1^2 - V_1 I_1 \tag{2.33}$$

$$L_2 I_2 \dot{I}_2 = V_3 I_2 - R I_2^2 - V_1 I_2 \tag{2.34}$$

$$C_1 V_1 \dot{V}_1 = V_1 I_1 + V_1 I_2 - V_1 I_3 \tag{2.35}$$

29

where L_1 and L_2 are the inductances of electrical inputs 1 and 2 respectively, I_1 and I_2 are the currents of electrical inputs 1 and 2 respectively, V_2 and V_3 are the voltages of these electrical inputs, R is the bleed resistance for these electrical inputs, C_1 is the capacitance of the bus, V_1 is the bus voltage, and I_3 is the load current. Depending on the desired level of fidelity, the dynamics introduced by the capacitances and inductances in this circuit can be neglected by setting the inductance and capacitance parameters to zero and thereby treating the bus voltage and input currents as algebraic states. In this work, we will consider a case in which these states are treated as algebraic and another case in which these states are dynamic.

The graph-based model of this voltage bus is shown in Figure 2.10 b.). Temperature dynamics of the bus are neglected by assuming the bleed resistance is small. The state vector and capacitance matrix are given below.

$$x = [V_1 \ I_1 \ I_2]^T \tag{2.36}$$

$$C = [C_1 V_1 \ L_1 I_1 \ L_2 I_2]^T \tag{2.37}$$

<center>a.)   b.)</center>
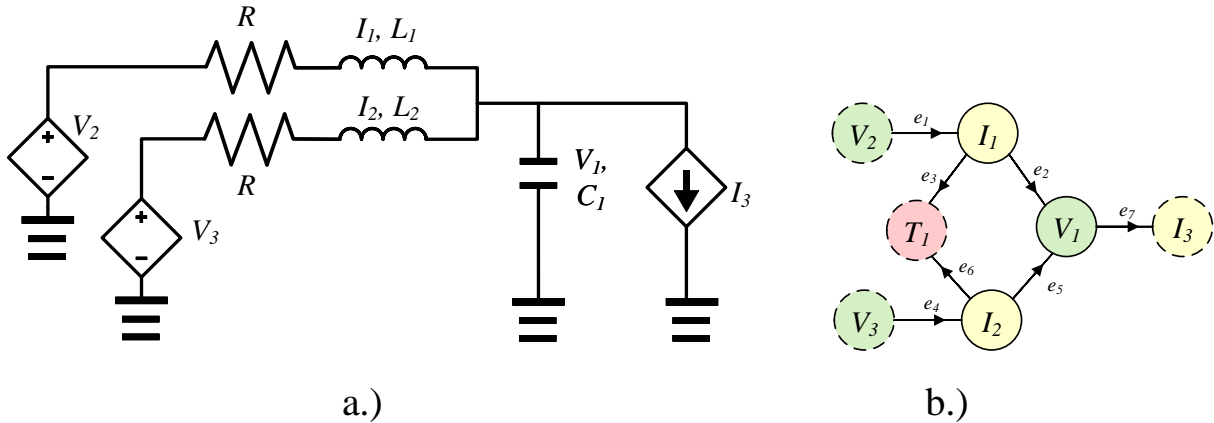
Figure 2.10: a.) Bus circuit and b.) graph model.

<u>2.3.5 Thermal Energy Storage Module Model</u>

The electrical storage components and power converters generate a significant amount of heat at high ramp rates. It is further assumed that the electrical load to which the HESS supplies power has inherent losses which will contribute to heat generation. In this study, PCM thermal energy storage modules are employed as thermal sinks to absorb heat from these electronic components. These TES modules are placed between electrical components and cold plates to act as a thermal buffer between electronics and coolant loop components by absorbing energy from high ramp rate loads. In previous work, a graph-based model was developed to facilitate control-oriented modeling of a PCM TES module in the latent heating mode [42]. In this work, the graph-based model of the TES module is modified to include both latent and sensible heating modes of the PCM.

To develop such a control-oriented model, several assumptions must be made to condense the PCM thermal dynamics into only the most relevant quantities. The TES module is approximated by a single lumped model, in which it is assumed that the temperature remains constant spatially throughout the entire module. Additionally, it is assumed that the temperature of the electronic component associated with each TES module is spatially invariant on the surface between the TES module and electronic component. Under these assumptions, performing an energy balance on the TES module yields the following

$$\dot{E}_{PCM} = Q_{in} - \frac{1}{R_u}(T_{PCM} - T_2),$$
(2.38)

where $E_{PCM} = E_L + E_S$ is the instantaneous amount of total energy stored in the PCM (i.e., the sum of latent energy stored E_L and sensible energy stored E_S), Q_{in} is the heat generated by the electrical component, R_u is the thermal resistance between the TES module and the electrical

component, T_{PCM} is the lumped temperature of the TES module, and T_2 is the temperature of the thermal component to which the TES module is attached (in this case, T_2 is the temperature of the cold plate wall). The temperature of the TES module is clearly a function of the energy stored, and the phase change phenomena causes this relationship to be nonlinear. In particular, the PCM temperature is given by the following piecewise linear function

$$T_{PCM}(E_{PCM}) = \begin{cases} T_0 + \dfrac{1}{C} E_{PCM} & \text{if } E_{PCM} \le E_c, \\ T_m & \text{if } E_c < E_{PCM} < E_c + L, \\ T_m + \dfrac{1}{C}(E_{PCM} - E_c - L) & \text{if } E_{PCM} \ge E_c + L, \end{cases} \qquad (2.39)$$

where T_m is the PCM melt temperature, E_c is termed the "critical energy" at which a fully solid PCM first begins to melt, C is the sensible heat capacity of the PCM, L is the latent heat capacity, and T_0 is an arbitrary temperature at which the PCM energy storage is initialized to zero. Graphically, this temperature profile has the shape shown in the upper plot of Figure 2.11, and we note that the shape is dependent on parameters C and L. These parameters are given by $C = mC_p$ and $L = ml$, where m is the PCM mass, C_p is its specific heat capacity, and l is its specific latent heat capacity.
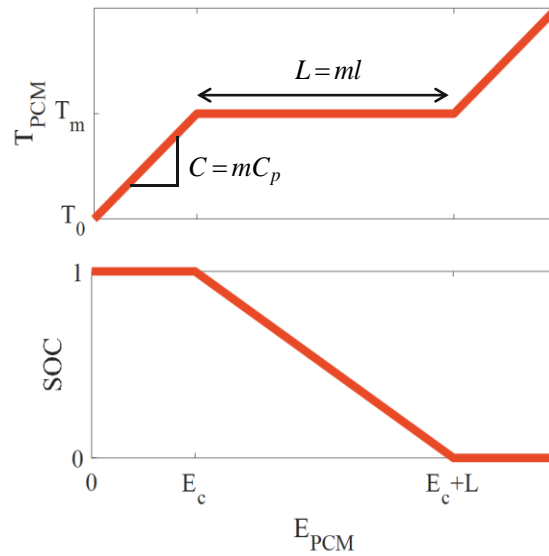
Figure 2.11: Generic form of PCM temperature and SOC profiles.

With the temperature profile defined above, the TES module model in (2.38) is readily translated into the graph-based modeling framework, resulting in the two variants of the TES graph shown in Figure 2.12. In both variants, the energy stored in the PCM is the only state, labeled E_{PCM} in accordance with (2.38). The state variable is chosen to be PCM energy storage rather than temperature because, as demonstrated visually in Figure 2.11, the PCM temperature captures no information about the latent energy storage. If it were desired to choose temperature as the state variable, then another vertex would be necessary to capture information about latent energy storage and relay that information to the temperature state. We opt instead for the simpler formulation of a single lumped energy storage vertex, from which temperature can be determined as a piecewise linear mapping. Note that, while the E_{PCM} vertex has been shaded pink here to reflect its thermal nature, this vertex does not represent a temperature but an amount of energy. In variant a.), source flow e_1^s represents the heat applied to the TES module by an electrical component, previously denoted as Q_{in}. Edge e_1 corresponds to heat transfer between the TES module and adjacent thermal

component which is given by $(T_{PCM} - T_2)/R_u$. Because T_{PCM} is nonlinear, in order to represent this power flow in the form of (2.3), we define

$$g_1(E_{PCM}, T_2) = \frac{(T_{PCM}(E_{PCM}) - T_2)}{R_u} \tag{2.40}$$

as a 2-D mapping that outputs the amount of heat transfer, given values of E_{PCM} and T_2. Setting the coefficient c_{11} in (2.3) equal to one and all other coefficients to zero yields the desired value for edge e_1. Since g_1 is piecewise linear in E_{PCM} and linear in T_2, (2.40) can be implemented using a 2-D lookup table. Note that in this variant of the graph model, the TES module is not affected by the temperature of the adjacent electronic component but rather by the amount of heat generated by the electrical component. Hence this variant is useful when the HESS is not directly modeled, in which case heat generation of the electrical component can be approximated as a constant efficiency loss.
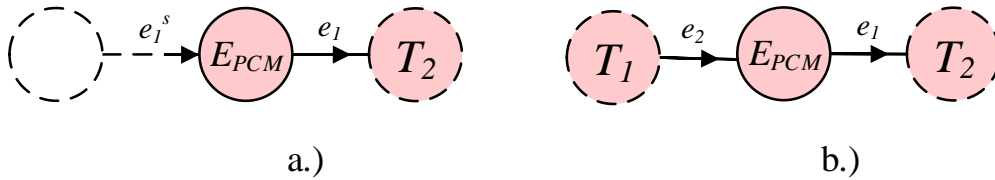
Figure 2.12: Two variants of the TES module graph model.

The second variant of the TES module graph model is shown in Figure 2.12 b.). This variant includes a sink state T_1 to represent the temperature of the adjacent electrical component. Source flow e_1^s is then replaced by edge e_2 which is defined in the same way as e_1. This variant captures electro-thermal coupling and is preferred over variant a.) when modeling the full electro-thermal system. In both of these variants, the state vector is simply $x = E_{PCM}$ and the capacitance

vector is $C = 1$. Note that variant b.) can be generalized for TES modules that cool multiple components by adding sink vertices and edges of the same form and orientation as T_1 and e_2.

The upper plot in Figure 2.11 demonstrates that, in the sensible heating modes for which $E_{PCM} \leq E_c$ or $E_{PCM} \geq E_c + L$, the PCM temperature gives a direct mapping to the amount of energy stored in the PCMs. In the latent mode for which $E_c < E_{PCM} < E_c + L$, however, temperature has no correlation to the amount of energy stored. In this mode, it is useful to define a state of charge (SOC) metric which quantifies the amount of energy stored in the form of latent heat. In the latent heating mode, PCM SOC is analogous to battery SOC. However, an important distinction between PCM SOC and battery SOC is that energy can be stored in a PCM even when the PCM's SOC reaches one through sensible heating, albeit at a slower rate. A battery, on the other hand, can only store energy while its SOC is less than one.

In this work, we define SOC of the PCM according to

$$SOC(E_{PCM}) = \begin{cases} 1 & \text{if } E_{PCM} \leq E_c, \\ 1 - \dfrac{1}{L}(E_{PCM} - E_c) & \text{if } E_c < E_{PCM} < E_c + L, \\ 0 & \text{if } E_{PCM} \geq E_c + L, \end{cases} \qquad (2.41)$$

which is equivalent to the mass fraction of solid PCM. Graphically, SOC has the shape shown in the lower plot of Figure 2.11, which is dependent on PCM mass. Though the SOC is not directly used in the graph-based model, this metric provides an estimate of the amount of latent energy storage remaining in the PCM. This knowledge of latent energy storage is critical for high ramp rate loading profiles, because a low SOC indicates that the PCM has little latent storage remaining and may overheat if large heat loads continue to be applied.

We conclude this section by acknowledging that, because of the low thermal conductivity of many PCMs such as paraffin waxes, the assumptions made to develop this model may neglect

significant thermal gradients in the TES module. In such cases, the graph-based TES model can readily be refined by decomposing the single vertex model into a cluster of connected vertices, each having the same general structure as shown in Figure 2.12 b.), with the interconnections and parameters of these vertex clusters dictated by the desired spatial resolution. In the present case, it is assumed that the thermal conductivity of the PCM is high enough that the assumptions remain valid. One prominent example of a PCM with high thermal conductivity, for which these assumptions remain valid, is a paraffin wax embedded in metal foam.

2.3.6 Cold Plate Heat Exchanger Model

The cold plate heat exchangers are used to recharge the TES modules through convective heat transfer with circulating coolant. The graph model for the cold plate heat exchanger used in this work, shown in Figure 2.13, was introduced in [49] and is reproduced here for completeness.
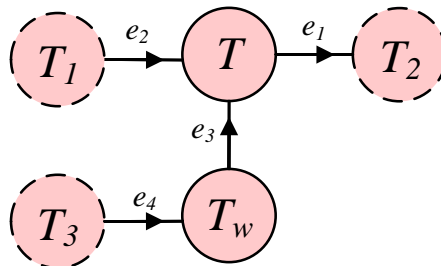
Figure 2.13: Cold plate graph model.

The dynamic of the cold plate wall temperature T_w is given by

$$mC_p\dot{T}_w = \frac{1}{R}(T_3 - T_w) - hA_s(T_w - T) \tag{2.42}$$

where m is the mass of the cold plate wall, C_p is the specific heat capacity of the cold plate wall, T_3 is the temperature of the adjacent TES module, R is the thermal resistance between the cold plate wall and TES module, h is the convective heat transfer coefficient, A_s is the surface area

between the coolant and the cold plate wall, and T is the temperature of coolant at the cold plate outlet. The coolant outlet temperature is given by

$$A_c L \rho C_p \dot{T} = h A_s (T_w - T) + \dot{m} C_p (T_1 - T) \tag{2.43}$$

where A_c is the cross-sectional coolant flow area, L is the length of the flow section, ρ is the coolant density, $\dot{m}$ is the coolant mass flow rate, and T_1 is the temperature of the fluid entering the cold plate from the upstream component. Note that the second term on the right-hand side of (2.43) is an advective heat transfer term which depends on the mass flow rate, which is a controllable input of the thermal system. Similar advective heat transfer terms will be seen in subsequent component models, and all such terms exhibit this dependence on a controllable input.

The state vector and capacitance vector, respectively, are then given by

$$x = [T_w \ T]^T, \tag{2.44}$$

$$C = [m C_p \ A_c L \rho C_p]^T. \tag{2.45}$$

2.3.7 Heat Exchanger Model

A brazed plate heat exchanger is used in this work to reject heat from the coolant loop to a colder sink fluid. The graph model for the parallel flow heat exchanger used in this work, shown in Figure 2.14, was introduced in [49] and is reproduced here for completeness. The two separate flows in the heat exchanger, one of which is the coolant and the other of which is a sink fluid, are referred to in this figure as flows on side a (corresponding to the sink fluid) and on side b (corresponding to the coolant).
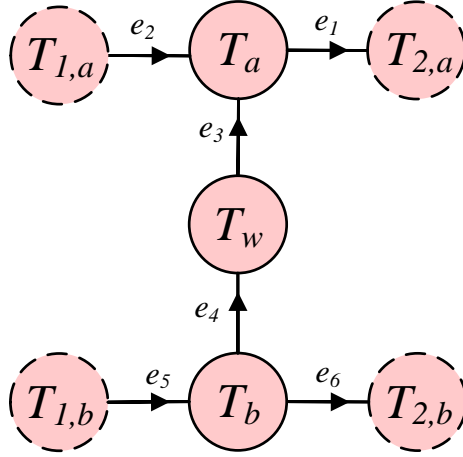
Figure 2.14: Heat exchanger graph model.

The dynamic of the heat exchanger wall temperature T_w is given by

$$mC_p\dot{T}_w = h_b A_b (T_b - T_w) - h_a A_a (T_w - T_a) \tag{2.46}$$

where m is the mass of the heat exchanger wall, C_p is the specific heat capacity of the wall, h_a and h_b are the convective heat transfer coefficients for the fluids on sides a and b of the heat exchanger respectively, A_a and A_b are the heat transfer areas on these respective sides, and T_a and T_b are the temperatures at the fluid outlets of sides a and b respectively. The dynamics of these fluid temperatures are given by

$$A_{c,a} L_a \rho_a C_{p,a} \dot{T}_a = h_a A_{s,a} (T_w - T_a) + \dot{m}_a C_{p,a} (T_{1,a} - T_a) \tag{2.47}$$

$$A_{c,b} L_b \rho_b C_{p,b} \dot{T}_b = \dot{m}_b C_{p,b} (T_{1,b} - T_b) - h_b A_{s,b} (T_b - T_w) \tag{2.48}$$

where $A_{c,a}$ is the cross-sectional fluid flow area of side a, L_a is the length of the flow section in side a, ρ_a is the density of fluid on side a, $C_{p,a}$ is the specific heat capacity of side a, $A_{s,a}$ is the heat transfer surface area for side a, $\dot{m}_a$ is the mass flow rate of fluid in side a, $T_{1,a}$ is the

38

temperature of the fluid at the inlet of side a, and each of these quantities are defined analogously for side b.

The state vector and capacitance vector for the heat exchanger are given by

$$x = [T_b \ T_w \ T_a]^T,$$ (2.49)

$$C = [A_{c,b}L_b\rho_bC_{p,b} \ mC_p \ A_{c,a}L_a\rho_aC_{p,a}]^T.$$ (2.50)

2.3.8 Tank Model

The final thermal component discussed in this section is the fluid tank. As with the heat exchanger and cold plate, the graph model for the tank used in this work, shown in Figure 2.15, was introduced in [49]. In this case, however, the tank graph is modified to include the flow splitting which occurs downstream of the tank in the valve.
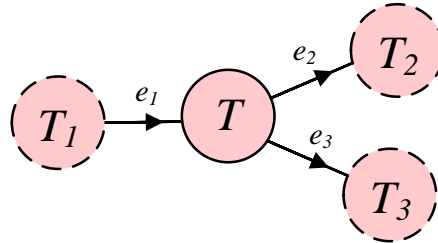
Figure 2.15: Tank graph model.

Neglecting heat lost to the environment, the dynamic of the tank coolant temperature T is given by

$$mC_p\dot{T} = \dot{m}_1C_pT_1 - \dot{m}_2C_pT - \dot{m}_3C_pT$$ (2.51)

where m is the mass of coolant in the tank, C_p is its specific heat, $\dot{m}_1$ is the flow rate entering the tank, T_1 is the temperature of the fluid entering the tank from the upstream component, $\dot{m}_2$ is the flow rate leaving the tank along edge e_2, and $\dot{m}_3$ is the flow rate leaving the tank along edge e_3. The state vector for the tank is then $x = T$ and the capacitance vector is $C = mC_p$.

2.4   Subsystem and System Models

In this section the component models are combined to form subsystems and systems. The subsystem models are presented and discussed first, starting with the electrical subsystem and proceeding to the thermal subsystem. Then the full system model is presented which combines the two subsystems and concludes the section. The methods for combining these component models are presented in [48], and the interested reader is referred to this work for details on the graph combination process.

2.4.1 Hybrid Energy Storage System Model

The graph-based models shown in Section 2.3 for the battery pack, ultracapacitor pack, converters, and voltage bus are combined to form the subsystem model shown in Figure 2.16. Note that for this subsystem, the ultracapacitor is represented as a linear capacitor rather than the third-order model that was the focus of 2.3.2. The linear capacitor model is preferred over the third-order model for the HESS because the effects of slower, higher order dynamics will be negligible for the loads considered in this work, and because the third-order model provides a more accurate model of heat generation that is not necessary when considering only the electrical subsystem. However, since the linear capacitor model does not inherently capture any heat generation in the ultracapacitor, a resistive loss is added on the terminal current state I_{13} to estimate heat generation.

Note that an extra edge has been added between the bus voltage state and the thermal sink state. This edge is added to account for heat generation in the current load and is treated as a resistive loss. Each vertex in this graph is assigned a number according to a global numbering scheme, and these numbers are shown here as subscripts on the labels of the vertices. To clarify where the component models fall into the subsystem graph, Table 2.2 lists these vertex numbers along with a description of the state to which each vertex corresponds within the component models.

Additionally, the edges in Figure 2.16 are color-coded to illustrate the types of power flows occurring along each of the edges. The mathematical formulations for each of these edge types are provided in Table 2.3.
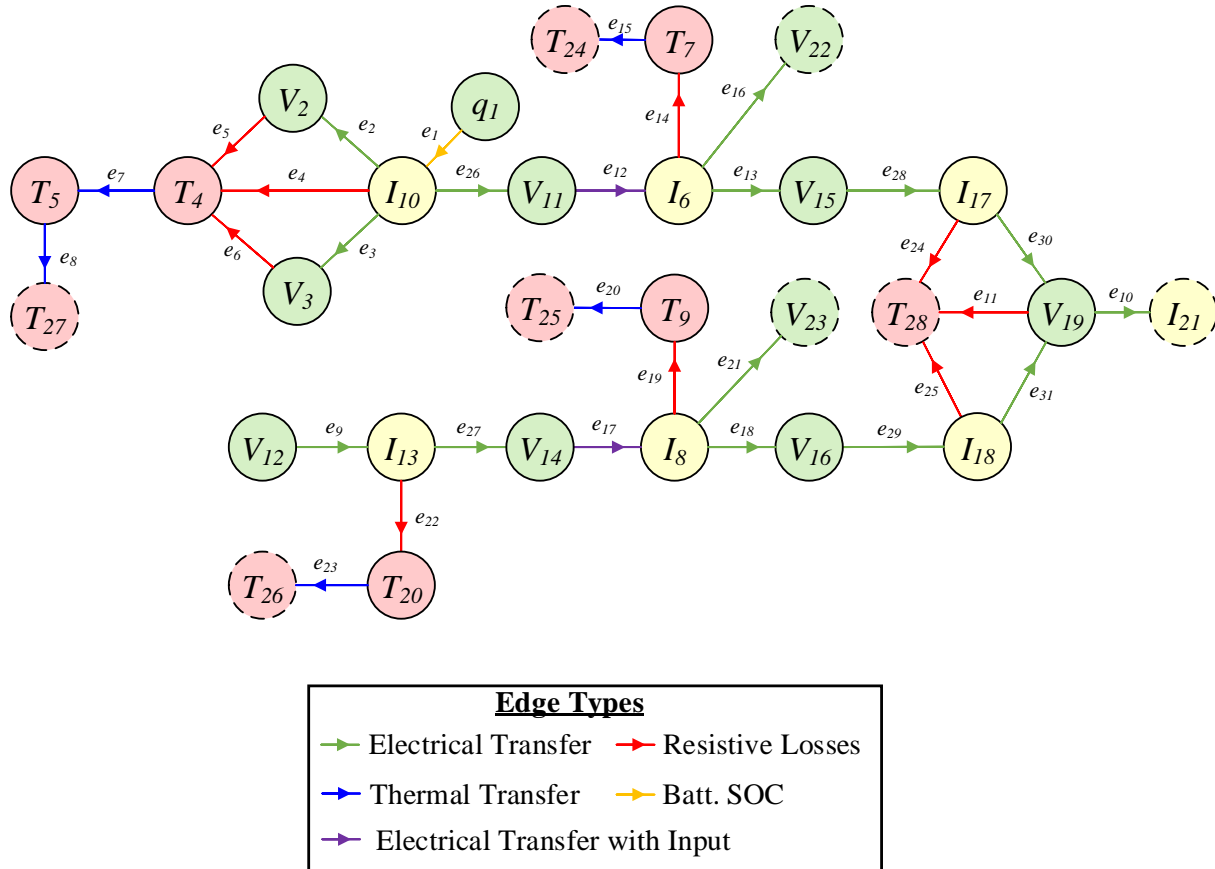
Figure 2.16: HESS graph model.

Table 2.2: HESS vertex labels.

		Vertex Numbers, Corresponding States, and Descriptions						
1	q_1	Batt. q	11	V_{11}	Conv. 1 V_1	21	I_{21}	Bus I_3
2	V_2	Batt. V_1	12	V_{12}	UC V_1	22	V_{22}	Conv. 1 V_3
3	V_3	Batt. V_2	13	I_{13}	UC I_1	23	V_{23}	Conv. 2 V_3
4	T_4	Batt. T_1	14	V_{14}	Conv. 2 V_1	24	T_{24}	Conv. 1 T_2
5	T_5	Batt. T_2	15	V_{15}	Conv. 1 V_2	25	T_{25}	Conv. 2 T_2
6	I_6	Conv. 1 I_1	16	V_{16}	Conv. 2 V_2	26	T_{26}	UC T_2
7	T_7	Conv. 1 T_1	17	I_{17}	Bus I_1	27	T_{27}	Batt. T_3
8	I_8	Conv. 2 I_1	18	I_{18}	Bus I_2	28	T_{28}	Bus T_1
9	T_9	Conv. 2 T_1	19	V_{19}	Bus V_1			
10	I_{10}	Batt. I_1	20	T_{20}	UC T_1			

Table 2.3: HESS graph edge definitions.

Edge Type	Edge Definition	Corresponding Edge Numbers
Electrical transfer	$P_j = x_j^{tail} x_j^{head}$	2, 3, 9, 10, 13, 16, 18, 21, 26, 27, 28, 29, 30, 31
Resistive losses	$P_j = \alpha_j (x_j^{tail})^2$	4, 5, 6, 11, 14, 19, 22, 24, 25
Thermal transfer	$P_j = \alpha_j (x_j^{tail} - x_j^{head})$	7, 8, 15, 20, 23
Battery SOC	$P_j = V_{ocv}(x_j^{tail}) x_j^{head}$	1
Electrical transfer with input	$P_j = u_k x_j^{tail} x_j^{head}$	12, 17

2.4.2 Thermal Energy Storage System Model

      The graph-based models shown in Section 2.3 for the TES modules, cold plates, heat exchanger, and tank are combined to form the TESS graph model shown in Figure 2.17. In the TESS, the electrical component temperatures are not modeled, so the TES models considered in this subsystem correspond to variant a.) in Figure 2.12. As in the electrical subsystem, each vertex in this graph is assigned a number according to a global numbering scheme, and these numbers are shown here as subscripts on the labels of the vertices. Table 2.4 lists these vertex numbers along with a description of the state to which each vertex corresponds within the component models. Additionally, the edges in Figure 2.17 are color-coded to illustrate the types of power flows occurring along each of the edges. The mathematical formulations for each of these edge types are provided in Table 2.5. Note that the conduction edges between vertices 8 and 7, 9 and 10 represent conduction between the TES modules and cold plates. As discussed in 2.3.5 these edges are implemented as a 2-D mapping of the PCM energy and cold plate wall temperature. The source edges e_1^s and e_2^s are not included in Table 2.5 as their corresponding power flows are defined as surrogates for the heat generated by the HESS.

42
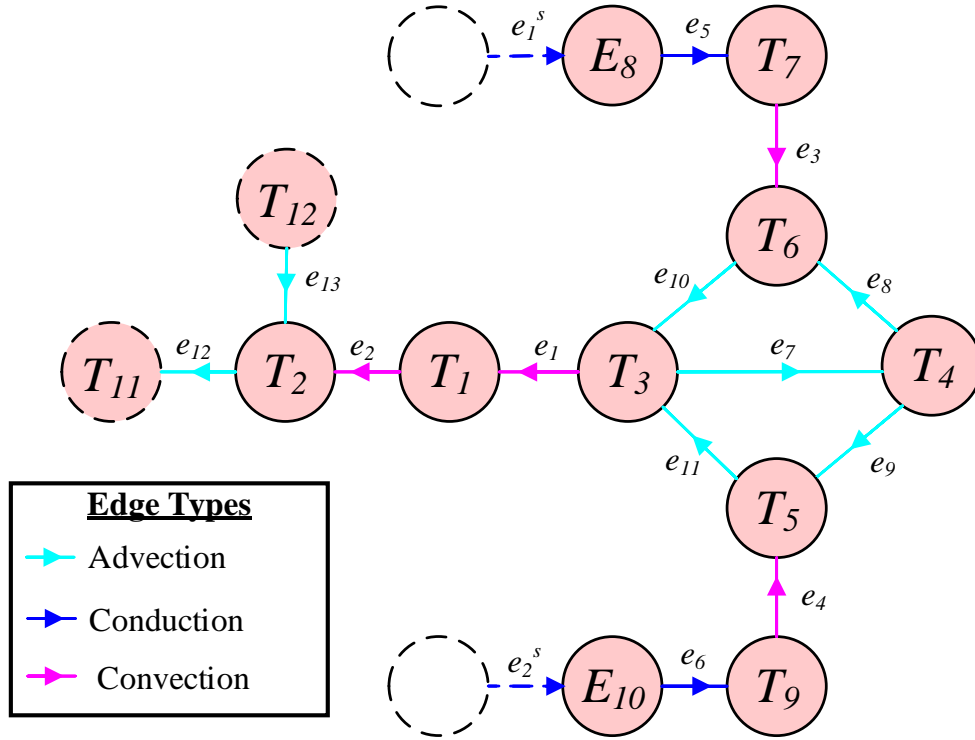
Figure 2.17: TESS graph model.

Table 2.4: TESS vertex labels.

Vertex Numbers, Corresponding States, and Descriptions						
1	T_1	HX T_w	7	T_7	CP1 T_w
2	T_2	HX T_a	8	E_8	TES1 E_{PCM}
3	T_3	HX T_b	9	T_9	CP2 T_w
4	T_4	Tank T	10	E_{10}	TES2 E_{PCM}
5	T_5	CP2 T	11	T_{11}	HX $T_{2,a}$
6	T_6	CP1 T	12	T_{12}	HX $T_{1,a}$

Table 2.5: TESS graph edge definitions.

Edge Type	*Edge Definition*	*Corresponding Edge Numbers*
Advection	$P_j = \alpha_j u_j x_j^{tail}$	7, 8, 9, 10, 11, 12, 13
Conduction	$P_j = \alpha_j (x_j^{tail} - x_j^{head})$	5, 6
Convection	$P_j = \alpha_j (x_j^{tail} - x_j^{head})$	1, 2, 3, 4

2.4.3 Hybrid Electro-Thermal Energy Storage System Model

With a few modifications, the electrical and thermal subsystems are combined to form the hybrid electro-thermal energy storage system graph model shown in Figure 2.18. A significant modification to the HESS model is the replacement of the ideal ultracapacitor model used previously with the higher-fidelity third-order model described in 2.3.2. The third-order ultracapacitor model is preferred in the HETESS model to obtain a more accurate formulation for heat generation and thermal dynamics of the ultracapacitor. Additionally, the edge connecting the bus voltage state V_{19} to the thermal sink state T_{28}, which was introduced to account for heat generation of the load, is replaced by a resistive loss acting directly on the load current I_{21}. Thermal state T_{24} is then introduced to model the temperature dynamic of the load in response to this resistive loss.

In the TESS, a third TES module and cold plate are included for cooling of the power converters, so that the power converters can be thermally separated from the energy storage components. This additional TES module is represented by the vertex labeled E_{25}, the wall temperature of the additional cold plate by T_{40}, and the fluid outlet temperature of the additional cold plate by T_{41}. Additionally, the TES modules are modeled using variant b.) of Figure 2.12. For TES modules 1 and 3, the TES module model is modified as discussed in Section 2.3.5 to allow each of these TES modules to cool multiple components at different temperatures.

As in Sections 2.4.1 and 2.4.2, the vertices and their respective descriptions are tabulated in Table 2.6. The edge numbers are omitted from Figure 2.18, but the edge types are illustrated using the same color-coding scheme as before.
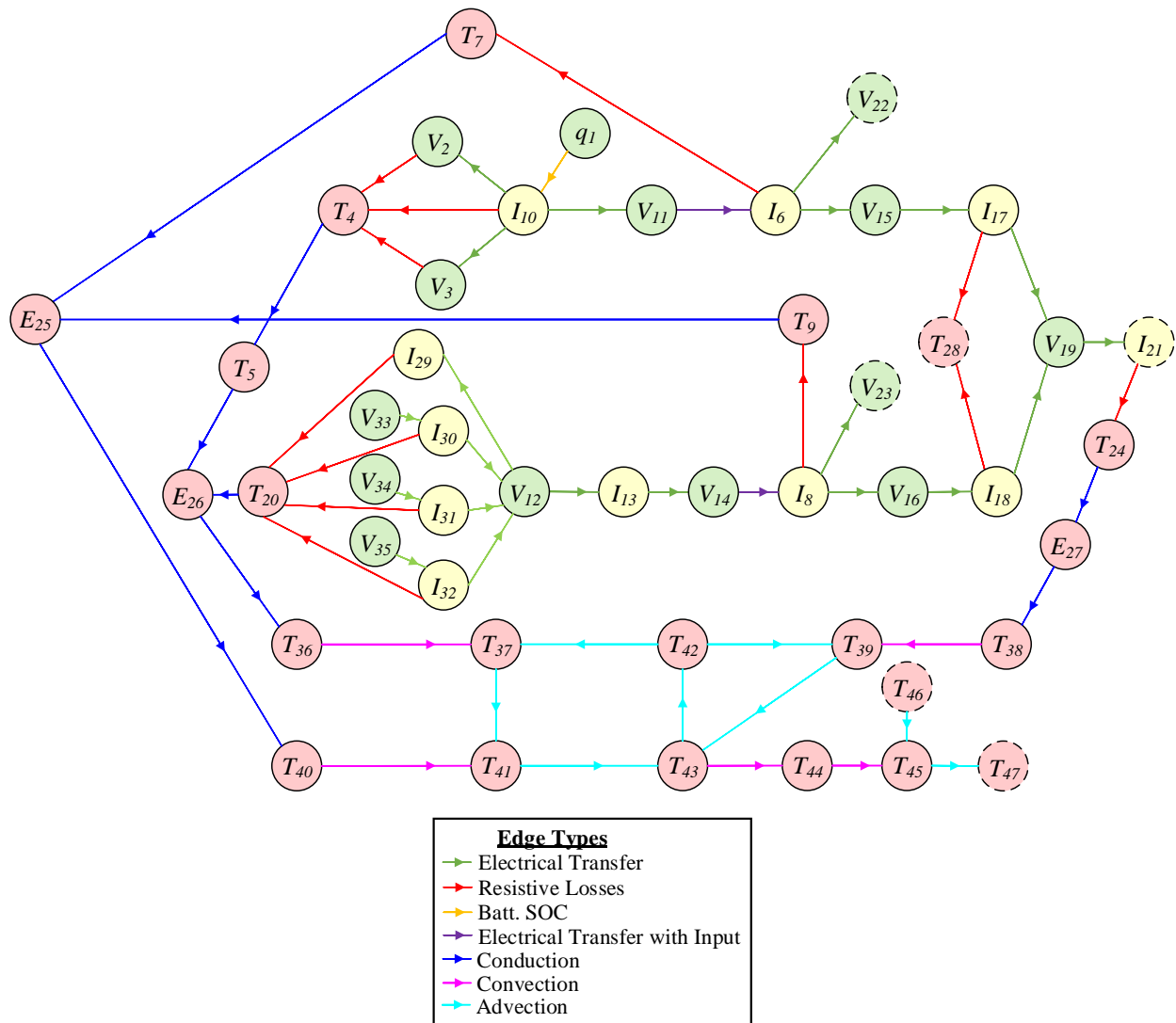
44

Figure 2.18: HETESS graph model.

Table 2.6: Hybrid electro-thermal energy storage system vertex labels.

		Vertex Numbers,			*Corresponding States, and Descriptions*			
1	q_1	Batt. q	17	I_{17}	Bus I_1	33	V_{33}	UC V_i
2	V_2	Batt. V_1	18	I_{18}	Bus I_2	34	V_{34}	UC V_D
3	V_3	Batt. V_2	19	V_{19}	Bus V_1	35	V_{35}	UC V_L
4	T_4	Batt. T_1	20	T_{20}	UC T_1	36	T_{36}	CP1 T_w
5	T_5	Batt. T_2	21	I_{21}	Bus I_3	37	T_{37}	CP1 T
6	I_6	Conv. 1 I_1	22	V_{22}	Conv. 1 V_3	38	T_{38}	CP2 T_w
7	T_7	Conv. 1 T_1	23	V_{23}	Conv. 2 V_3	39	T_{39}	CP2 T
8	I_8	Conv. 2 I_1	24	T_{24}	Load T	40	T_{40}	CP3 T_w
9	T_9	Conv. 2 T_1	25	E_{25}	TES3 E_{PCM}	41	T_{41}	CP3 T
10	I_{10}	Batt. I_1	26	E_{26}	TES1 E_{PCM}	42	T_{42}	Tank T
11	V_{11}	Conv. 1 V_1	27	E_{27}	TES2 E_{PCM}	43	T_{43}	HX T_b
12	V_{12}	UC V_1	28	T_{28}	Bus T_1	44	T_{44}	HX T_w
13	I_{13}	UC I_1	29	I_{29}	UC I_{leak}	45	T_{45}	HX T_a
14	V_{14}	Conv. 2 V_1	30	I_{30}	UC I_i	46	T_{46}	HX $T_{1,a}$
15	V_{15}	Conv. 1 V_2	31	I_{31}	UC I_D	47	T_{47}	HX $T_{2,a}$
16	V_{16}	Conv. 2 V_2	32	I_{32}	UC I_L			

As discussed previously, the HESS and TESS exhibit some similarities in structure, in that they each contain a storage component that can provide or store energy at a very fast rate for intermittent periods, and another component which can store or move energy continuously at a lower rate. The graph model in Figure 2.18 demonstrates some relevant differences in structure between the HESS and TESS. The most apparent difference, apart from the difference in domains, lies in the general direction in which power moves: the HESS supplies electrical power to a load, while the TESS absorbs thermal loads generated by the HESS. Additionally, by design, the configuration of the "slow" and "fast" components within the two subsystems varies in terms of how power moves between the storage components and the load. In the HESS, the battery and ultracapacitor are configured such that these components move power in a parallel manner to the load. In the TESS, thermal loads impact the system in a serial manner, entering the subsystem in the TES modules, then circulating through the coolant loops to the heat exchanger where thermal loads are ultimately rejected to a sink fluid. This structural difference is accentuated in Figure 2.18

by the location of control-dependent edges. In the HESS, the control-dependent edges (shown in purple) are in parallel locations between the storage elements and the electrical load. In the TESS, the advective heat transfer edges are control-dependent, and these edges are located between the TES modules and the heat exchanger. Hence, in the HESS system, the control dictates how each storage element supplies power in parallel to the electrical load, while in the TESS system, the control dictates the rate at which heat is moved serially from the TES modules to the heat sink.

Building the graph model of the hybrid electro-thermal energy storage system demonstrates several of the advantages of the graph-based modeling framework mentioned earlier. The component models, which were combined to form subsystems and then to form an integrated system, demonstrate the modularity of the models and the ability to "plug and play" with different components within the same system or subsystem. The straightforward combination of dynamic electrical and thermal components in a unified modeling scheme highlights the domain-agnostic nature of the modeling framework. The variable fidelity capabilities of the framework were emphasized in Section 2.3.5, in which it was seen that the TES module model could be refined to obtain spatial resolution in the PCM temperature profiles, and in this section, in which ultracapacitor models of varying fidelity are interchanged. The scalability and computational efficiency aspects of the graph-based scheme will be demonstrated in subsequent chapters.

CHAPTER 3.   CONTROL

Controller design is a vital element of the design of electro-thermal systems, particularly in the context of energy storage systems which are sensitive to electrical and thermal operating conditions. In order to ensure adequate dynamic performance, optimal designs of these systems should consider not just the size of the energy storage system, but also the performance of the controller and the ability of the controller to achieve the particular requirements of the system or subsystem under study. In this work, the HESS and TESS have different control objectives and as such they are each equipped with their own dedicated control architecture.

Many researchers have considered the challenge of controller development to determine the power split for battery-ultracapacitor HESSs. These control strategies can be divided into two general categories: heuristic and optimal control strategies. Rule-based HESS control strategies, such as [57], use logic to determine the mode of operation among a set of heuristically derived rules. In [57], a rule-based controller was developed with the objectives of prolonging battery life and maximizing the overall drive train efficiency. Filter-based HESS control strategies, such as [58]–[60], are heuristic strategies which seek to protect the battery from high discharge rates by controlling the battery to provide the low-pass-filtered value of the load power. Optimal strategies use optimization or optimal control techniques, such as linear programming [9], dynamic programming [61], [62], and model predictive control (MPC) [61], [63], [64], to optimize certain objectives, the most common of which are extension of battery life and minimization of power losses [65].

Few researchers have examined thermal management consisting of PCM-integrated liquid cooling for hybrid electrical energy storage systems. Such thermal management systems have been considered extensively for the similar case of battery-only energy storage systems, but few have

considered control of the fluid flow rate. In [37], it was determined that the temperature of coolant through the PCM had a significant impact on the performance of the thermal management system. In [66], it was found that varying the flow rate of coolant, rather than holding the flow rate constant, can improve the temperature distribution of the battery pack, emphasizing the need for flow rate control. On the other hand, many works have examined control strategies for liquid/two-phase cooling systems with integrated TES excluding the dynamics of electrical components. A hybrid hierarchical MPC formulation for a similar coolant loop architecture was performed in [42], wherein the coolant flow rate through each loop was controlled to track a reference for the TES SOC. In [67], an MPC formulation is used to maximize the efficiency of the compressor in a two-phase coolant loop, while a mix of proportional and proportional-integral controllers regulate component temperatures to charge and discharge the TES efficiently. Many researchers have applied control techniques to manage TES systems in other applications, such as buildings and solar plants. Some of these have examined heuristic control strategies such as proportional, integral, and derivative (PID) control and rule-based control to manage coolant temperatures [68]–[70]. Other studies have applied optimal control strategies to manage TES systems for building applications [70]–[73].

With the ultimate goal of this work being multi-objective design optimization, which is a computationally taxing process when dynamic simulations are involved, the solution time of the controller is an important consideration. While optimal control formulations, such as those discussed above for the HESS, offer improved performance over other classical control strategies, these formulations add significantly to the computational expense of a dynamic simulation through the introduction of an optimization subroutine. Incorporating optimal control formulations in a dynamic simulation increases the time to explore the overall design space and may render the

optimization routine intractable for large optimization problems. Therefore, to mitigate the computational expenses added by a controller, heuristic proportional-integral (PI) control strategies are employed in both subsystems for this work.

For the HESS, a filter-based strategy similar to the one proposed in [58] is adopted to control the battery-ultracapacitor hybrid. For the TESS, a PI control strategy is developed which controls the fluid temperatures through the TES modules by adjusting mass flow rates. The HESS and TESS controllers are introduced in this chapter, followed by simulation results that demonstrate the operation of the controllers.

3.1   HESS Controller Design

The two control objectives for the HESS controller are protection of the battery from high discharge rates and maintaining the bus voltage. To accomplish these objectives, a control strategy similar to the one presented in [58] is chosen. Particularly, two decoupled PI controllers are employed which dictate the control inputs (duty cycles) for the DC-DC converters to meet these control objectives.

3.1.1 Battery controller

The controller for the battery subsystem prevents the battery from supplying high discharge rates using a filter-based strategy. The objective of this controller is to ensure that the battery pack provides the smoothed average value of the power requirement of the electrical load. Passing the power profile of the electrical load through a low-pass filter achieves this averaging of the load profile by attenuating high-frequency fluctuations, particularly those introduced by the high ramp rate load. Hence, a transfer function with a cutoff frequency of 0.0475Hz is applied to the load power profile to obtain the low-pass filtered value of the load power. The value of this cutoff frequency was selected heuristically to be smaller than 50% of the 0.1Hz frequency of the high

ramp rate load to significantly attenuate the high ramp rate variations. Specifically, the filtered

value of the load power is given by

$$P_{filt} = \frac{1}{s^2 + 20s + 0.95} P_{load} \tag{3.1}$$

where P_{load} is the load power and P_{filt} is its filtered value.

The filter's ability to attenuate high ramp rate disturbances is examined by comparing P_{load}

and P_{filt}. For this work, a 30-minute current load profile consisting of low frequency variations

and high ramp rate disturbances is considered. We will show in the following section that the bus

voltage is controlled to remain near a reference value, so in the remainder of this section the load

power is estimated as the product of this current load profile and the reference bus voltage. The

high ramp rate disturbances to the load power profile act intermittently on the low frequency

variations during the time periods from 9 minutes to 11.5 minutes, and from 22 minutes to 25.5

minutes in the simulation time frame. During these time periods, the disturbances ramp up and

down once every 10 seconds at a rate of 55kW/s remaining at their maximum value for 0.5s,

resembling pulses of power. With the energy demands of each of these bursts totaling around 80kJ,

the high ramp rate disturbances are somewhat representative of the loads required by an

electromagnetic launcher for small to medium sized UAVs, such as the prototype launcher

described in [74]. The electrical load profile used in this work is shown in Figure 3.1 along with

the filtered value of the load power, demonstrating the attenuating performance of the filter given

by (3.1). The filter attenuates the high ramp rate disturbances by 80%. This filtered load power

gives a much safer power demand for the battery pack by significantly reducing the magnitude of

the high ramp rate power disturbances. Note that the DC gain of the filter described in (3.1) is

greater than unity, causing a 5% offset between the steady-state values of the filtered and estimated load power. This allows for the battery pack to account for electrical losses in the HESS.
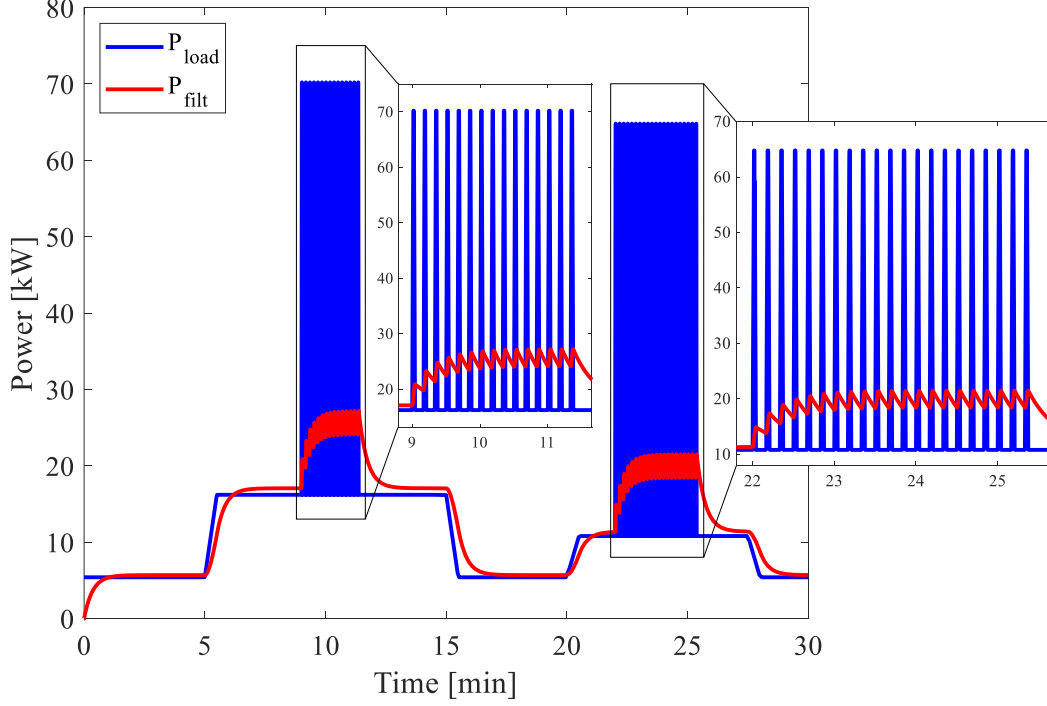
Figure 3.1: Electrical load power and filtered load power.

With the filtered power profile given by (3.1) and shown in Figure 3.1, the battery controller compares the power provided by converter 1 (P_{DCDC1}) to this reference filtered load profile. The error between these two signals, given by

$$e_1 = P_{filt} - P_{DCDC1}, \tag{3.2}$$

is sent through a PI controller, which yields the following control signal

$$u_1 = (K_{p1} + K_{i1} / s)e_1, \tag{3.3}$$

where K_{p1} is the proportional gain of the PI controller and K_{i1} is the integral gain. The resulting control signal u_1 is saturated between 0 and 1 and used as the duty cycle for converter 1. This saturation can lead to integral windup if the pre-saturated control signal greatly exceeds its bounds.

52

In this work, the amount by which the pre-saturated control signal exceeds its bounds is minimal, so a simple clamping strategy is sufficient to mitigate integral windup rather than a more formal method. This control strategy is demonstrated conceptually by the block diagram in Figure 3.2.
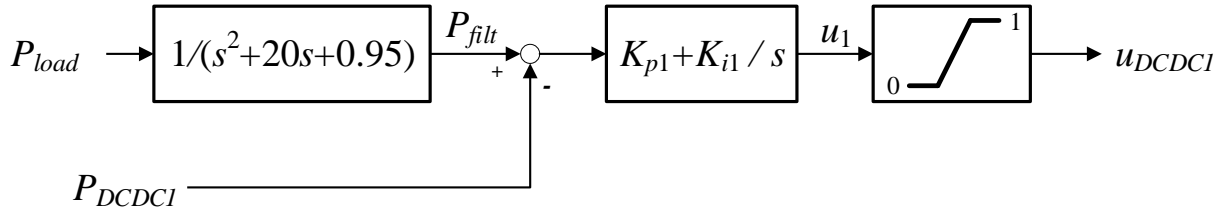
Figure 3.2: HESS converter 1 control block diagram.

3.1.2 Ultracapacitor controller

The controller for converter 2 is then tasked with maintaining the bus voltage at a reference value. In this study the reference value for the bus voltage (V_{ref}) is chosen to be 270V to suit the demands of the UAV launch system. Maintaining the bus voltage at this reference value is accomplished simply by finding the error between the bus voltage V_{bus} and reference voltage

$$e_2 = V_{ref} - V_{bus} \tag{3.4}$$

and applying PI control, yielding the following control signal

$$u_2 = (K_{p2} + K_{i2} / s)e_2, \tag{3.5}$$

where K_{p2} is the proportional gain of the PI controller and K_{i2} is the integral gain. As with converter 1, the resulting control signal u_2 is saturated between 0 and 1 and used as the duty cycle for converter 2. A clamping strategy is again used to mitigate integrator windup, as the pre-saturated control signals do not significantly exceed their bounds. This control strategy is demonstrated conceptually by the block diagram in Figure 3.3.

V_{ref} +   − $K_{p2}+K_{i2}/s$ u_2 0   1 u_{DCDC2}

V_{bus}
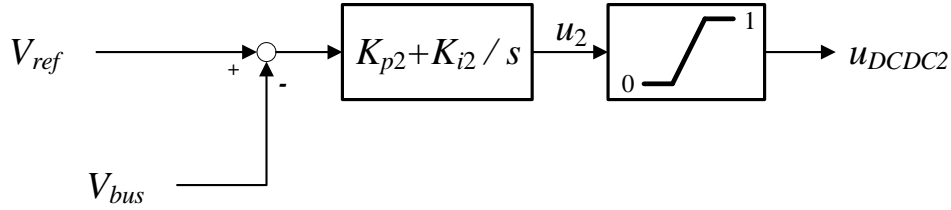
Figure 3.3: HESS converter 2 control block diagram.

3.1.3 Closed-loop HESS simulation results

To demonstrate the performance of the HESS control strategy, the controllers defined above are applied to the HESS model described in 2.4.1. The particular set of values of sizing and control parameters for which this simulation is performed, referred to hereafter as the nominal values of these parameters and gains, is given in Table 3.1. The nominal HESS system is simulated under the same current load profile introduced in 3.1.1 for the analysis of the filtered load power.

Closed-loop simulation results for selected signals are shown in Figure 3.4. The upper row of plots shows the SOC and voltage of the battery pack and ultracapacitor pack. The SOC of the ultracapacitor pack here is defined as the ratio of the ultracapacitor voltage to its maximum voltage. To maximize their energy storage capabilities without risking over-charging, the battery and ultracapacitor packs are initialized at SOC near but not equal to one. The middle plots highlight the performance of the control strategy by comparing the reference values of the controllers to the simulated values. The middle left plot shows that the controller for converter 2 is maintaining the bus voltage within 1 volt of the reference, and the middle right plot shows that the battery power is closely tracking the filtered load power. The lower plots show the duty cycles applied to the two converters to achieve this performance and the resulting currents of each of the system components, with the load current shown in gray. See the appendix for magnified views of each of the subplots in this figure.

54
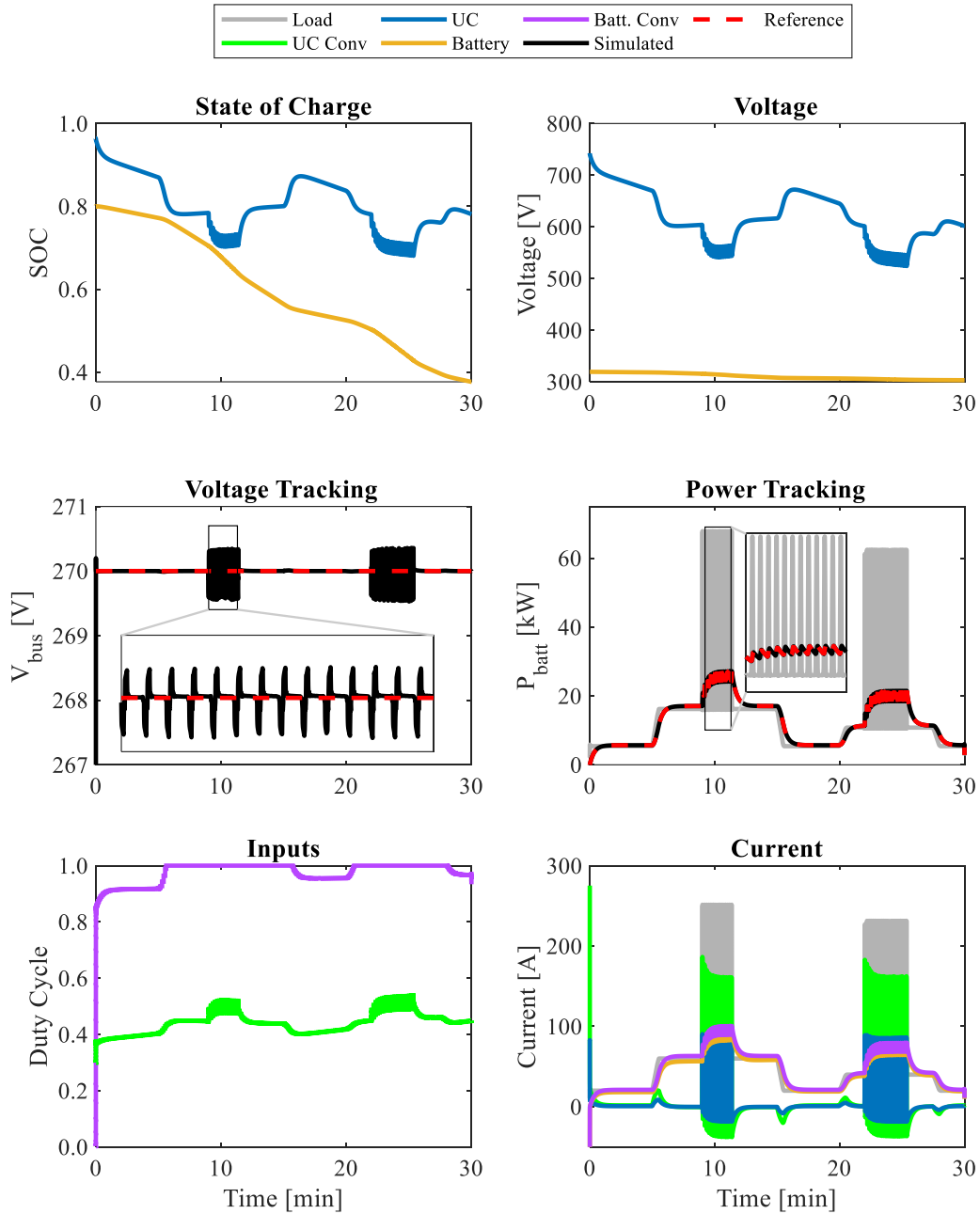
Figure 3.4: Closed-loop HESS simulation results.

Table 3.1: Nominal HESS sizing and control parameters.

| Number of Cells		Controller Gains	
Series (battery)	80	K_{p1} (battery)	0.00001
Parallel (battery)	10	K_{i1} (battery)	0.0001
Series (UC)	275	K_{p2} (UC)	0.004
Parallel (UC)	15	K_{i2} (UC)	0.1

3.2   TESS Controller Design

The control objective for the TESS controller is to maintain the fluid temperature through the cold plates such that the coolant remains colder than the melt temperature of the respective PCM. This is accomplished by varying the mass flow rates through the flow loops to vary the rate at which heat is absorbed from the TES modules and subsequently rejected to the sink fluid in the heat exchanger. Note that the flow rates through the two flow loops (through cold plate 1 and through cold plate 2) are coupled in that their sum is the total mass flow rate in the system. The pump, which drives mass flow in the system, dictates this total flow rate. Hence the selected control strategy for the pump couples the temperature effects of the two flow sections. The valve setting is then chosen to proportion the total flow rate appropriately between the two flow sections.

3.2.1 Pump Controller

The controller for the pump consists of two PI controllers corresponding to each of the two flow sections. One controller aims to regulate the temperature at the outlet of cold plate 1 to a reference value, and the other aims to regulate the temperature at the outlet of cold plate 2 to another reference value. These references are chosen to be 10°C below the melt temperature of the respective PCM. Each controller compares the actual temperature at the cold plate outlet to the respective reference temperature and applies PI control to the error between these two values. The two resulting control signals are summed so that the resulting signal contains the summed contributions of the two controllers. This signal is used as the duty cycle for the pump, which dictates the total mass flow rate. The duty cycle is saturated in accordance with the physical limitations of the pump. In this work, the duty cycle of the pump is allowed to vary continuously between 0% and 65%. Prior to summing the individual contributions of the two controllers, these contributions are saturated between 0% and 65% as well, employing a clamping strategy to

56

mitigate windup in the integral terms of the individual controllers. The control strategy for the pump is demonstrated by the block diagram shown in Figure 3.5.
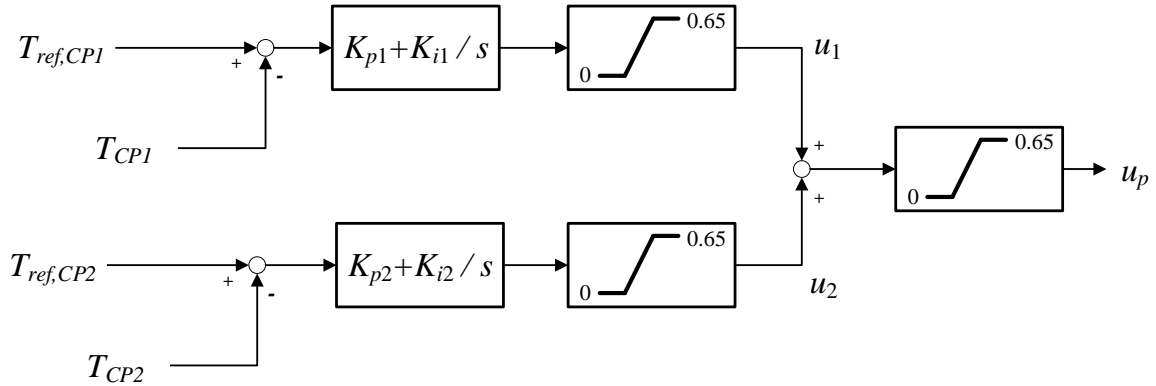
Figure 3.5: TESS pump control block diagram.

3.2.2 Valve Setting

With the pump dictating the total flow rate through the coolant loops, the valve is responsible for proportioning flow appropriately between the two flow sections. The valve is modeled as a solenoid valve, and its dynamics are assumed to be faster than the timestep of the simulation. Hence the valve setting is assumed to occur instantaneously, and is defined according to

$$u_v = \frac{u_1}{u_1 + u_2}, \tag{3.6}$$

where u_1 and u_2 are the saturated contributions of the two individual controllers shown in Figure 3.5, and u_v is the valve setting. The mass flow rates through the two sections are then given by

$$\dot{m}_1 = u_v \dot{m}_{total},$$
$$\dot{m}_2 = (1 - u_v)\dot{m}_{total}, \tag{3.7}$$

57

where $\dot{m}_1$ is the flow rate through cold plate 1, $\dot{m}_2$ is the flow rate through cold plate 2, and $\dot{m}_{total}$ is the total mass flow rate. This choice of valve setting directs a larger portion of the total flow rate to travel through one of the cold plates when its temperature exceeds its reference.

3.2.3 Closed Loop TESS Simulation Results

To demonstrate the performance of the TESS control strategy, the controller defined above is applied to the TESS model described in 2.4.2 under the nominal set of sizing parameters and controller gains given in Table 3.2. As mentioned in 2.1, the thermal loads for the TESS system are defined such that the load applied to cold plate 1 is a surrogate for heat generation of the storage elements and power converters, while the load applied to cold plate 2 is a surrogate for heat generation of the electronic load. Particularly, the thermal load generated by each electrical component is estimated as a small percentage of the magnitude of electrical power output by that component. This percentage is taken to be 20% for the electrical load which is assumed to be the most inefficient component, 10% for the battery pack and converters, and 1% for the ultracapacitor which is assumed to be the most efficient component due to its low internal resistance. The thermal load applied to cold plate 1 is the sum of the estimated thermal loads of the battery pack, converters, and ultracapacitor pack. Denoted Q_{in1} and Q_{in2}, the thermal loads applied to cold plates 1 and 2 respectively are shown in Figure 3.6.

Table 3.2: Nominal TESS sizing and control parameters.

Sizing Parameters		Controller Gains	
Mass [kg] (TES1)	10	K_{p1} (TES1)	20
Melt Temp. [°C] (TES1)	45	K_{i1} (TES1)	1
Mass [kg] (TES2)	8.5	K_{p2} (TES2)	20
Melt Temp. [°C] (TES2)	50	K_{i2} (TES2)	1
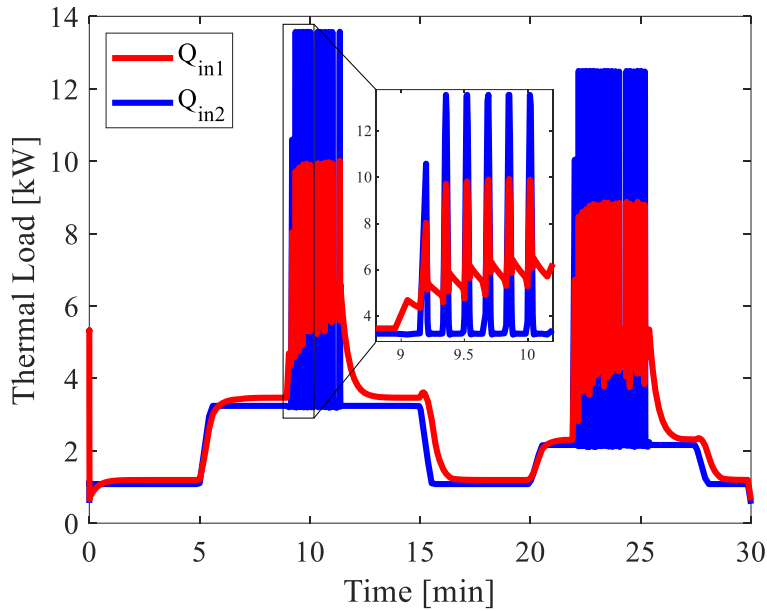
Figure 3.6: TESS load profiles.

Closed-loop simulation results of the TESS system from 2.4.2 under these load profiles are shown in Figure 3.7. All components in the TESS are initialized at a steady state temperature of 30°C. The left two plots show the temperatures and states-of-charge of the PCMs in the two TES modules in response to the given load profiles, demonstrating the performance of the graph-based TES module model. Over the course of the 30-minute simulation, the PCMs are heated sensibly until they reach their respective melting temperatures. At this point, the PCMs continue to absorb energy by changing phase from solid to liquid, gradually lowering the SOC of the TES modules. Once the SOC of each PCM reaches zero, the PCM continues to absorb thermal energy through sensible heating, reaching peak temperatures of 69°C and 61°C in TES1 and TES2 respectively. The right two plots show the reference tracking ability of the controller and the mass flow rates used in order to achieve this reference tracking. The controllers are inactive during the first few minutes while the cold plate temperatures heat up to reach their reference temperatures. Once the reference temperatures are met, the pump begins to drive coolant flow through the system, with

more coolant being directed through CP1 because its reference temperature is lower. As the PCMs are heated sensibly beyond their melting temperature, this causes the cold plate temperatures to increase, forcing the pump to supply higher mass flow rates to bring the cold plate temperatures to their reference values. See the appendix for magnified views of each of the subplots in this figure.
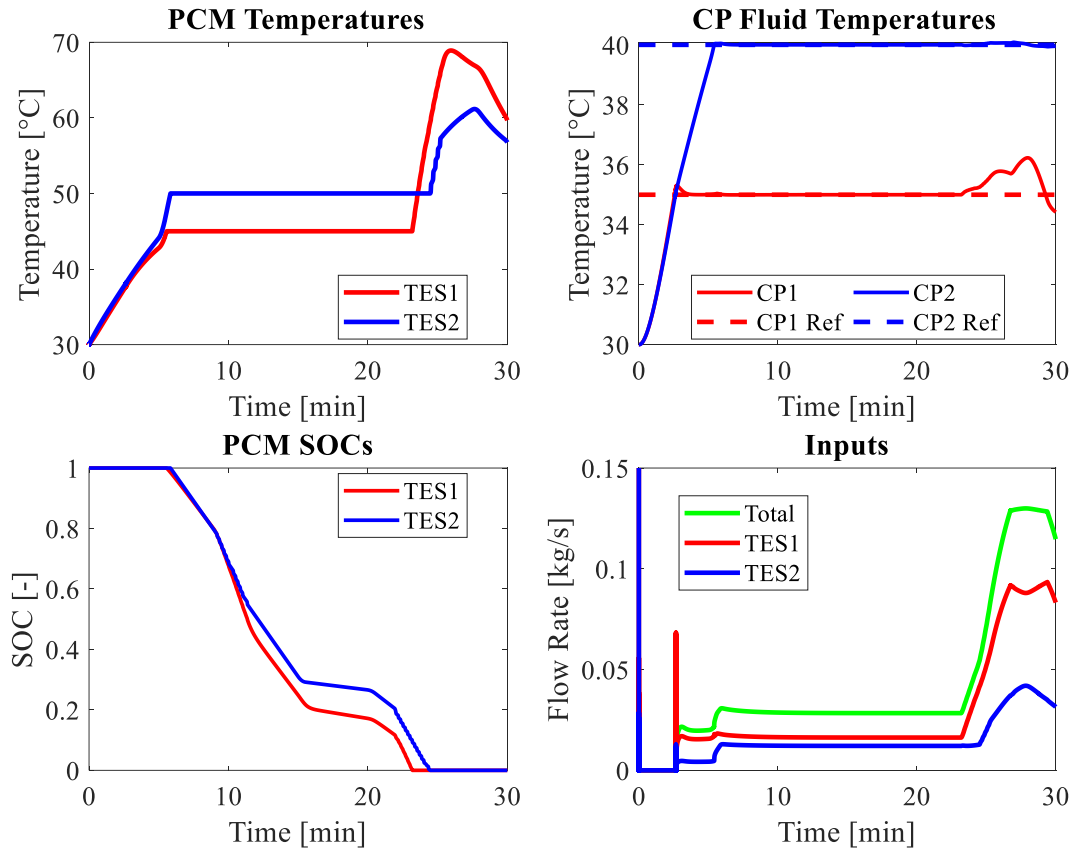

Figure 3.7: Closed-loop TESS simulation results.

3.3   Closed-Loop HETESS Simulation Results

The closed-loop hybrid electro-thermal energy storage system is obtained by applying the controllers described above to the model introduced in 2.4.3. Due to intrinsic model differences between the HETESS and the HESS and TESS subsystem models, a different nominal parameter

set is considered for the sizing of the nominal electro-thermal system. These sizing parameters are provided in Table 3.3. The control parameters are unchanged from their prior values.

Closed-loop simulation results of the HETESS in response to the electrical load shown in 3.1.3 are provided in Figure 3.8. The upper half of this figure contains trajectories of HESS signals, while the bottom half contains trajectories of TESS signals. The top row of plots shows the voltage and current profiles of components in the HESS. Comparing these trajectories to the corresponding trajectories in Figure 3.4 highlights the differences in voltage behavior between the first-order and third-order ultracapacitor models. Simulated temperatures of the electronic components are shown in the right-hand plot in the second row. In this plot, the battery core temperature is plotted as a solid tan trace, while the battery shell temperature is plotted as a dashed tan trace. The temperature profiles in this plot demonstrate that the load is the most inefficient component, followed by the converters, the battery pack, and the ultracapacitor pack. The trajectories of the PCM temperatures and SOCs show that, for the nominal system, the temperatures of the energy storage components do not increase significantly. This suggests that the estimated thermal loads considered in 3.2.3 overestimated the heat generation of the electrical components, and further motivates the importance of modeling the full electro-thermal system to accurately capture coupling between the electrical and thermal domains. See the appendix for magnified views of the subplots in this figure.

Table 3.3: Nominal HETESS sizing parameters.

| Sizing Parameters	
Series (battery)	85
Parallel (battery)	8
Series (UC)	275
Parallel (UC)	15
Mass [kg] (TES1)	5
Melt Temp. [°C] (TES1)	42
Mass [kg] (TES2)	8.5
Melt Temp. [°C] (TES2)	46
Mass [kg] (TES3)	5
Melt Temp. [°C] (TES3)	42
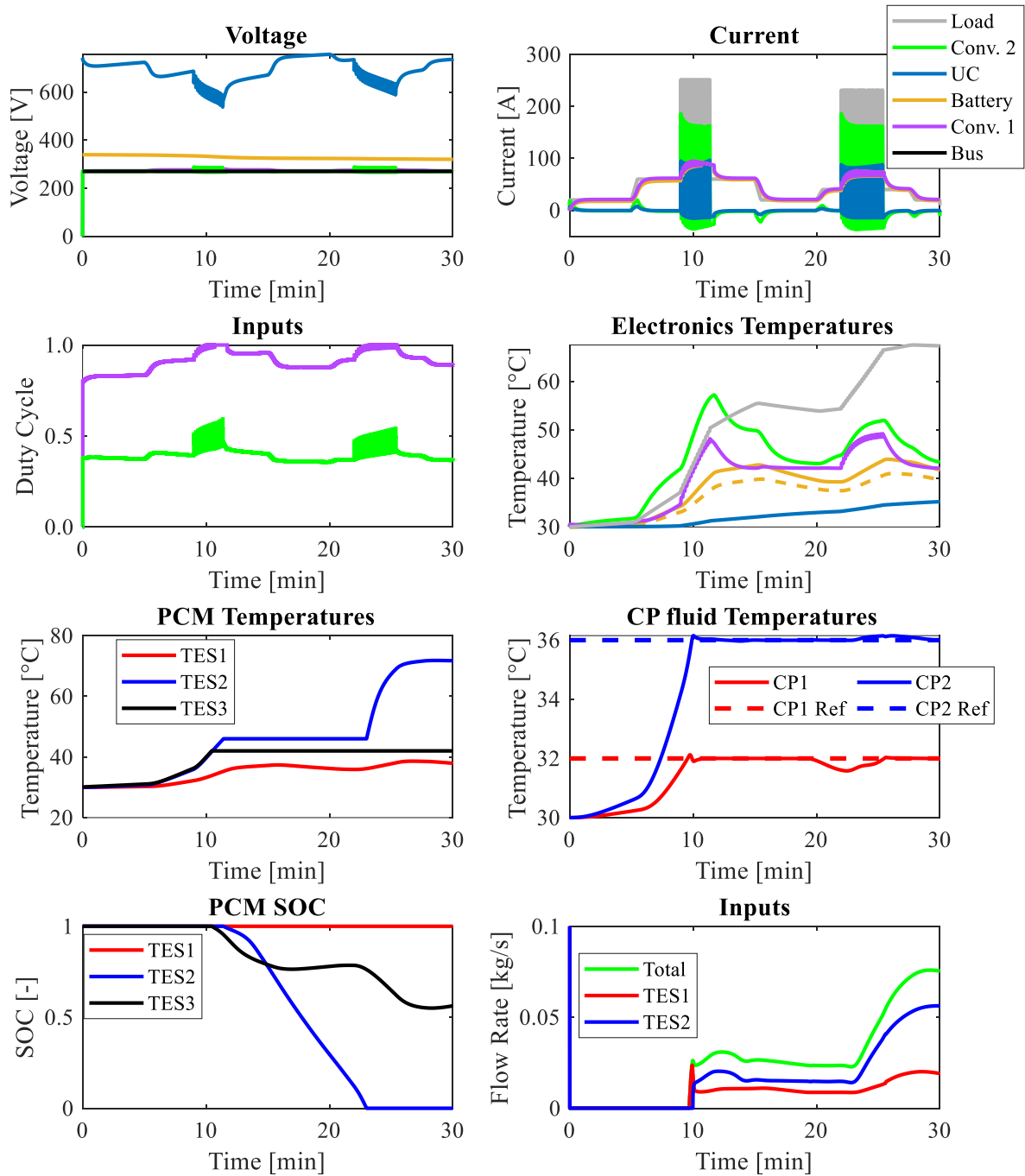
Figure 3.8: Closed-loop HETESS simulation results.

The performance of the HESS controller is demonstrated in Figure 3.9 by comparing the simulated and reference values of the bus voltage and battery power. This figure demonstrates that the bus voltage is tracked sufficiently well in the electro-thermal system. The battery power is also

tracked sufficiently, with some deviations occurring during the high ramp rate disturbances. Noting the trajectory of the corresponding control input, it is clear that these deviations occur due to the control signal reaching the upper limit of its admissible values. By increasing the number of battery cells in parallel, the power capabilities of the battery pack can be increased to avoid deviations such as these. While this motivates the need to optimize the sizing of the battery pack, we note that this deviation from the reference does not interfere with the overall goal of limiting the power demands of the battery.
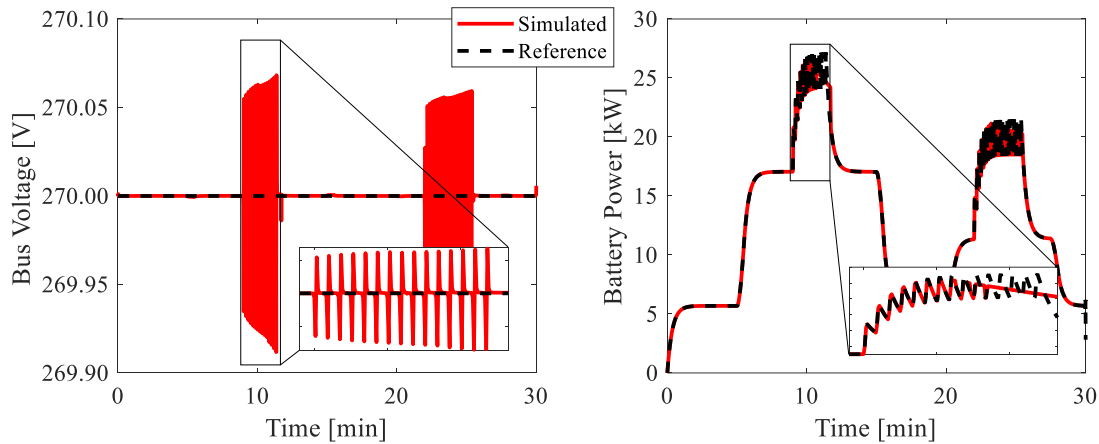
Figure 3.9: HESS controller performance in HETES system.

The performance of the TESS controller in the electro-thermal system is demonstrated by the bottom right plots in Figure 3.8. These plots show that the cold plate temperatures exceed their references only by fractions of a degree. Beginning 23 minutes into the simulation, PCM 2 fully melts, then continues to heat sensibly, which contributes to the fluid temperature in cold plate 2 exceeding its reference slightly during this time period. At this time, a larger portion of mass flow rate is directed into this flow section to cool the cold plate temperature.

These closed-loop simulation results further demonstrate the merits of the graph-based modeling framework. The domain-agnostic formulation enables the setup and simulation of a

model consisting of multi-domain signals, including coupling terms between these signals. The computation time for this simulation was 33 seconds, demonstrating a simulation speed around 60 times faster than real time. This level of computational efficiency is valuable for subsequent design optimization trials.

The respective control strategies for the HESS and TESS exhibit some relevant similarities but are structurally quite different. A notable similarity between the two control strategies is that both controllers use proportional-integral control to achieve their objectives. The computational efficiency of these heuristic control strategies is key to achieving the quick simulation speed. A notable difference is that the control signals of the HESS are decoupled, while the mass flow rates of the TESS are inherently coupled. Additionally, recalling the prior discussion of symmetrical "slow" and "fast" components in both subsystems, the selected control strategy ensures that the loads seen by the "slow" components (battery and heat exchanger) are smoothed versions of the high ramp rate load profiles for each subsystem. The HESS controller directly ensures that the battery provides the average electrical load requirement, while the TES modules indirectly filter the thermal load rejected by the heat exchanger by absorbing high ramp rate loads and rejecting heat to the cold plates at a nearly constant rate.

CHAPTER 4.   DESIGN OPTIMIZATION

In this work, a multi-objective optimization study is performed to simultaneously optimize sizing and performance of the hybrid electro-thermal energy storage system. HESS sizing is determined by the number of battery cells in series and parallel and the number of ultracapacitor cells in series and parallel. TESS sizing is determined by the mass and melting temperature of each of the PCMs in the TES modules. The performance of both of these subsystems is dependent on these sizing variables as well as the controllers and their corresponding gains. Hence in this work, we seek to optimize the controller gains and sizing variables simultaneously.

This chapter begins with an introduction to design optimization for graph-based models, which is based on a graph-based design optimization framework developed in [23]. As mentioned in Chapter 2, a major benefit of the graph-based techniques used herein is the ability to simultaneously consider energy transfers in disparate domains. In this section, we leverage this ability to examine the effects of the inclusion of electro-thermal coupling in the HETESS model. To do so, we optimize the HESS and TESS subsystems separately, then optimize the combined electro-thermal system.

4.1   Graph-Based Design Optimization Framework

The graph-based design optimization framework introduced in [23] is used as the basis for this work and consists of four steps, which are described sequentially in this section. These steps are: (i) augmenting the graph-based model with design matrices and operators, (ii) defining the design objectives, (iii) defining the design constraints, and (iv) formulating and solving the optimization problem. We first note that the framework introduced in [23] applies to the optimization of both continuous and discrete variables. By nature, some of the variables considered in this study must take on integer values; however, since they are allowed to vary over a wide

range of values, these variables are treated as continuously variable in this work. Hence we specialize the framework for the case of purely continuous design variables, and refer the interested reader to [23] for a discussion of the treatment of discrete variables in the framework.

4.1.1 Augment the Graph-Based Model

The first step in the framework is to augment the graph-based model to include the impact of the design variables on the graph-based model. A nominal graph-based model in the form of (2.7) can be augmented by introducing design matrices and operators that modify the nominal values of graph elements (vertices, edges, and source edges). The following is a discussion of these modifiers, starting with the design matrices.

Design matrices scale the nominal parameter values of graph elements according to the values of the design variables. A graph-based model which has been augmented with design matrices takes the form of

$$\Psi_c C \dot{x} = -\bar{M} \Psi P + D \Psi^s P^s, \tag{4.1}$$

where Ψ_c, Ψ, and Ψ^s are diagonal design matrices of appropriate dimensions. In this equation, Ψ_c defines scaling relationships between design variables and vertex capacitances, Ψ defines scaling relationships for power flows, and Ψ^s defines scaling relationships for source power flows. The matrix Ψ_c is a diagonal matrix defined as follows

$$\Psi_c = \begin{bmatrix} \psi_{c,1}(\theta) & \cdots & 0 \\ \vdots & \ddots & \vdots \\ 0 & \cdots & \psi_{c,N_v}(\theta) \end{bmatrix} \tag{4.2}$$

where θ represents the set of continuous design variables and the function $\psi_{c,i}$ is defined in accordance with the underlying physics of the system to quantify the scaling relationship between

the design variables and the capacitance of the ith vertex. The remaining design matrices are defined analogously as follows

$$\Psi = \begin{bmatrix} \psi_1(\theta) & \cdots & 0 \\ \vdots & \ddots & \vdots \\ 0 & \cdots & \psi_{N_e}(\theta) \end{bmatrix}, \quad (4.3)$$

$$\Psi^s = \begin{bmatrix} \psi_1^s(\theta) & \cdots & 0 \\ \vdots & \ddots & \vdots \\ 0 & \cdots & \psi_{N_s}^s(\theta) \end{bmatrix}, \quad (4.4)$$

where $\psi_i(\theta)$ defines the scaling relationship between the design variables and the ith power flow, and $\psi_i^s(\theta)$ defines the scaling relationship between the design variables and the ith source power flow.

As is the case in the present study, some situations arise in which the initial conditions of the model vary as a function of the design variables. In such cases, a fourth design matrix Ψ_0 can be introduced similarly to Ψ_c, Ψ, and Ψ^s such that

$$x_0 = \Psi_0 \bar{x}_0, \quad (4.5)$$

$$\Psi_0 = \begin{bmatrix} \psi_{0,1}(\theta) & \cdots & 0 \\ \vdots & \ddots & \vdots \\ 0 & \cdots & \psi_{0,N_v}(\theta) \end{bmatrix} \quad (4.6)$$

where $\bar{x}_0$ are the nominal initial conditions of the model, x_0 are the modified initial conditions, and $\psi_{0,i}$ defines the scaling relationship between the design variables and the initial condition of the ith state [75]. Additional design matrices can be defined to scale the nominal values of other elements of the closed-loop model formulation that are not explicitly included in (2.7), such as controller references and operating constraints. These design matrices can accomplish any

continuous linear or nonlinear scaling of the nominal values of model elements. In the general case, these additional design matrices will be denoted as H and defined in the same way as (4.2), (4.3), (4.4), and (4.6), with their individual entries denoted as $\eta(\theta)$.

While the design matrices are useful for capturing scaling relationships between the design variables and model elements, there are some rare instances in which elements of the graph model cannot be modified appropriately by scaling. In particular, consider the nonlinear functions g_j in (2.3). These are functions not only of the head and tail states and inputs, but also of the parameters of the model which may be varied in the design study. These functions may be nonlinear in the design parameters in a way that cannot be captured by a simple scaling relationship.

In this work, we address this by introducing the concept of a design operator, which modifies the form of a nonlinear function to accurately capture the effects of the changing design variables. The effect of design operators is as follows

$$g(x_h, x_t, u) = \zeta(x_h, x_t, u, \theta) \tag{4.7}$$

where $g(\cdot)$ is the new nonlinear function of the head state x_h, tail state x_t, and input u. The design operator $\zeta(\cdot, \theta)$ essentially generates a new nonlinear function $g(\cdot)$ for each set of values of the design variables θ. To make these concepts of design matrices and design operators more concrete, detailed examples of each will be provided in subsequent sections of this chapter.

4.1.2 Define the Objective Function

The second step of the framework is to define the objective function of the optimization problem. For this work, we will formulate the optimization problem in the sense of minimization of an objective function. It is straightforward to convert this formulation to one of maximization of an objective function. Following the guidelines in [23], the design engineer can define this objective function to relate the trajectories of the dynamic system to relevant metrics, such as

sizing, reliability, and performance. Some common objective functions that are of use in this work are state tracking, power flow tracking, state constraint violation, and power flow constraint violation. These take the form of transfer rate-based objective functions [23], and can be represented generically as

$$J = \sum_{j=1}^{N} \left(w_j \int_{t_0}^{t_f} z_j(t,\theta)dt \right),$$ (4.8)

where J is the value of the objective function, $z_j(t,\theta)$ is the instantaneous value of the relevant quantity to be minimized, N is the total number of elements of z at any time instance, and w_j is a weighting term quantifying the importance of the jth element of z relative to the other elements. The quantity to be minimized, $z_j(t,\theta)$, varies depending on the particular objective. For example, if the objective is to minimize state tracking error then $z_j(t,\theta)$ can be defined as $\left\| x_j(t,\theta) - x_{ref,j}(t,\theta) \right\|_2^2$, where $x_j(t,\theta)$ is the instantaneous value of the jth state and $x_{ref,j}(t,\theta)$ is the instantaneous value of the reference for the jth state. In this case, J is a weighted sum of N integrated state tracking error terms.

Objective functions are not limited to the form of (4.8). In some cases, the objectives may exhibit no dependence on the trajectories of the system. This is true, for example, when the design variables are sizing variables and the objective is to minimize size of the system, in which case the objective $J = J(\theta)$ may be a function of only the design variables θ. Additionally, individual objectives can be combined to form an aggregated objective function in order to solve an optimization problem with multiple objectives. This can be accomplished using the weighted sum method [76], for example, by defining the total objective function

$$J_{total} = w_1 J_1 + \ldots + w_N J_N$$ (4.9)

as a weighted sum of the individual objective functions $J_1,\ldots,J_N$ with weights $w_1,\ldots,w_N$, distinct from the weighting terms in (4.8).

4.1.3 Define the Design Constraints

In the third step of the framework, constraints are defined for the admissible values of the design variables. These constraints can be defined by the design engineer to enforce any problem-specific limitations to which the design variables are subjected, or to conservatively limit the design space for the sake of feasibility or computation time. Design constraints are defined as

$$\underline{\theta} \leq \theta \leq \overline{\theta} \, , \tag{4.10}$$

$$g(\theta) \leq 0 , \tag{4.11}$$

where $\underline{\theta}$ and $\overline{\theta}$ are the minimum and maximum admissible values of the design variables respectively, and $g(\theta)$ defines any nonlinear constraints [23].

4.1.4 Formulate and Solve the Optimization Problem

The final step in the framework is to formulate and solve the optimization problem. The optimization problem can be set up, using results from the preceding framework steps, as

$$\min_{\theta} J_{total}(\theta) \tag{4.12}$$

subject to the constraints (4.10) and (4.11), in addition to the constraints on system trajectories and model elements introduced in 4.1.1.

The process of solving (4.12) is not straightforward due to the dependence of the objective function on dynamic simulations, which may be nonlinear, complex functions of the design variables. One solution strategy utilizes the shooting method [77]. For the graph-based methods considered herein, the shooting method consists of generating an augmented graph-based model for the current set of design variable values, then simulating the model under these conditions, and

finally using the simulation results to calculate the objective function. Direct transcription [78] is another potential solution method for optimization problems with optimal control formulations.

4.2   HESS Design and Control Optimization

To demonstrate the application of this optimization framework, the sizing and control parameters of the HES, TES, and HETES systems will each be optimized, starting with optimization of the HESS sizing and control parameters. HESS sizing is determined by the number of battery cells in series and parallel and the number of ultracapacitor cells in series and parallel. As is the norm for battery system sizing, the number of battery cells in series is chosen such that the voltage of the battery pack is near the desired bus voltage. Thus the sizing design variables in this study are

$$\theta^E = \{N_{p,batt}, N_{s,UC}, N_{p,UC}\},\tag{4.13}$$

where $N_{p,batt}$ is the number of parallel battery cells, and $N_{s,UC}, N_{p,UC}$ are the numbers of series and parallel ultracapacitor cells respectively. Note the superscript E is used to indicate that θ^E corresponds to sizing variables in the electrical subsystem. By nature, these variables must take on integer values. However, since they are allowed to vary over a wide range of values, these variables are treated as continuously variable in this study. HESS performance is dependent upon these sizing variables as well as the controllers and their corresponding gains, which are each modified with a set of continuous scaling variables, denoted as ϕ^E. The goal of this optimization will be to minimize sizing of the HESS while maximizing its performance, in terms of reference tracking and safe operation of the battery. In this section, we proceed through the steps of the framework introduced in the preceding section for this particular optimization problem. The methods, results, and analysis presented here were introduced in [75] and are repeated here for completeness.

<u>4.2.1 Graph-Based HESS Model Augmentation</u>

In the HESS, sizing variables θ^E impact vertex capacitances, edge values, and initial conditions, so design matrices will be created for each of these elements. The nonlinear functions g_j in (2.3) are independent of the HESS design variables so design operators are not necessary for this system. We will now build up the design matrices corresponding to each of the graph elements, starting with the vertex capacitances. In 2.3.1, it was shown that several of the battery vertex capacitances are dependent on the design variables. In particular, capacitances Q, C_1, C_2, C_c, and C_s, corresponding to vertices q_1, V_2, V_3, T_4, and T_5 respectively in the full HESS model, are dependent on the number of parallel battery cells according to the following relation

$$C' = N_{p,batt} C. \tag{4.14}$$

Thus, in the design matrix Ψ_c, the corresponding functions $\psi_{c,1}(\theta^E)$, $\psi_{c,2}(\theta^E)$, $\psi_{c,3}(\theta^E)$, $\psi_{c,4}(\theta^E)$, and $\psi_{c,5}(\theta^E)$ are defined such that

$$\psi_{c,i}(\theta^E) = \theta_1^E = N_{p,batt}, \quad i = 1,\ldots,5. \tag{4.15}$$

With the ultracapacitor pack modeled as an ideal capacitor, its capacitance scales with the design variables as $C' = N_{p,UC} C / N_{s,UC}$. Hence the function corresponding to the ultracapacitor voltage vertex V_{12} is given by

$$\psi_{c,12}(\theta^E) = \theta_3^E / \theta_2^E = N_{p,UC} / N_{s,UC}. \tag{4.16}$$

In the HESS, these are the only capacitances that are dependent on the design variables, so the remaining functions $\psi_{c,i}(\theta^E)$ are simply set to unity.

The Ψ design matrix, corresponding to scaling of power flows, will now be built. In the battery pack, edges e_4, e_5, and e_6 represent resistive losses, and e_7 represents a thermal transfer

with an associated thermal resistance. As discussed in 2.3.1, these resistance parameters are inversely proportional to the number of parallel battery cells. The power flow corresponding to e_4, whose tail vertex is the current vertex I_{10}, is given by $I_{10}^2 R_s$, while the power flows corresponding to e_5, e_6 are given by V_2^2 / R_1 and V_3^2 / R_2 respectively. The power flow of e_7 is defined as $(T_4 - T_5) / R_c$. It follows that the scaling of the power flow corresponding to e_4 is inversely proportional to the number of parallel battery cells, while the scaling relationships of the power flows corresponding to e_5, e_6, and e_7 are directly proportional to the number of parallel battery cells. The corresponding entries of the design matrix Ψ are thus given by

$$\psi_4(\theta^E) = 1 / \theta_1^E = 1 / N_{p,batt}, \tag{4.17}$$

$$\psi_i(\theta^E) = \theta_1^E = N_{p,batt}, \quad i = 5, 6, 7. \tag{4.18}$$

For the ultracapacitor, the resistive loss e_{22} with tail vertex I_{13} is proportional to the corresponding resistance, which scales with the design variables as $R' = N_{s,UC} R / N_{p,UC}$. The corresponding entry of the design matrix Ψ is given by

$$\psi_{22}(\theta^E) = \theta_2^E / \theta_3^E = N_{s,UC} / N_{p,UC}. \tag{4.19}$$

The power flows given by (4.17)-(4.19) are the only ones dependent on the design variables, so the remaining entries $\psi_i(\theta^E)$ are set to unity. There are no source flows in the HESS, so the Ψ^s design matrix is the identity matrix.

The design matrix pertaining to initial conditions (4.6) is now specified. The ultracapacitor voltage V_{12} is the only vertex whose initial condition is dependent on the design variables. To maximize its capability as an energy source, the ultracapacitor voltage is initialized near its

maximum voltage. The terminal voltage of the pack scales proportionally with the number of series ultracapacitor cells, so the entry of Ψ_0 corresponding to this voltage vertex is given by

$$\psi_{0,12}(\theta^E) = \theta_2^E = N_{s,UC},\qquad(4.20)$$

and as this is the only design-variable-dependent initial condition, all other elements $\psi_{0,i}(\theta^E)$ of Ψ_0 are set to unity.

Lastly, we define design matrices for other elements of the model that are dependent on design variables but not explicitly shown in the graph-based representation (4.1). One such element, arising from the objective of safe battery operation, is a constraint on the magnitude of power drawn from each cell of the battery pack. To prevent cell degradation due to high discharge rates, a power constraint P'_{max} is defined on the battery power flow (edge e_{26}) such that

$$P'_{max} = P_{max}N_{s,batt}N_{p,batt},\qquad(4.21)$$

where P_{max} is the maximum power rating of an individual cell. A power constraint design matrix $H_1 = diag(\eta_i(\theta^E))$ is created to reflect this dependence on the design variables. Since $N_{s,batt}$ is held fixed in this study, the entry in H_1 corresponding to edge e_{26} is given by $\eta_{26}(\theta^E) = \theta_1^E = N_{p,batt}$. This is the only maximum power constraint that is dependent on the design variables, so the remaining entries of this design matrix are unity. A second design matrix H_2 for the minimum battery power constraint is defined analogously.

In addition to the sizing variables θ^E, the controller gains in this study will be optimized to maximize performance. To do so, we introduce gain scaling variables

$$\phi^E = \{\alpha_1^E\ \ \beta_1^E\ \ \alpha_2^E\ \ \beta_2^E\}\qquad(4.22)$$

such that

74

$$K'^E_{p1} = \phi^E_1 K^E_{p1} = \alpha^E_1 K^E_{p1},$$
$$K'^E_{i1} = \phi^E_2 K^E_{i1} = \beta^E_1 K^E_{i1},$$
$$K'^E_{p2} = \phi^E_3 K^E_{p2} = \alpha^E_2 K^E_{p2}, \qquad (4.23)$$
$$K'^E_{i2} = \phi^E_4 K^E_{i2} = \beta^E_2 K^E_{i2},$$

where $K^E_{p1}, K^E_{i1}, K^E_{p2}$, and K^E_{i2} are the nominal values of the controller gains given in 3.1.3.

The translation of (4.23) to a design matrix form is straightforward.

4.2.2 HESS Objective Function Definition

The optimization objectives for the HESS are to minimize sizing of the energy storage elements and to maximize the system's performance. The sizing objective is taken as the mass of the energy storage elements, given by

$$J^E_{size} = m_{batt} N_{p,batt} N_{s,batt} + m_{UC} N_{p,UC} N_{s,UC}, \qquad (4.24)$$

where $m_{batt} = 0.132$kg and $m_{UC} = 0.023$kg are the masses of individual battery and ultracapacitor cells respectively.

The performance objective takes into account the performance of the HESS controller as well as safe operation of the battery pack in terms of its adherence to the maximum power constraint described in 4.2.1. Note that, though the heuristic PI control strategy is not capable of explicitly considering constraints on the system, constraining the maximum battery power flow is crucial to ensure safe operation, so this constraint (4.21) is indirectly enforced with an added term in the optimization objective function. HESS performance is maximized by minimizing deviations from ideal performance. These deviations are quantified by bus voltage tracking error, battery power tracking error, and violations of the maximum battery power constraint. At a time instant t, deviations in performance are given by

$$E_{perf}(t) = w_1 \left| V_{bus}(t) - V_{ref}(t) \right|^2 + w_2 \left| P_{DCDC1}(t) - P_{filt}(t) \right|^2 + w_3 \left| s_{P_{batt}}(t) \right|^2 \qquad (4.25)$$

where w_1, w_2, and w_3 are weightings on each of the terms and $s_{P_{batt}}$ is a nonnegative slack variable corresponding to violation of the battery maximum power constraint. These weightings are tuned such that all terms in (4.25) are nearly equal in magnitude. The slack variable is given by

$$P_{batt} \leq P'_{max} + s_{P_{batt}} .$$
(4.26)

The total performance objective for a given simulation is obtained by integrating the instantaneous performance deviations throughout the simulation as follows

$$J_{perf}^{E} = \int_{0}^{t_{final}} E_{perf}(t)dt ,$$
(4.27)

where t_{final} is the final time of the simulation.

The overall optimization objective of the HESS combines the sizing and performance objectives. Minimization of size and maximization of performance, however, are competing objectives; reducing the size of the HESS inevitably leads to poor reference tracking and increases the risk of the battery pack violating its maximum power constraint. Thus in this work the design and control optimization is formulated as a multi-objective problem, which is analyzed using an aggregate objective function. This objective function is defined using the weighted sum method as

$$J_{total}^{E} = w_{perf} J_{perf}^{E} + w_{size} J_{size}^{E} ,$$
(4.28)

where w_{perf} and w_{size} are weighting terms which quantify the relative importance of the performance and sizing objectives respectively.

4.2.3 Definition of HESS Design Constraints

Upper and lower bounds are defined for the sizing variables θ^E and control variables ϕ^E. In this study, the lower bound on $N_{s,UC}$ corresponds to the minimum number of ultracapacitor cells required to reach the bus voltage reference. The lower bounds on $N_{p,batt}$ and $N_{p,UC}$

correspond to the minimum number of cells of each component needed to fulfill the load requirement without becoming fully depleted. The upper bounds on the sizing variables can then be chosen such that the total size of the HESS remains below some desired value. In this study the upper bounds were selected liberally to allow the optimizer more freedom in selecting values for the design variables.

Determination of bounds for the controller gain scaling variables ϕ^E is ultimately up to the designer. These bounds can be chosen, for example, to ensure the closed loop system remains within admissible ranges for response time or amount of overshoot. In this work the nominal controller gains were tuned to achieve good performance (bus voltage deviations less than 1V), and the gain scaling variable bounds were chosen such that the controller gains could be increased or decreased by up to a factor of 10 to improve performance and maintain stability.

4.2.4 Formulation and Solution of the HESS Optimization Problem

The dependence of the objective function on closed-loop simulation results motivates the use of the shooting method to solve this optimization problem. As described previously, the shooting method consists of performing a dynamic simulation of the augmented graph-based model in closed loop for each set of design variables and then using these simulation results to calculate the objective function. Particularly, in this study the optimization problem is formulated such that the augmented graph-based model is simulated in MATLAB using ode23t under the load profile and control strategy shown in Figure 3.4. The closed-loop simulation results are used to calculate the objective function (4.28) for a given set of weightings w_{perf} and w_{size}. Stability of the optimization problem is ensured by setting the objective function to a large value for designs that result in simulation failure or unacceptable performance. Gradient-based algorithms are ill-suited to solve the nonconvex objective function (4.28), so a genetic algorithm (GA) is used to reduce

77

the likelihood of convergence to a local minimum. For the results presented in this section, the GA in the MATLAB optimization toolbox was used with a population size of 50 and function tolerance of 10^{-5}. The computational efficiency of the graph-based modeling framework allowed for simulations to run 60 times faster than real time, keeping the solution time relatively low for the optimization study.

Figure 4.1 and Figure 4.2 illustrate the improvements in HESS performance and sizing obtained using the design and control optimization framework for the optimization problem corresponding to $w_{perf} = 0.57$ and $w_{size} = 0.43$ [75]. These figures compare the best design from the initial generation evaluated by the GA to the optimized design from the final generation. The results in Figure 4.1 compare the final (optimal) and initial designs in terms of dynamic responses of the bus voltage and battery power as well as values of the design variables. The final design is shown to outperform the initial design in terms of voltage reference tracking, while exhibiting significant reductions in the number of ultracapacitor cells and achieving similar performance in battery power reference tracking. The sizing improvement between the initial and final designs is illustrated in Figure 4.2. By reducing the number of ultracapacitor cells, the mass and volume of the final design are significantly reduced compared to the initial design. See the appendix for magnified views of the top two subplots of Figure 4.1.

To examine the relationships between the sizing and performance objectives, a series of individual optimization problems are obtained by varying the relative magnitudes of weightings w_{perf} and w_{size} on the performance and sizing objectives respectively. To cover a wide range of weighting combinations, these weightings are varied by varying w_{perf} between 0 and 1 and setting $w_{size} = 1 - w_{perf}$. Solving each of these optimization problems yields a set of Pareto optimal designs. The optimal designs obtained in this study are shown in Figure 4.3 with the Pareto frontier shown

78

in gray. The performance objective is normalized to its maximum value on the Pareto frontier. The color of points in Figure 4.3 corresponds to the relative magnitudes of w_{perf} and w_{size}, where dark blue points correspond to high w_{size} and light blue points correspond to high w_{perf}. The starred point in Figure 4.3 corresponds to the results shown previously in Figure 4.1 and Figure 4.2. From this Pareto frontier, it is observed that sizing reductions can be made with minimal degradation in performance in the range from 550kg to 250kg, but further reducing the size below 250kg can lead to undesirable performance.
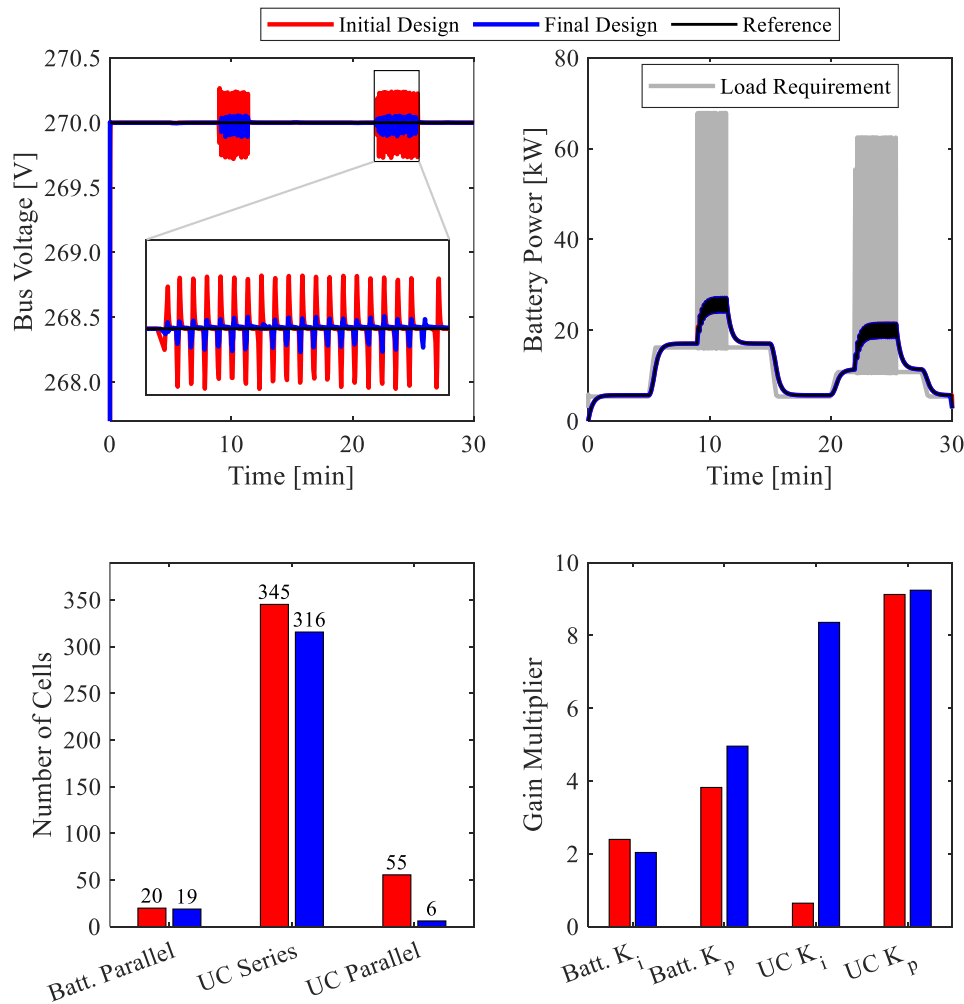
Figure 4.1: Comparison of initial and final HESS designs.
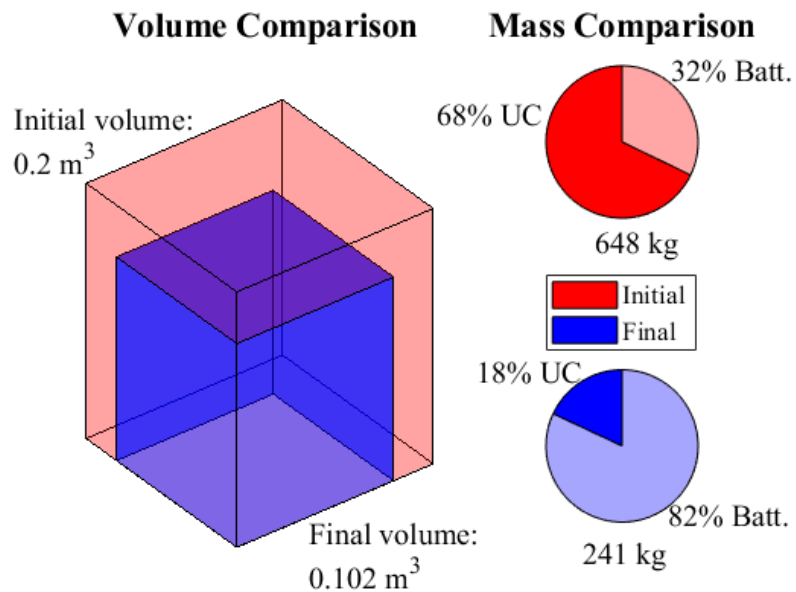
Figure 4.2: Comparison of initial and final HESS sizing metrics.
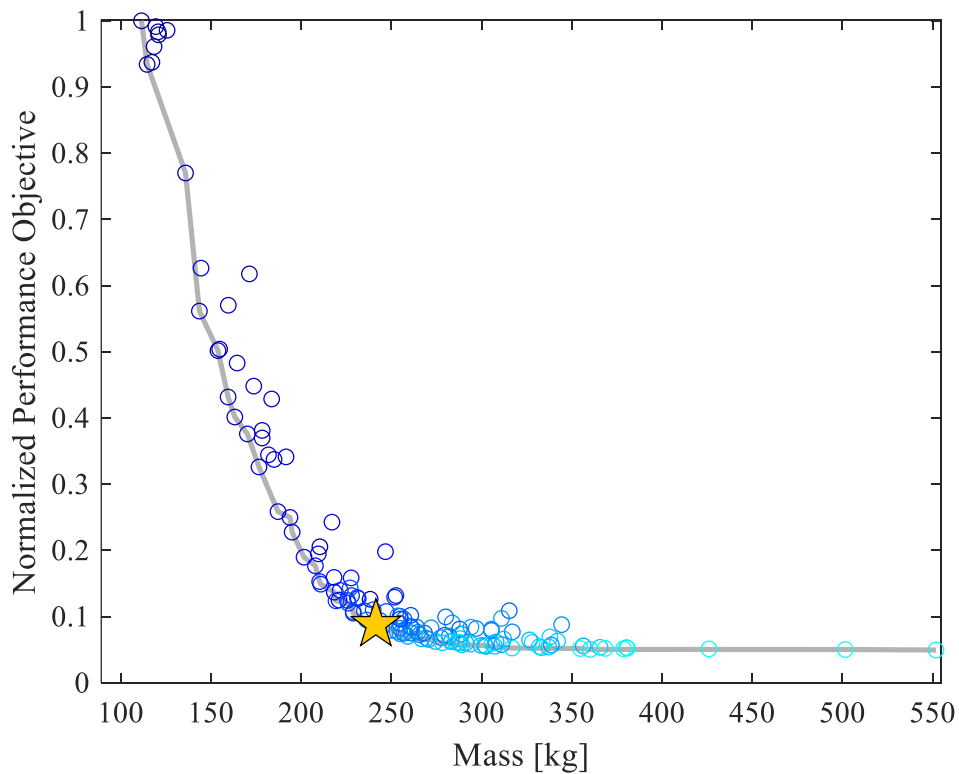
Figure 4.3: Sizing and performance tradeoff for HESS.

In the results shown above, the sizing and control parameters are simultaneously optimized to improve characteristics of the overall system. We now examine the effectiveness of including the control parameters in the optimization by comparing the results shown above to a benchmark study performing sizing optimization only. The benchmark study varied only the sizing variables $\theta^E = \{N_{p,batt}, N_{s,UC}, N_{p,UC}\}$ while holding the control gains constant at the nominal values given in Table 2.1. A set of Pareto-optimal designs was obtained for the sizing-only benchmark study by varying the weights on the sizing and performance objectives, as was done for the sizing and control optimization study. A comparison in Figure 4.4 of these results with the results obtained by the sizing and control optimization study shows a dramatic improvement in performance when the controller parameters are adjusted by the optimizer. This dramatic improvement underscores the importance of incorporating control strategies and control parameters in the design process.
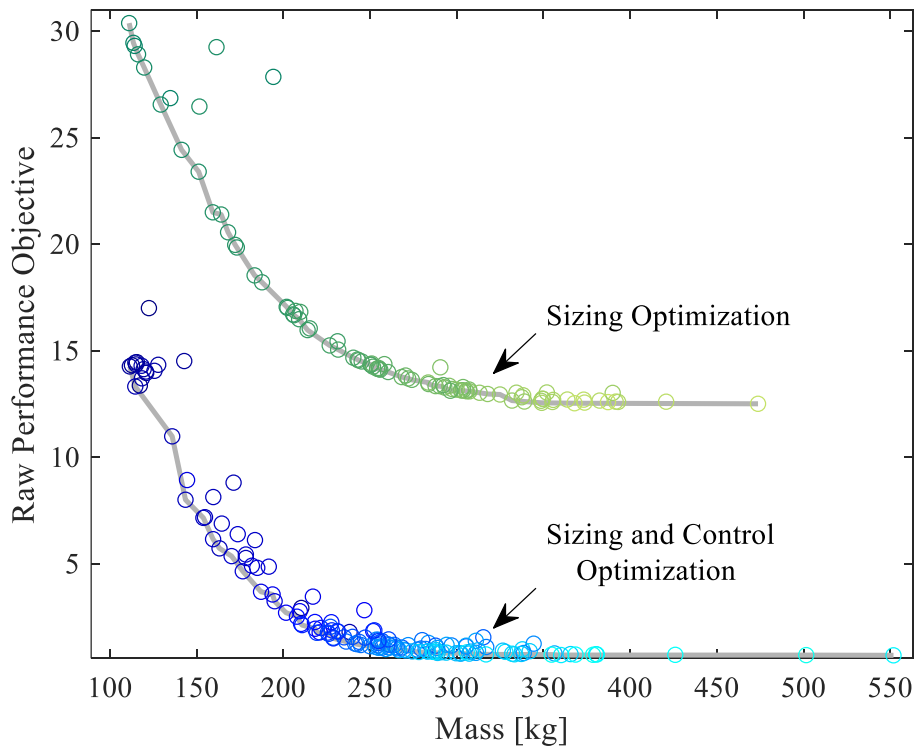
Figure 4.4: Performance improvement by including control parameters in HESS optimization.

81

4.3 TESS Design and Control Optimization

In this section, the design and control parameters of the TESS are optimized. Assuming the coolant loop components are fixed, the sizing parameters to be optimized are the parameters of the TES modules. In this work, we focus on paraffin waxes for PCM thermal energy storage due to their high latent heat capacity and wide selection of melt temperature [79]. While the mass of these paraffin wax TES modules can be varied continuously, the melt temperature variation is restricted to the discrete set of melting temperatures of commercially available waxes. However, the distribution of melt temperatures of commercially available waxes is nearly continuous in the range between 30°C and 80°C [80], [81]. For this reason, PCM melt temperatures are treated as continuously variable in this study, similarly to the treatment of battery and ultracapacitor cells in Section 4.2. Thus the continuous sizing variables of the TESS are

$$\theta^T = \{m_1, T_{m,1}, m_2, T_{m,2}\} \tag{4.29}$$

where m_i is the mass of the ith TES module and $T_{m,i}$ is its melt temperature. Note the superscript T is used to indicate that θ^T corresponds to thermal sizing variables. As with the HESS, the performance of the TESS is dependent on its controllers, so the control gains are also treated as design variables in this study. These will be modified with a set of scaling variables which will be denoted as ϕ^T. Paralleling the objectives of the HESS optimization, the TESS optimization objectives will be to minimize the mass of the TES modules while maximizing performance of the TES system. Minimization of the performance objective aims to maintain safe operation by adhering to state constraints and to minimize pump energy consumption. In this section, we proceed through the steps of the framework introduced in section 4.1 for this optimization problem.

4.3.1 Graph-Based TESS Model Augmentation

To augment the graph-based TESS model, we first note that the parameters of all coolant loop components are being held constant, so the TES module models are the only portions of the graph model affected by modifying the sizing variables θ^T. Referring to section 2.3.5, it can be noted that the PCM mass and melt temperature impact the TES module graph model only through the nonlinear edge map given by (2.40). As a result, the design matrices Ψ_c, Ψ, Ψ^s, and Ψ_0 considered in (4.1)-(4.6) are all identity matrices of the appropriate dimensions. However, design operators must be defined for the nonlinear edge maps of the TES module graph model. These nonlinear edge maps correspond to edges e_5 and e_6 in the TESS graph (see Figure 2.17). For a given set of design variables θ^T, these edge maps are given by the following piecewise linear functions. For clarity, the functions below are given in terms of the head and tail states corresponding to each edge as defined in Figure 2.17.

$$
g_5(E_8,T_7) = \zeta_5(E_8,T_7,\theta^T) = \begin{cases} \dfrac{1}{R_{u,1}}\left(T_{0,1} + \dfrac{1}{C_1}E_8 - T_7\right) & \text{if } E_8 \le E_{c,1}, \\[2ex] \dfrac{1}{R_{u,1}}\left(T_{m,1} - T_7\right) & \text{if } E_{c,1} < E_8 < E_{c,1} + L_1, \\[2ex] \dfrac{1}{R_{u,1}}\left(T_{m,1} + \dfrac{1}{C_1}(E_8 - E_{c1} - L_1) - T_7\right) & \text{if } E_8 \ge E_{c,1} + L_1, \end{cases} \quad (4.30)
$$

$$
g_6(E_{10},T_9) = \zeta_6(E_{10},T_9,\theta^T) = \begin{cases} \dfrac{1}{R_{u,2}}\left(T_{0,2} + \dfrac{1}{C_2}E_{10} - T_9\right) & \text{if } E_{10} \le E_{c,2}, \\[2ex] \dfrac{1}{R_{u,2}}\left(T_{m,2} - T_9\right) & \text{if } E_{c,2} < E_{10} < E_{c,2} + L_2, \\[2ex] \dfrac{1}{R_{u,2}}\left(T_{m,2} + \dfrac{1}{C_2}(E_{10} - E_{c,2} - L_2) - T_9\right) & \text{if } E_{10} \ge E_{c,2} + L_2, \end{cases}
$$

$$(4.31)$$

In these equations, subscripts 1 and 2 are used to denote properties of TES1 and TES2 respectively. For the ith TES module, $R_{u,i}$ is the thermal resistance, $T_{0,i}$ is the temperature at which the PCM energy is initialized, C_i is the sensible heat capacity, $E_{c,i}$ is the "critical energy", and L_i is the latent heat capacity. The dependence of (4.30) and (4.31) on the design variables emerges from its direct dependence on design variables $T_{m,1}$ and $T_{m,2}$ as well as from these parameters. As noted in section 2.3.5, the sensible heat capacity depends on the PCM mass as $C_i = m_i c_i$, and the latent heat capacity depends on the PCM mass as $L_i = m_i l_i$. Additionally, from Figure 2.11 it can be seen that the critical energy depends on both the mass and melt temperature as $E_{c,i} = \dfrac{T_{m,i} - T_{0,i}}{C_i}$. So, for a given set of design variables $\theta^T = \{m_1, T_{m,1}, m_2, T_{m,2}\}$, the design operators ζ_5 and ζ_6 each generate a nonlinear mapping according to (4.30) and (4.31), and these nonlinear maps are used to calculate the values of g_5 and g_6 for instantaneous values of E_8, E_{10}, T_7, and T_{10}. Since (4.30) and (4.31) are piecewise linear, they can be implemented as 2-D lookup maps of the corresponding state variables.

Next we define design matrices for other elements of the model that are dependent on design variables, but not explicitly included in the graph model formulation. Two such elements are the reference signals for the TESS controllers. Recalling Section 3.2.1, the PI controllers dictating the pump duty cycle use a temperature reference which is set to 10°C below the melt temperature of the respective PCM. The temperature references correspond to fluid temperatures of cold plates 1 and 2, which are defined as the sixth and fifth states (T_6 and T_5) respectively in Figure 2.17. A design matrix $H_1 = diag(\eta_i(\theta^T))$ is introduced to reflect the dependence of the state references on the design variables. We define a vector of nominal state references as $\bar{x}_{ref}$, denoting

the ith component as $\bar{x}_{ref,i}$. In the TESS, only the references for states T_6 and T_5 are used, so the remaining components of $\bar{x}_{ref}$ can be defined arbitrarily. Doing so, the entries of the design matrix H_1 corresponding to cold plate fluid temperatures are given by

$$\begin{aligned}
\eta_6(\theta^T) &= (\theta_2^T - 10) / \bar{x}_{ref,6} \\
\eta_5(\theta^T) &= (\theta_4^T - 10) / \bar{x}_{ref,5}
\end{aligned}$$
(4.32)

where θ_2^T and θ_4^T are the melt temperatures of PCMs 1 and 2 respectively, and $\bar{x}_{ref,i}$ is the value of the corresponding controller reference for the nominal system described in 3.2.3. The remaining entries of the design matrix H_1 will not affect the system, so they are set to unity. The vector of augmented controller references is then given by

$$x_{ref} = H_1 \bar{x}_{ref}.$$
(4.33)

The TESS controller gains, in addition to the sizing variables θ^T, will be optimized to maximize performance. To do so, we again introduce gain scaling variables

$$\phi^T = \{\alpha_1^T \quad \beta_1^T \quad \alpha_2^T \quad \beta_2^T\}$$
(4.34)

such that

$$\begin{aligned}
K'^T_{p1} &= \phi_1^T K_{p1}^T = \alpha_1^T K_{p1}^T, \\
K'^T_{i1} &= \phi_2^T K_{i1}^T = \beta_1^T K_{i1}^T, \\
K'^T_{p2} &= \phi_3^T K_{p2}^T = \alpha_2^T K_{p2}^T, \\
K'^T_{i2} &= \phi_4^T K_{i2}^T = \beta_2^T K_{i2}^T,
\end{aligned}$$
(4.35)

where $K_{p1}^T, K_{i1}^T, K_{p2}^T$, and K_{i2}^T are the nominal values of the controller gains given in 3.2.3. These scaling relationships can readily be translated to a design matrix form.

4.3.2 TESS Objective Function Definition

Similar to the objectives of the HESS optimization study, the objectives of the TESS optimization study are to minimize mass of the TES modules and maximize their performance.

Since the masses of the TES modules are design variables, the sizing objective (mass of TES modules) is simply given by

$$J_{size}^{T} = m_1 + m_2.$$

(4.36)

The performance objective takes into account the performance of the TESS controller, safe operation of the TESS in terms of adherence to constraints on state variables, and pump energy consumption. The controller performance subobjective should quantify how well the cold plate fluid temperatures track their references. However, there should be no penalty in controller performance when these temperatures remain below their reference temperatures because it is preferable for system temperatures to remain low. For this reason, the controller performance subobjective is defined to quantify deviations from ideal controller performance by measuring how much the cold plate fluid temperatures exceed their references. This effectively turns the controller performance subobjective into a measure of constraint violation for states T_6 and T_5, where the constraints for these states are the state references given by (4.33). In addition to these temperature constraints, a maximum temperature constraint of 80°C is applied to other temperatures in the system to ensure the TESS can effectively cool electronic equipment. Because it is undesirable to allow the PCM to fully melt and overheat, the TES modules are also constrained by applying SOC constraints. The states of charge of the TES modules are not states in the TES system, so SOC constraint violation must be calculated by first applying (2.41) to calculate the SOC of each TES module as a function of the PCM stored energy states, E_8 and E_{10}. The final contribution to the performance objective is pump power consumption, which is included as a performance subobjective to penalize designs which cause the pump to use excessively large amounts of power. Note that in order to improve simulation speed, a nonzero minimum mass flow rate is enforced in the hydraulic model, so each design will incur a small but nonzero amount of pump energy

86

consumption. Modeling of the pump hydraulic dynamics falls outside the scope of the thesis, but the reader is referred to [82] for a discussion on the calculation of pump energy consumption. Constraint violation and pump energy constitute deviations from ideal TESS performance, so these terms are aggregated into the following measure of instantaneous deviations from ideal performance

$$E_{perf}(t) = w_1 \| s(t) \|^2_Q + w_2 P_{pump}(t),$$ (4.37)

where $s(t)$ is a vector of slack variables corresponding to state constraint violations at time t, $P_{pump}(t)$ is the instantaneous amount of pump power consumption, Q is a positive definite diagonal matrix used to scale the relative magnitude of state constraint violations, and w_1 and w_2 are weighting terms on the constraint violation and pump power consumption subobjectives respectively. Note that (4.37) employs the notation $\| x \|^2_A = x^T A x$. The aggregate performance objective is obtained by integrating (4.37) over the course of the simulation as follows

$$J^T_{perf} = \int_0^{t_{final}} E_{perf}(t) dt ,$$ (4.38)

where t_{final} is the final time of the simulation.

The overall optimization objective of the TESS combines the competing sizing and performance objectives. This is accomplished, as with the HESS, using the weighted sum method, resulting in the following total objective function

$$J^T_{total} = w_{perf} J^T_{perf} + w_{size} J^T_{size}$$ (4.39)

where, as before, w_{perf} and w_{size} quantify the relative importance of the performance and sizing objectives respectively in the total objective function.

4.3.3 Definition of TESS Design Constraints

The next step is to define upper and lower bounds for the design variables. Bounds on the sizing design variables $\theta^T = \{m_1, T_{m,1}, m_2, T_{m,2}\}$ are chosen by considering physical constraints on the desired vehicle platform and the selected phase change materials. The lower bounds of PCM masses m_1 and m_2 are both set to 0.25kg. To limit the mass of the thermal management system, the upper bounds of these masses are both set to 50kg. As mentioned at the start of section 4.3, the melt temperatures of commercially available paraffin waxes vary within the range from 30°C to 80°C. Hence, to ensure that each TES module design could be made from commercially available products, the lower and upper bounds for the PCM melt temperatures $T_{m,1}$ and $T_{m,2}$ are set to 30°C and 80°C respectively. The upper and lower bounds for the TESS sizing design variables are thus given by

$$
\begin{aligned}
0.25\text{kg} &\leq \theta_1^T \leq 50\text{kg} \\
30°\text{C} &\leq \theta_2^T \leq 80°\text{C} \\
0.25\text{kg} &\leq \theta_3^T \leq 50\text{kg} \\
30°\text{C} &\leq \theta_4^T \leq 80°\text{C}.
\end{aligned}
\tag{4.40}
$$

The control gain scaling variables $\phi^T = \{\alpha_1^T, \beta_1^T, \alpha_2^T, \beta_2^T\}$ are bounded such that the controller gains can be scaled up or down by a factor of 10. Since the nominal gains given in 3.2.3 are tuned to achieve good performance for the nominal system, this allows the optimizer to conservatively vary the control gains to improve performance while retaining stability.

4.3.4 Formulation and Solution of the TESS Optimization Problem

The final step in the TESS optimization study is to formulate and solve the optimization problem, which is accomplished using the shooting method. The augmented TESS graph-based model is simulated in Simulink using the ode23tb solver under the thermal load shown in Figure 3.6. The resulting closed-loop simulation results are used to calculate the objective function (4.39)

for a given set of weightings w_{perf} and w_{size}. The objective function is set to infinity for designs which yield undesirable performance or cause the solver to fail. The genetic algorithm in MATLAB's optimization toolbox is used to perform the optimization with a population size of 50 and function tolerance of 5×10^{-4}. The computationally efficient graph-based model typically simulates around 90 times faster than real time, enabling the genetic algorithm to explore a large design space and arrive at an optimal solution in a reasonable amount of time.

Figure 4.5 and Figure 4.6 show the changes in the TESS sizing and performance resulting from implementing the graph-based optimization framework for the optimization problem corresponding to $w_{perf} = 0.52$ and $w_{size} = 0.48$. These figures compare the best design from the initial generation evaluated by the genetic algorithm to the optimized design from the final generation. The upper plot in Figure 4.5 shows the heat loads applied to the two TES modules, and the remaining plots in this figure show the cold plate fluid temperatures and PCM states of charge. For both the initial and final design, the cold plate fluid temperatures are observed to reach without exceeding their reference values, indicating satisfactory controller performance. The reference temperatures change significantly from the initial to the final design; the CP1 reference temperature increases from 49°C to 70°C, and the CP2 reference temperature increases from 51°C to 70°C. Additionally, the trajectories of the PCM states of charge show significant changes from initial to final design. In TES1, the PCM heats and subsequently melts very slowly in the initial design such that the PCM doesn't fully melt by the end of the simulation. In the final design, the PCM in TES1 melts and heats at a faster rate, fully melts 22 minutes into the simulation, and remains fully melted for the remainder of the simulation. In TES2, the PCM heats and melts very quickly for both the initial and final designs, with the final design showing the faster rate of heating and melting. Figure 4.6 shows the values of the sizing and performance objectives, as well as the

design variables, for the initial and final designs. From this figure, it can be seen that the sizing objective is significantly reduced between the initial and final designs, which is accomplished by a dramatic reduction in TES1 mass and a slight reduction in TES2 mass. These mass reductions explain the high rate of PCM melting, heating, and cooling for the final design. Comparing the initial and final performance subobjectives in Figure 4.6, it can be seen that the final design exhibits more constraint violation than the initial. This increase is attributed to the SOC of TES1 falling below its lower limit of 0.1, as shown in Figure 4.5. Finally, we note that the PCM melt temperatures converge to their upper limit of 80°C. Because of this, the cold plate fluid reference temperatures are higher, so the pump does not have to expend much energy cooling the cold plates. Additionally, if melt temperatures were lower, more constraint violation would be seen in the final design, as the PCM would begin melting sooner. See the appendix for magnified views of each of the subplots of Figure 4.5.

A multi-objective optimization study is performed by systematically varying the sizing and performance weightings, w_{size} and w_{perf}, such that $0 \leq w_{perf} \leq 1$ and $w_{size} = 1 - w_{perf}$. Solving each of this series of optimization problems yields a set of Pareto-optimal designs. The optimal designs obtained in this study are shown in Figure 4.7 with the Pareto frontier shown in gray and the starred point corresponding to the results shown in Figure 4.5 and Figure 4.6. The performance objective is normalized to its maximum value on the Pareto frontier. Following the convention of Figure 4.3, the color of points in Figure 4.7 corresponds to the relative magnitudes of w_{perf} and w_{size}, where dark blue points correspond to high w_{size} and light blue points correspond to high w_{perf}. From this figure, it can be seen that the total PCM mass can be reduced to around 5kg, but further decreases in PCM mass lead to large deviations from ideal performance. On the other hand, TESS performance can be improved considerably by increasing PCM mass, but increasing the PCM mass

beyond 20kg yields little improvement in performance. The ability to generate tradeoff curves such as Figure 4.3 and Figure 4.7 highlights the utility of the graph-based framework as a tool to perform multi-objective optimization for a variety of engineering systems. In the following section, we will show the aptitude of the framework to handle multidisciplinary optimization problems by applying the framework to optimize the combined electro-thermal system described in 2.4.3.
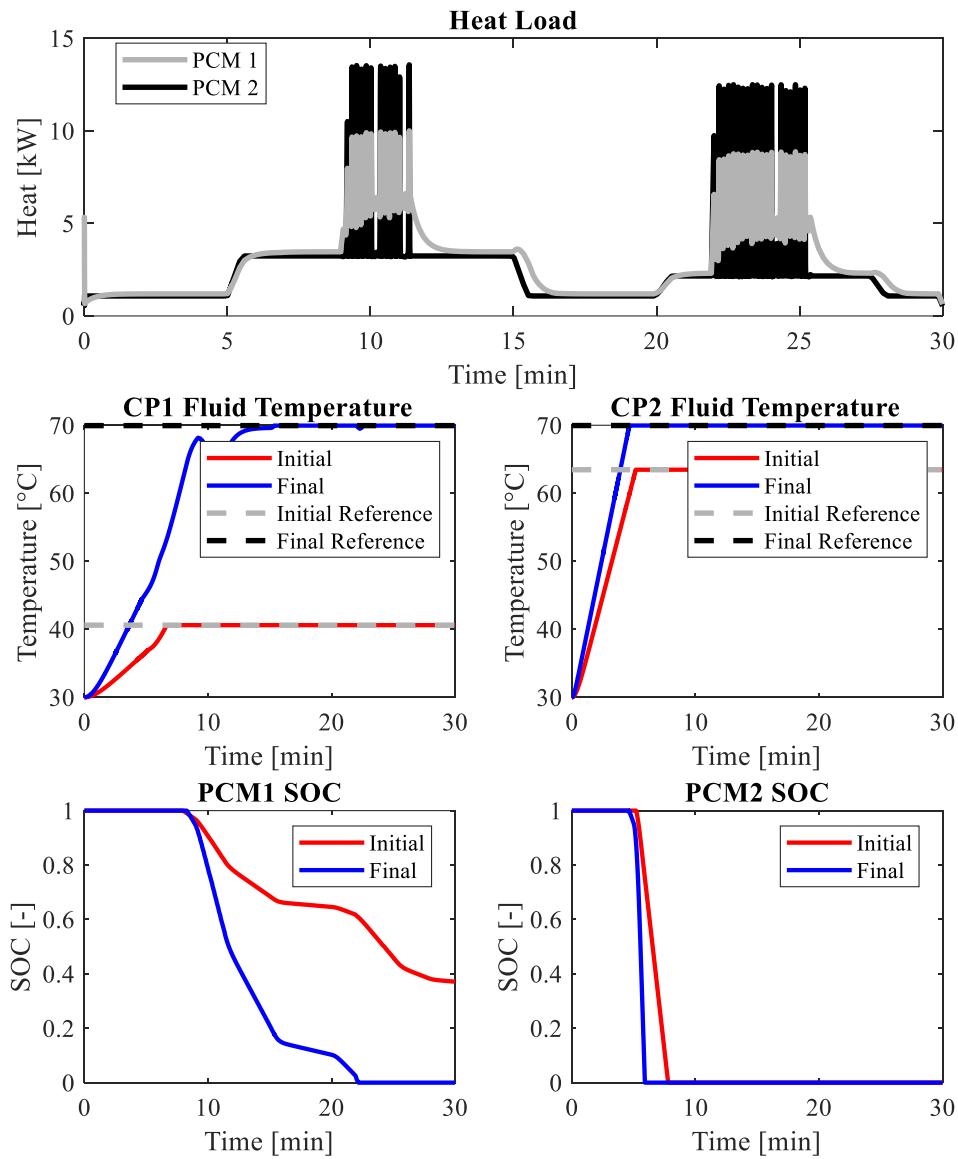
Figure 4.5: Comparison of selected trajectories of initial and final TESS designs.
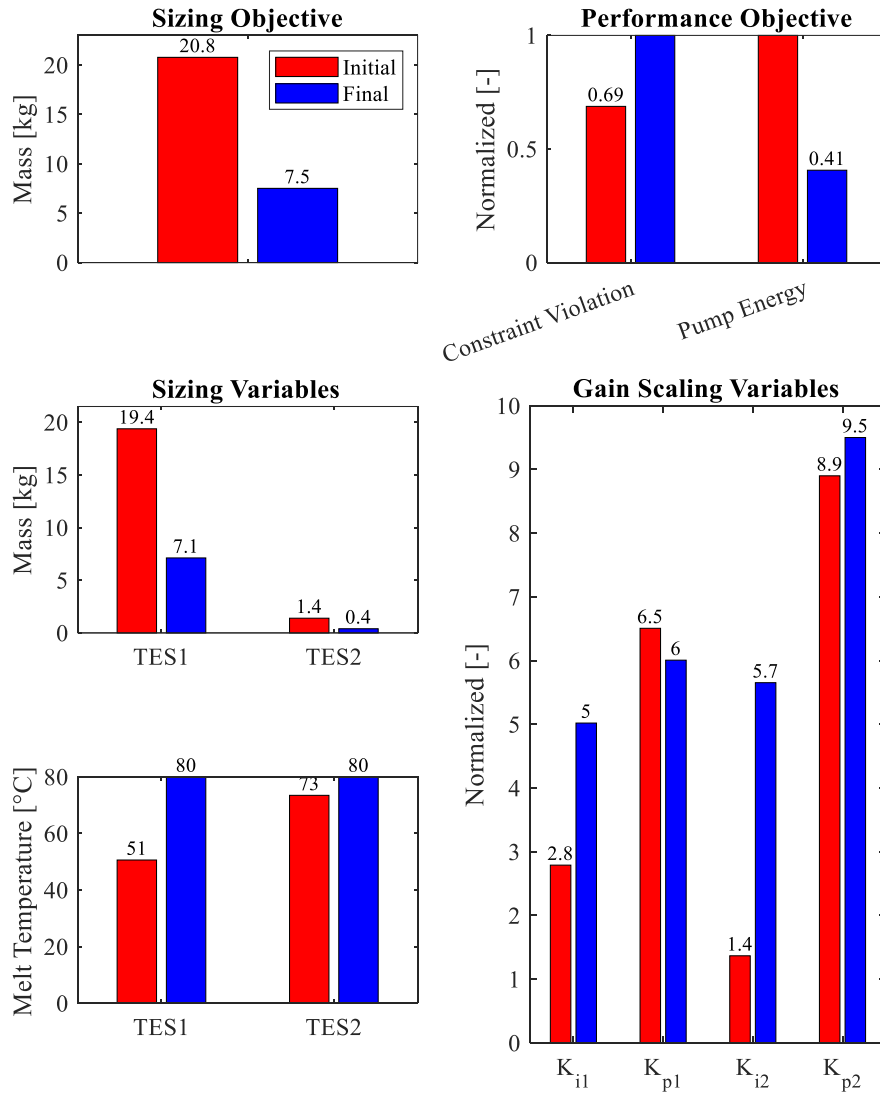
Figure 4.6: Comparison of objectives of initial and final TESS designs.
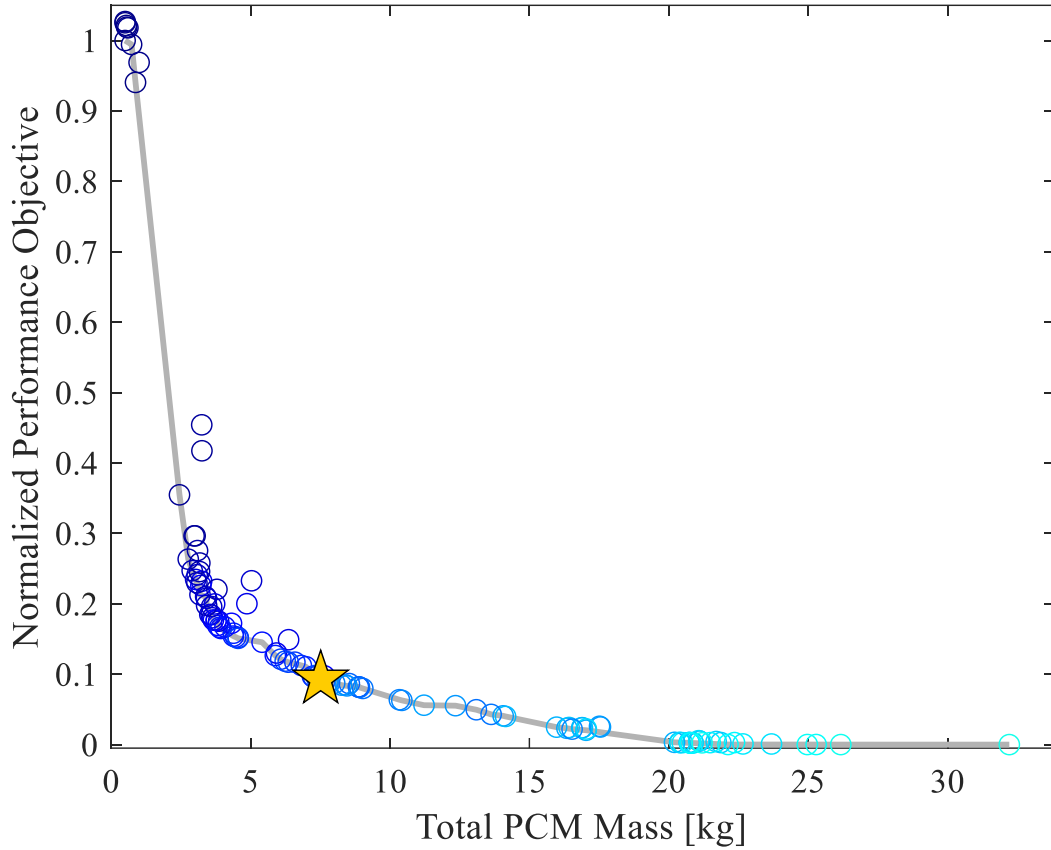
Figure 4.7: Sizing and performance tradeoff for TESS.

4.4 Hybrid Electro-Thermal Energy Storage System

As a final demonstration of the application of the design optimization framework, the sizing and control parameters of the HETESS will be optimized. Sizing of energy storage elements in the HETESS is determined by the combination of sizing variables θ^E for the HESS and θ^T for the TESS. As mentioned in 2.4.3, the TESS is modified in this system through the addition of a third TES module. With this addition, the sizing variables that define the HETESS are given by

$$\theta = \left\{ N_{p,batt} \quad N_{s,UC} \quad N_{p,UC} \quad m_1 \quad T_{m,1} \quad m_2 \quad T_{m,2} \quad m_3 \quad T_{m,3} \right\}, \tag{4.41}$$

where the first seven terms are the elements of θ^E and θ^T as described in the preceding sections, m_3 is the mass of PCM in the third TES module, and $T_{m,3}$ is the melt temperature of PCM in the

93

third TES module. In accordance with their treatment in the previous sections, all sizing variables are treated as continuously variable. Controller gains in the HETESS are modified using gain scaling variables $\phi = \{\phi^E \quad \phi^T\}$, which are also treated as continuously variable. The goals of this optimization study will combine the goals of the HESS and TESS optimization studies: minimizing size of the electro-thermal system while maximizing performance. These sizing and performance objectives will combine the sizing and performance objectives of the HESS and TESS optimization studies. Much of the setup for HETESS optimization is repeated from the HESS and TESS optimization studies, but the modifications made in 2.4.3 to build the HETESS necessitate modifications to the implementation of the design optimization framework from these subsystem optimization studies. For this reason, we will proceed once more through the steps of the framework to specify the optimization methodology for the electro-thermal system.

4.4.1 Graph-Based HETESS Model Augmentation

To augment the graph-based HETESS model, we begin by defining design matrices as in (4.1), starting with the design matrix Ψ_c corresponding to vertex capacitances. Since the battery model used for the HETESS is unchanged from the model used for the TESS, the battery capacitances Q, C_1, C_2, C_c, and C_s, corresponding to vertices q_1, V_2, V_3, T_4, and T_5 in the HETESS graph, will once more be given by (4.14). The corresponding entries in the capacitance design matrix are defined such that

$$\psi_{c,i}(\theta) = \theta_1 = N_{p,batt}, \quad i = 1,\ldots,5. \tag{4.42}$$

The HETESS model considered for this study uses the third-order ultracapacitor model described in 2.3.2, with capacitances C_i, C_D, and C_L dependent on the number of parallel ultracapacitor

cells according to $C' = N_{p,UC}C$. The corresponding entries in the capacitance design matrix are given by

$$\psi_{c,i}(\theta) = \theta_3 = N_{p,UC}, \quad i = 33,34,35. \tag{4.43}$$

Finally, the thermal capacitance C_c of the ultracapacitor pack is given by $C'_c = N_{s,UC}N_{p,UC}C_c$, so the corresponding entry in the capacitance design matrix is given by

$$\psi_{c,20}(\theta) = \theta_2\theta_3 = N_{s,UC}N_{p,UC}. \tag{4.44}$$

The remaining capacitances are independent of the design variables, so the remaining entries in Ψ_c are set to unity.

We next define the design matrix Ψ corresponding to power flows. Since the battery model is unchanged from the model used for the HESS, the elements of Ψ corresponding to resistive losses in the battery are once more given by (4.17) and (4.18). On the other hand, the third-order ultracapacitor model includes additional losses not accounted for in the first-order model used previously. These losses, represented by edges e_8, e_9, e_{10}, and e_{11} in Figure 2.8, are each given by I^2R in terms of the respective tail states I_i, I_D, I_L, and I_{leak}, and resistance parameters R_i, R_D, R_L, and R_{leak}. These resistance parameters are dependent upon the design variables as $R'_{i,D,L,leak} = R_{i,D,L,leak} / N_{p,UC}$, so the corresponding entries of the power flow design matrix are given by

$$\psi_i(\theta) = 1/\theta_3 = 1/N_{p,UC}. \tag{4.45}$$

Additionally, edge e_{13} in Figure 2.8 representing heat transfer between the ultracapacitor pack and TES module is given by $(T_1 - T_{PCM})/R$, with the resistance parameter given by

$R'_c = R_c / (N_{s,UC} N_{p,UC})$. The corresponding element of the power flow design matrix is then given by

$$\psi_i(\theta) = \theta_2 \theta_3 = N_{s,UC} N_{p,UC}. \tag{4.46}$$

Finally, recall that the modifications discussed at the end of section 2.3.2 give the voltage and temperature dynamics of cells within the pack. The edge e_{12} shown in Figure 2.8, however, should give the total power provided by the ultracapacitor pack, which is given in terms of the pack terminal voltage and current draw as $V_T I_1$. The terminal voltage is given by $V_T = N_{s,UC} V_1$, so the entry in the power flow design matrix corresponding to this edge is defined as

$$\psi_i(\theta) = \theta_2 = N_{s,UC}. \tag{4.47}$$

These are the only power flows in the HETESS model that have a design matrix representation, so the remaining elements of Ψ are set to unity.

There are no source flows in the HETESS model, so the Ψ^s design matrix is the identity matrix. Additionally, the third-order ultracapacitor model directly quantifies the pack terminal voltage as a function of the cell voltages and the number of series ultracapacitor cells, so the dependence of the initial ultracapacitor pack voltage on the design variables is already accounted for. Thus for the HETESS model the Ψ_0 matrix is also set to unity.

The next step towards augmentation of the HETESS graph-based model is the development of design operators to modify nonlinear edge maps based on the values of the design variables. This step is only necessary for edges having a PCM energy state as either their tail or head vertex, since the nonlinear edge maps describing PCM heat transfer are the only edge maps dependent on design variables. Referring to Figure 2.18, there are eight of these edges: two edges directed into/one edge out of state E_{26} representing heat loads to/from TES1, two edges directed into/one

edge out of state E_{25} representing heat loads to/from TES3, and one edge directed into/one edge directed out of state E_{27} representing heat loads to/from TES2. A design operator is defined for each of these edges with the same form as (4.30) and (4.31), parameterized appropriately in terms of the corresponding TES module parameters.

With design matrices and operators defined for the main elements of the graph model, we proceed to define design matrices for other elements of the model. This includes the design matrices modifying battery power constraints and temperature references for the controllers in the TES subsystem. These design matrices are constructed exactly as before in sections 4.2.1 and 4.3.1, albeit with additional ones on the diagonals accounting for the additional states introduced by integrating the HES and TES subsystems.

Lastly, the controller gain scaling variables will be used to modify the nominal values of the controller gains. For the HETESS, the set of gain scaling variables is obtained by concatenating the gain scaling variables for the two subsystems as

$$\phi = \left\{ \phi^E \ \phi^T \right\} = \left\{ \alpha_1^E \ \beta_1^E \ \alpha_2^E \ \beta_2^E \ \alpha_1^T \ \beta_1^T \ \alpha_2^T \ \beta_2^T \right\}. \tag{4.48}$$

These gain scaling variables modify the nominal controller gains according to (4.23) and (4.35) in the same way as before, and these modifications can be readily translated into a design matrix form.

4.4.2 HETESS Objective Function Definition

The objectives of HETESS optimization are to minimize size and maximize performance of the closed-loop system. The sizing objective is taken as the total mass of the electrical and thermal energy storage elements, given by

$$J_{size} = J_{size}^E + J_{size}^T = m_{batt} N_{p,batt} N_{s,batt} + m_{UC} N_{p,UC} N_{s,UC} + m_1 + m_2 + m_3. \tag{4.49}$$

The performance objective of the HETESS combines the state reference tracking, power reference tracking, and power constraint violation subobjectives of the HESS optimization study with the state constraint violation and pump energy subobjectives of the TESS optimization study. The total performance objective is obtained as a weighted sum of the performance objectives (4.27) and (4.38) of the HESS and TESS optimization studies, given by

$$J_{perf} = J_{perf}^{E} \Big/ \overline{J}_{perf}^{E} + J_{perf}^{T} \Big/ \overline{J}_{perf}^{T} \tag{4.50}$$

where $\overline{J}_{perf}^{E}$ and $\overline{J}_{perf}^{T}$ are normalization constants used to ensure the HES and TES subsystems provide nearly equal contributions to the overall performance objective [83]. Note that the weightings of electrical subobjectives (i.e., w_1, w_2, and w_3 in (4.25)) are kept at the same values used in the HESS optimization study. The same is true regarding the weightings of the thermal subobjectives in (4.37).

The sizing and performance objectives are aggregated into a single objective function using the weighted sum method, yielding the following overall optimization objective

$$J_{tot} = w_{size} J_{size} + w_{perf} J_{perf} \tag{4.51}$$

where w_{perf} and w_{size} quantify the relative importance of the performance and sizing objectives respectively on the total objective function.

4.4.3 Definition of HETESS Design Constraints

Constraints on the HETESS sizing variables θ are obtained by concatenating the constraints used for the HESS and TESS optimization studies. Upper and lower bounds for the HESS design variables θ^{E} are obtained as described in 4.2.3. Upper and lower bounds for TESS design variables θ^{T} are the same as those provided for TES1 and TES2 in (4.40), with two analogous constraints added for TES3.

Constraints on HETESS gain scaling variables ϕ are defined exactly as described in 4.2.3 and 4.3.3, allowing each gain scaling variable to vary up or down by up to a factor of 10.

4.4.4 Formulation and Solution of the HETESS Optimization Problem

The shooting method is used to formulate and solve the HETESS optimization problem. The augmented HETESS graph-based model is simulated in Simulink using the ode23tb solver under the same electrical load introduced in Figure 3.1, with a run time averaging around 30 seconds for the 30-minute simulation (around 60 times faster than real time). Given a set of design variables and weightings w_{perf} and w_{size}, the closed-loop simulation results are used to calculate the total objective function (4.51). A genetic algorithm is used to arrive at an optimal design for each set of weightings. For this study, the genetic algorithm function tolerance is set to 10^{-8} and the population size is set to 50. The crossover fraction is lowered, to varying extents, from its default value of 0.8 to promote diversity within the populations.

The results in Figure 4.8, Figure 4.9, and Figure 4.10 compare the best designs from the initial and final generations of the genetic algorithm for $w_{perf} = 0.12$ and $w_{size} = 0.88$, and Table 4.1 shows the values of the design variables for these designs. These two designs can be compared by considering the changes in each of the objectives from the initial design to the final design. The upper left plot of Figure 4.8 shows that, while both designs track the reference bus voltage well within 0.05V, the initial design provides more optimal state reference tracking. State constraint violations are minimal for both designs; as demonstrated in the middle two plots, temperatures are kept well within limits in both designs, and PCM SOCs remain above their lower bounds. In these plots, it appears that the cold plate fluid temperatures remain at their references. In fact, the fluid temperatures of cold plate 2 exceed their reference by <0.01°C for the initial design and 0.2°C for the final design. For this reason, the state constraint objective is very small in both designs but

larger for the final design, as shown in the tabulated values in Figure 4.9. Similarly, while the battery power tracking error is very small in both designs, the upper right plot of Figure 4.8 shows that battery power deviates slightly more from the reference in the final design. Neither design results in battery power exceeding its max constraint, since this subobjective is highly penalized in the overall objective function. It is interesting to note that pump energy consumption, while less than 1J for both designs, is larger for the final design than the initial design. In the initial design both cold plate fluid temperatures remain colder than their references, so the pump provides mass flow at its minimum level throughout the simulation. However, in the final design the fluid temperature of cold plate 2 meets its reference value early in the simulation, so the flow rates increase above their minimum level to track the reference. The lower value of pump energy in the final design suggests that the pump energy objective is nonconvex. Finally, the sizing metrics shown in Figure 4.10 demonstrate a significant improvement in the sizing objective from the initial to the final design. The sizing objective, total mass of energy storage elements, is reduced by 70%. Additionally, the volume of energy storage elements, although not explicitly considered in the optimization problem, is reduced by 60%. Note that if the selected final designs of the individual HESS and TESS designs were combined to form a hybrid electro-thermal system, the resulting system would exhibit poorer state tracking, increased state constraint violations, and higher mass than the final HETESS design shown in this analysis. This finding demonstrates the importance of incorporating multi-domain dynamics into the optimization formulation. Magnified views of the subplots of Figure 4.8 are provided in the appendix.
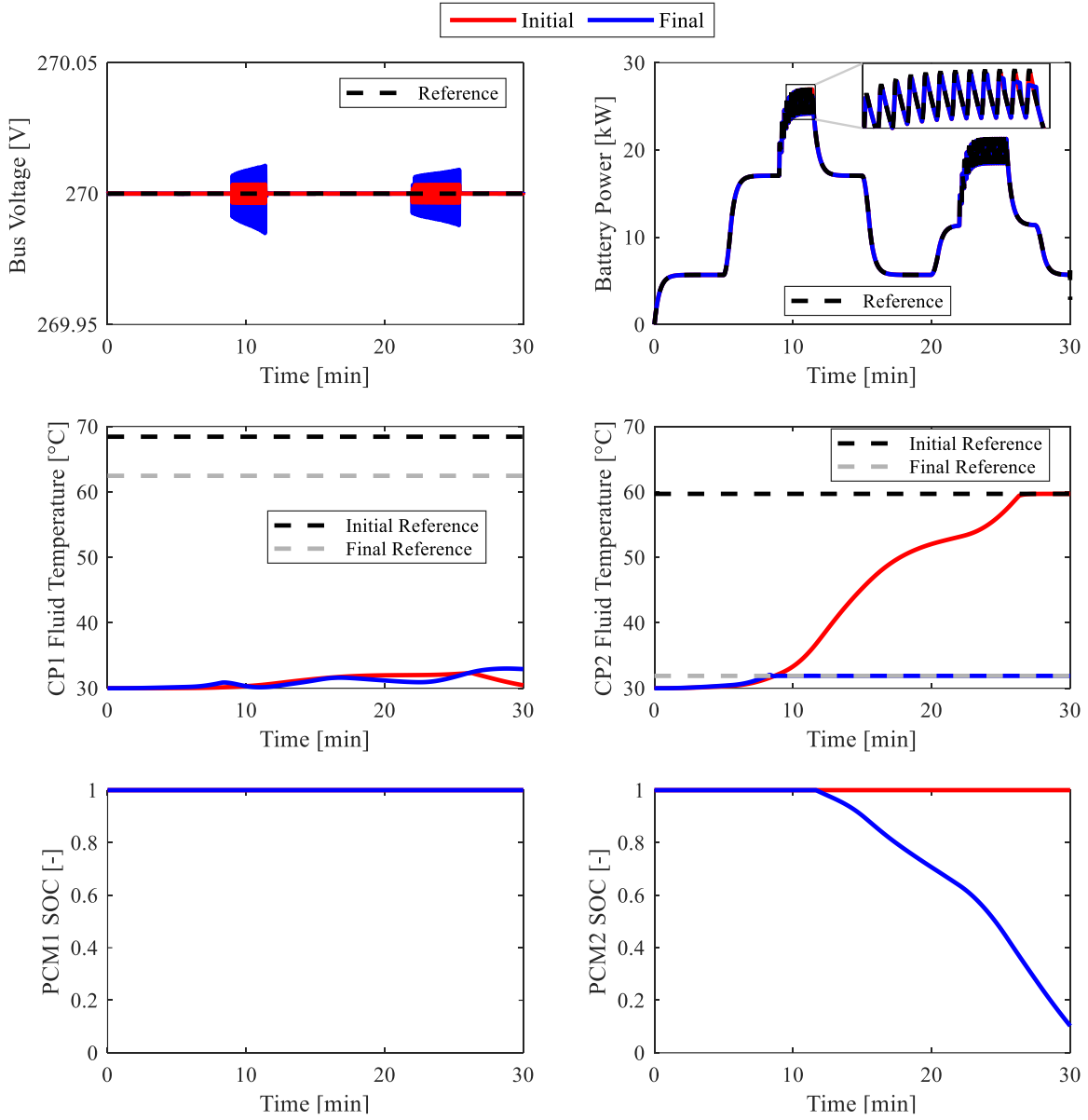
Figure 4.8: Comparison of selected trajectories of initial and final HETESS designs.
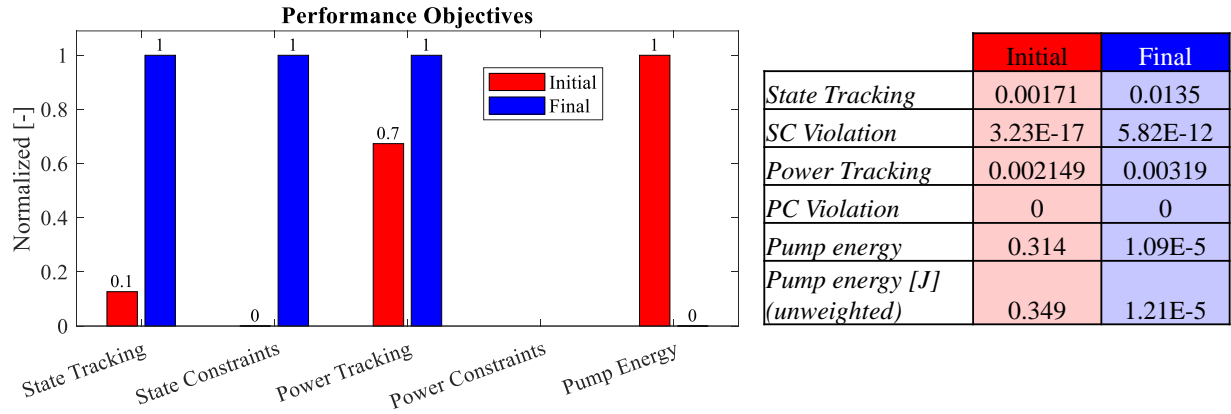
Figure 4.9: Comparison of performance objectives of initial and final HETESS designs.

	Initial	Final
State Tracking	0.00171	0.0135
SC Violation	3.23E-17	5.82E-12
Power Tracking	0.002149	0.00319
PC Violation	0	0
Pump energy	0.314	1.09E-5
Pump energy [J] (unweighted)	0.349	1.21E-5
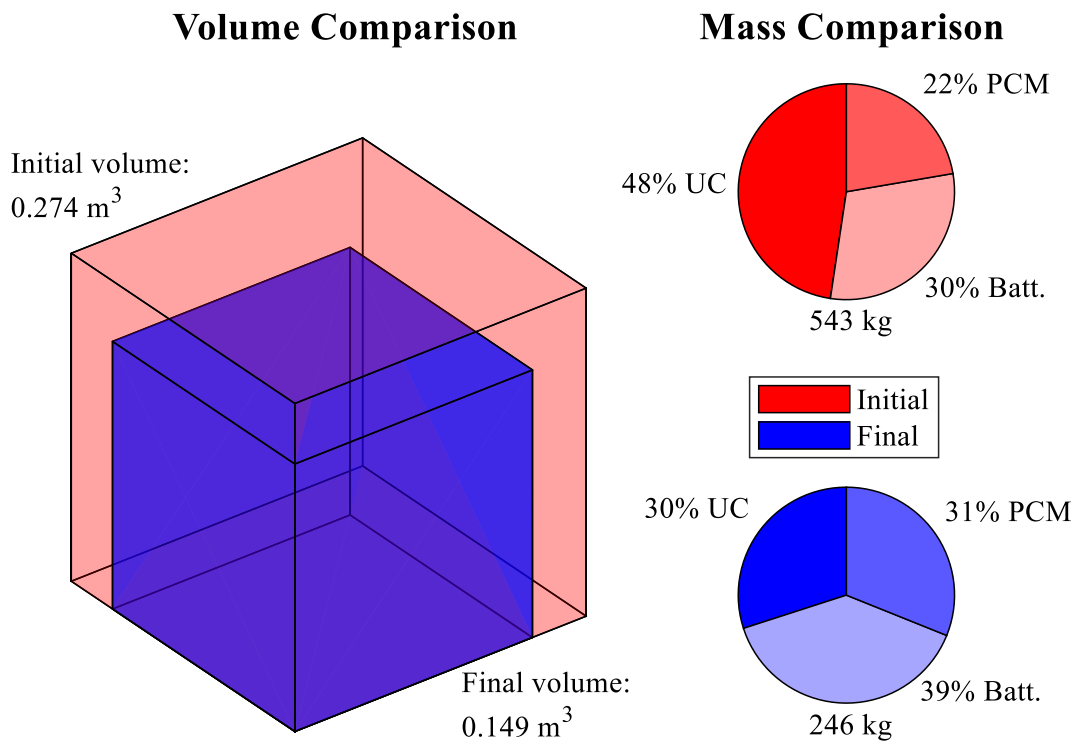
Figure 4.10: Comparison of initial and final HETESS sizing metrics.

Table 4.1: Comparison of initial and final values of HETESS design variables.

Design Variable	Initial Design	Final Design
$N_{p,batt}$	15	9
$N_{s,UC}$	356	245
$N_{p,UC}$	32	13
$K_{p,batt}$	3.7	4.1
$K_{i,batt}$	7.8	8.0
$K_{p,UC}$	9.8	10.0
$K_{i,UC}$	10.0	9.8
m_{TES1} [kg]	43.6	8.7
m_{TES2} [kg]	44.5	28.5
m_{TES3} [kg]	32.9	39.3
$T_{m,1}$ [°C]	78	72
$T_{m,2}$ [°C]	70	42
$T_{m,3}$ [°C]	65	36
K_{p1}	9.1	6.0
K_{i1}	4.2	8.2
K_{p2}	5.0	9.3
K_{i2}	5.2	2.0

The objective weightings w_{perf} and w_{size} are systematically varied to obtain a Pareto frontier quantifying tradeoffs between the sizing and performance objectives. Shown in Figure 4.11 is the Pareto frontier identified for the HETESS. In this figure, as before, lighter blue points correspond to higher values of w_{perf} while darker blue points correspond to higher values of w_{size}, and the gray line denotes the identified Pareto frontier. The starred point in this figure denotes the design corresponding to the preceding analysis. Note that in this study, the performance objective magnitudes are very low in comparison to the previous results for individual domain optimization studies. To ensure that the sizing and performance objectives contribute to the overall objective

function with similar magnitudes, the performance objective weight w_{perf} is scaled to a significantly larger value than its counterpart w_{size}.
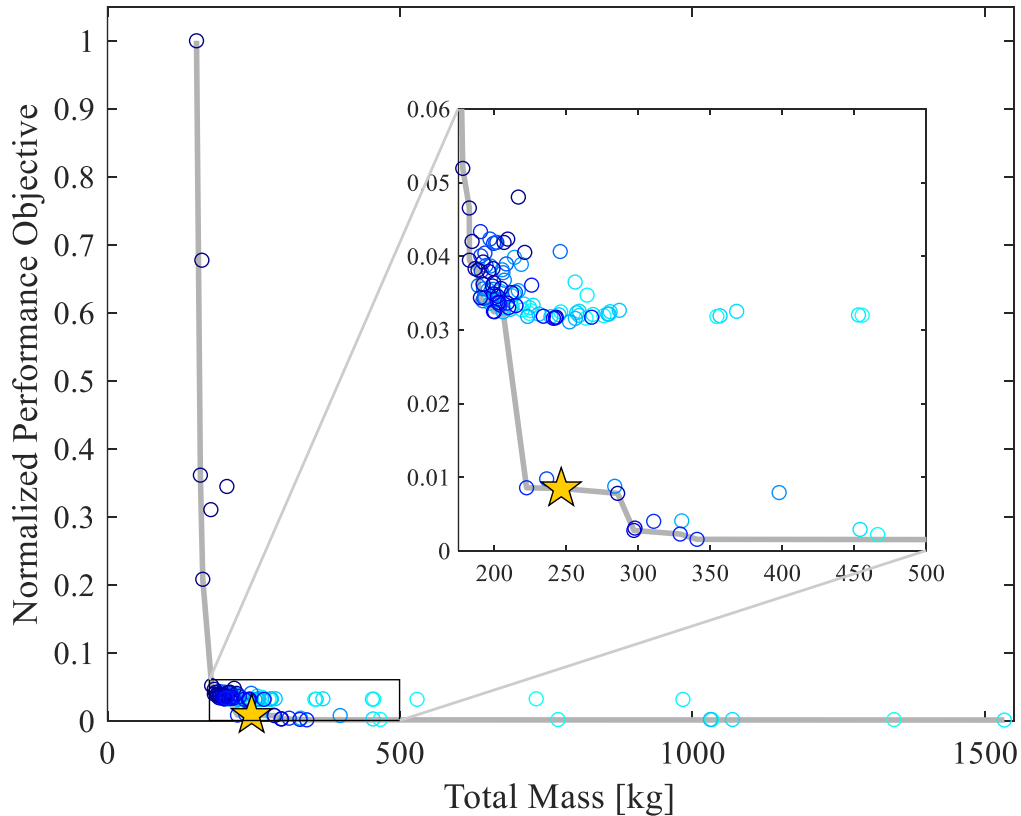
Figure 4.11: Sizing and performance tradeoff for HETESS.

As shown in Figure 4.11, there are some cases in which the optimizer converges to points lying far from the Pareto frontier. The emergence of these points indicates a nonconvex objective function consisting of strong local minima. To investigate the existence of these local minima, the HETESS optimization formulation was solved using the `gamultiobj` function in the Matlab optimization toolbox. Figure 4.12 shows the results obtained from this analysis. In the upper plot, all designs explored by the `gamultiobj` function are shown in black (referred to as GAMO Designs), and the points lying on the Pareto frontier identified by this function are starred in pink. Additionally, the designs from Figure 4.11 obtained using the weighted sum method are plotted

104

using their previously used coloring scheme (referred to as WS Designs), along with their Pareto frontier. The GAMO designs shown in this figure confirm the existence of strong local minima in the nonconvex performance objective. The lower plot shows the weighted contributions of each of the performance subobjectives – state tracking, state constraint (SC) violation, power tracking, power constraint (PC) violation, and pump energy – to the overall performance objective J_{perf}. These are plotted with respect to the sizing objective. From the lower plot it is clear that pump energy is nonconvex as a function of the sizing objective, and that pump energy dominates the objective function in this region. Note that, with such a highly nonconvex objective function, other multi-objective optimization methods, such as compromise programming, could be more effective than the weighted sum method used herein.
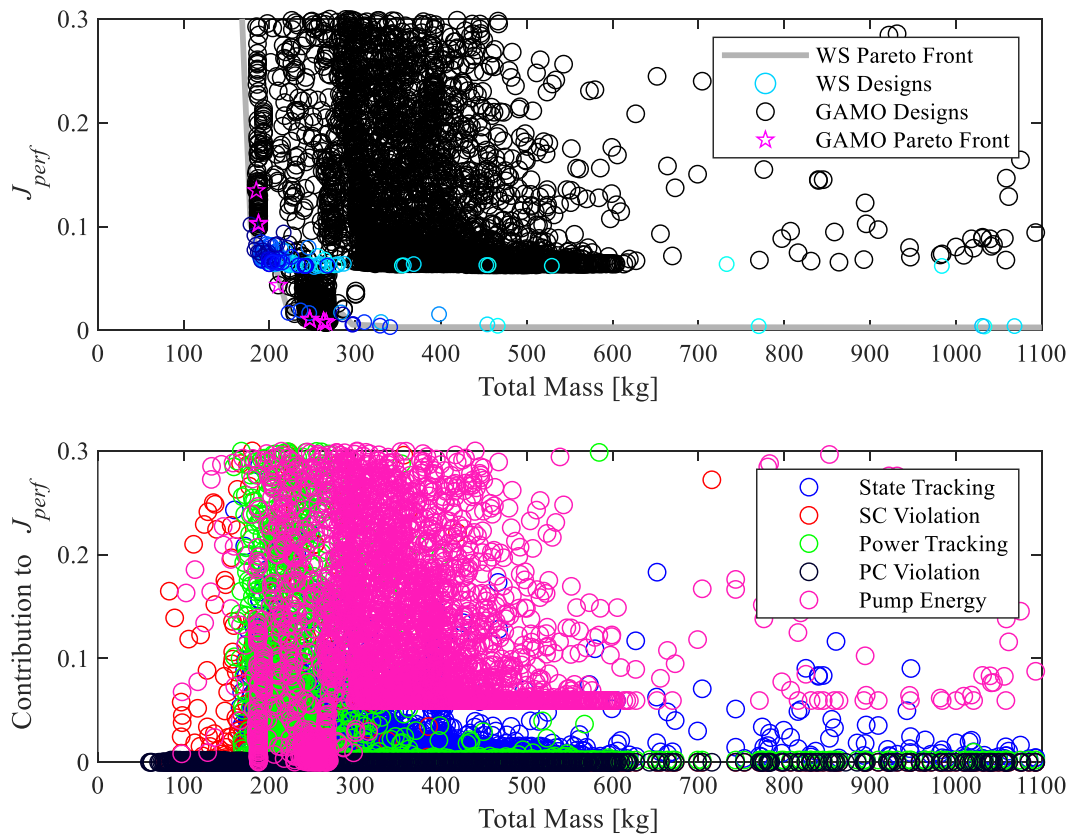
Figure 4.12: Weighted sum and `gamultiobj` optimization results for HETESS.

Finally, we compare the optimization results obtained by the sizing and control optimization study described in this section to a sizing-only optimization study. In the sizing-only study, the control gains are held constant at their nominal values given in Table 3.3, while the sizing variables are optimized. A significant improvement in the performance objective is noted when the control gains are included in the optimization formulation. This highlights the value of including control parameters in the system design process, in addition to the value added by incorporating multi-domain dynamics as discussed previously in this section.
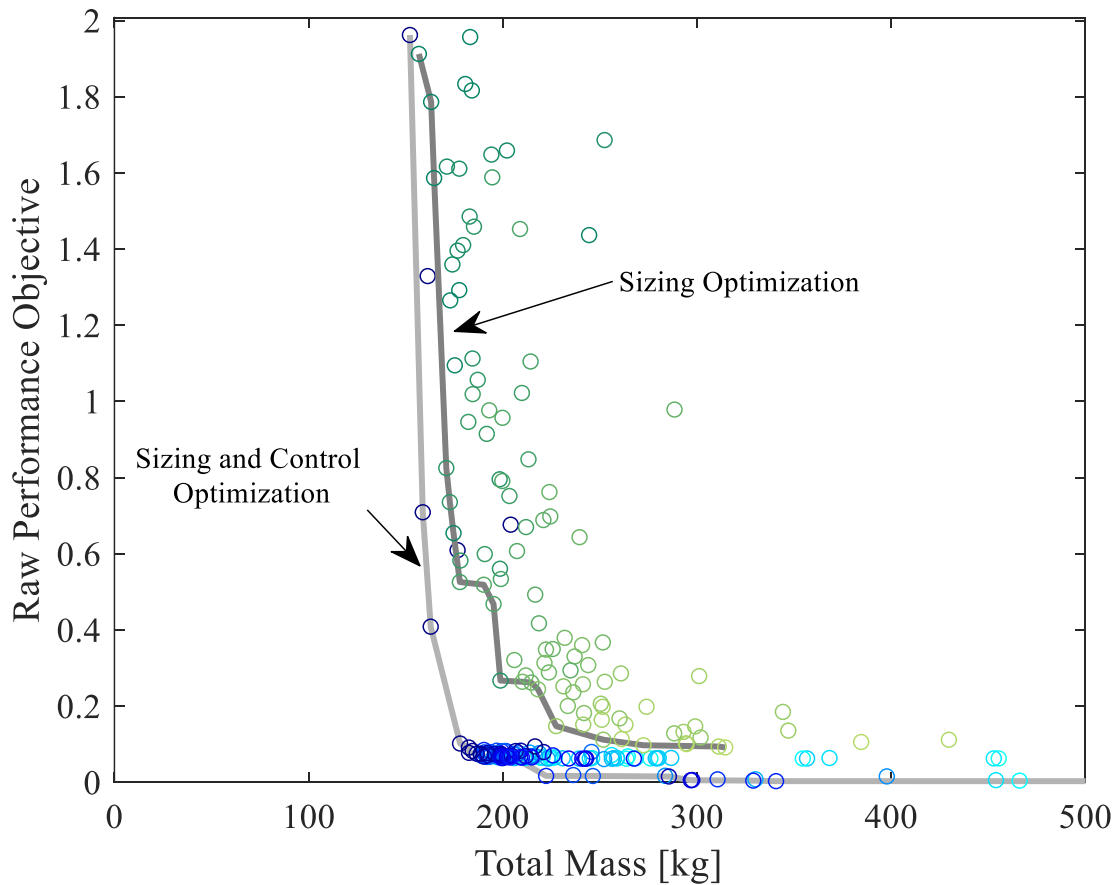
Figure 4.13: Performance improvement by including control parameters in HETESS optimization.

CHAPTER 5.   CONCLUSION

5.1   Summary of Contributions

Increased electrification of vehicles, including those with high ramp rate loads such as heavy construction and military vehicles, will rely on significant advances in onboard energy storage. Higher power density and efficient thermal management are key enablers to improve range and lifetime of onboard electrical energy storage, and the hybrid electro-thermal energy storage system introduced in Section 2.1 offers a power-dense solution for vehicles with high ramp rate loading cycles. The HETESS includes energy-dense batteries and power-dense ultracapacitors for electrical energy storage, and PCM thermal energy storage modules and coolant loops for thermal energy storage. In designing multi-domain systems such as this, optimization formulations should consider multi-domain dynamics and control to maximize the added benefit.

The graph-based energy modeling techniques employed in this work provide a unified framework to model multi-domain dynamics. A brief introduction to these graph-based techniques is given in Section 2.2. In Section 2.3, graph-based models are described for each of the electrical and thermal components considered in this work, including novel graph models of the ultracapacitor pack and TES modules. The graph models considered in this work consist of vertices representing current, voltage, temperature, and PCM stored energy, as well as edges representing electrical power transfer, resistive losses, and heat transfer. Component graph models are grouped to form the electrical (HESS) subsystem and the thermal (TESS) subsystem, and finally the two subsystems are merged to form the hybrid electro-thermal energy storage system. The HETESS is subjected to a current load with high ramp rate fluctuations.

Chapter 3 describes the control strategies employed for closed-loop control of the HETESS and its subsystems. Proportional-integral controllers are selected for their computational

efficiency. The HESS controllers seek to maintain bus voltage and prevent the battery pack from supplying damagingly high discharge rates. The latter is accomplished by regulating the battery pack power output to the low-pass-filtered value of the load power. The TESS controllers seek to cool the TES modules by regulating the cold plate fluid temperatures to reference values which are determined using the PCM melt temperatures. Simulation results demonstrate the effectiveness of these control approaches in both the subsystems as well as the HETESS.

Chapter 4 describes the graph-based optimization framework used in this work, building upon the multi-domain graph-based modeling framework described in Chapter 2. The first step in the optimization framework is to augment the graph-based model to capture the effects of the changing design variables on elements of the graph. The next step is to define the objective function, which may be a function of the design variables themselves or of simulation results for the augmented graph-based model, or a combination of multiple objectives. In the third step of the framework, constraints are defined for the design variables. The final step in the framework is to formulate and solve the optimization problem. The optimization framework is demonstrated step-by-step for the HESS and TESS subsystems as well as for the HETESS. In each of these studies, sizing and control parameters of the energy storage systems are optimized to minimize mass and maximize performance. Results of these demonstrations highlight the utility of the optimization framework as a tool to determine relationships and tradeoffs between competing objectives, such as the sizing and performance objectives considered herein. In the HESS and TESS optimization studies, it is noted that optimized designs retain a high level of performance while achieving significant reductions in mass compared to their respective initial designs. These improvements are further increased in the HETESS optimization study, which simultaneously varies sizing and control parameters of the electrical and thermal subsystems. Finally, it is noted that the inclusion

of control parameters in the optimization formulation leads to significant improvements in performance metrics.

5.2   Future Work

The design optimization studies in this thesis demonstrate applications of a design optimization framework for multi-domain systems and their controllers. Future work will consider further applications of the framework and the inclusion of more advanced controllers. Regarding the former, future work will include application of the framework to more complex systems and systems-of-systems. Future work will also focus on experimental validation of the optimization framework for sizing and control optimization of energy storage systems. In addition to these applications of the framework, an important future step is to include more advanced optimization techniques and algorithms within the design optimization framework. While a conventional genetic algorithm is used to optimize the weighted-sum objective function in this thesis, more advanced techniques such as hybrid optimization methods or surrogate modeling could have been used to arrive at optimal solutions with a higher degree of accuracy or in a more computationally efficient manner. Regarding the inclusion of more advanced controllers, optimal control strategies as discussed in Chapter 3 promise improved performance metrics in comparison to the heuristic control strategies used in this thesis. Future work will apply some of these optimal control strategies, such as model predictive control, to systems designed using the optimization framework. Due to the longer solution time of optimal control strategies compared to heuristic strategies, this step will likely rely on the inclusion of computationally efficient optimization algorithms within the optimization framework.

REFERENCES

[1]   A. Runge-Metzger, "A Clean Planet for all. A European long-term strategic vision for a prosperous, modern, competitive and climate neutral economy," Brussels, 2018.

[2]   S. L. Myers, "China's Pledge to Be Carbon Neutral by 2060: What It Means," *The New York Times*, Sep. 23, 2020.

[3]   International Energy Agency, "Global EV Outlook 2020," OECD, Jun. 2020.

[4]   U.S. Department of Energy, "Electrical and Electronics Technical Team Roadmap," *U.S. DRIVE Partnership*, 2017.

[5]   Cox Automotive, "Evolution of mobility: the path to electric vehicle adoption," Atlanta, GA, 2019.

[6]   K. Smith, E. Wood, S. Santhanagupalan, G. H. Kim, Y. Shi, and A. Pesaran, "Predictive Models of Li-ion Battery Lifetime," *IEEE Conference on Reliability Science for Advanced Materials and Devices*, 2014.

[7]   R. Hemmati and H. Saboori, "Emergence of hybrid energy storage systems in renewable energy and transport applications – A review," *Renew. Sustain. Energy Rev.*, vol. 65, pp. 11–23, Nov. 2016.

[8]   R. Xiong, H. Chen, C. Wang, and F. Sun, "Towards a smarter hybrid energy storage system based on battery and ultracapacitor - A critical review on topology and energy management," *J. Clean. Prod.*, vol. 202, pp. 1228–1240, Nov. 2018.

[9]   A. Ostadi, M. Kazerani, and S. K. Chen, "Hybrid Energy Storage System (HESS) in vehicular applications: A review on interfacing battery and ultra-capacitor units," *IEEE Transportation Electrification Conference and Expo*, 2013.

[10]   J. P. Zheng, T. R. Jow, and M. S. Ding, "Hybrid power sources for pulsed current applications," *IEEE Trans. Aerosp. Electron. Syst.*, vol. 37, no. 1, pp. 288–292, 2001.

[11]   A. Kuperman and I. Aharon, "Battery-ultracapacitor hybrids for pulsed current loads: A review," *Renew. Sustain. Energy Rev.*, vol. 15, no. 2, pp. 981–992, 2011.

[12]   C. E. Laird and A. G. Alleyne, "A hybrid electro-thermal energy storage system for high ramp rate power applications," *Dynamic Systems and Control Conference*, 2019.

[13]   S. J. Moura, J. B. Siegel, D. J. Siegel, H. K. Fathy, and A. G. Stefanopoulou, "Education on vehicle electrification: Battery systems, fuel cells, and hydrogen," *IEEE Vehicle Power and Propulsion Conference*, 2010.

[14]   F. Reno, "Optimizing the trajectory of a wheel loader working in short loading cycles," *Proceedings from the 13th Scandinavian International Conference on Fluid Power*, Sep.

2013.

[15] S. Hui and J. Junqing, "Research on the system configuration and energy control strategy for parallel hydraulic hybrid loader," *Autom. Constr.*, vol. 19, no. 2, pp. 213–220, Mar. 2010.

[16] C. B. Baxi and T. Knowles, "Thermal energy storage for solid-state laser weapons systems," *J. Dir. Energy*, vol. 1, no. 4, pp. 293–308, 2006.

[17] M. Garcia-Sanz, "Control Co-Design: An engineering game changer," *Adv. Control Appl. Eng. Ind. Syst.*, vol. 1, no. 1, Dec. 2019.

[18] J. R. R. A. Martins and A. B. Lambe, "Multidisciplinary design optimization: A survey of architectures," *AIAA J.*, vol. 51, no. 9, pp. 2049–2075, Sep. 2013.

[19] J. T. Allison and D. R. Herber, "Multidisciplinary design optimization of dynamic engineering systems," *AIAA J.*, vol. 52, no. 4, pp. 691–710, 2014.

[20] A. E. Bayrak, N. Kang, and P. Y. Papalambros, "Decomposition-Based Design Optimization of Hybrid Electric Powertrain Architectures: Simultaneous Configuration and Sizing Design," *J. Mech. Des.*, vol. 138, no. 7, Jul. 2016.

[21] A. E. Bayrak, Y. Ren, and P. Y. Papalambros, "Topology Generation for Hybrid Electric Vehicle Architecture Design," *J. Mech. Des.*, vol. 138, no. 8, Aug. 2016.

[22] J. Jalving, Y. Cao, and V. M. Zavala, "Graph-based modeling and simulation of complex systems," *Comput. Chem. Eng.*, vol. 125, pp. 134–154, 2019.

[23] D. J. Docimo, Z. Kang, K. A. James, and A. G. Alleyne, "A Novel Framework for Simultaneous Topology and Sizing Optimization of Complex, Multi-Domain Systems-of-Systems," *J. Mech. Des.*, vol. 142, pp. 1–37, 2020.

[24] J. Shen, A. Hasanzadeh, and A. Khaligh, "Optimal power split and sizing of hybrid energy storage system for electric vehicles," *IEEE Transportation Electrification Conference and Expo*, 2014.

[25] R. E. Araújo, R. De Castro, C. Pinto, P. Melo, and D. Freitas, "Combined sizing and energy management in EVs with batteries and supercapacitors," *IEEE Trans. Veh. Technol.*, vol. 63, no. 7, pp. 3062–3076, Sep. 2014.

[26] X. Hu, L. Johannesson, N. Murgovski, and B. Egardt, "Longevity-conscious dimensioning and power management of the hybrid energy storage system in a fuel cell hybrid electric bus," *Appl. Energy*, vol. 137, pp. 913–924, Jan. 2015.

[27] J. Shen, S. Dusmez, and A. Khaligh, "Optimization of sizing and battery cycle life in battery/ultracapacitor hybrid energy storage systems for electric vehicle applications," *IEEE Trans. Ind. Informatics*, vol. 10, no. 4, pp. 2112–2121, 2014.

[28] S. Wen *et al.*, "Optimal sizing of hybrid energy storage sub-systems in PV/diesel ship power system using frequency analysis," *Energy*, vol. 140, pp. 198–208, 2017.

[29] Z. Song, H. Hofmann, J. Li, X. Han, and M. Ouyang, "Optimization for a hybrid energy storage system in electric vehicles using dynamic programing approach," *Appl. Energy*, vol. 139, pp. 151–162, Feb. 2015.

[30] Z. Song, J. Hou, S. Xu, M. Ouyang, and J. Li, "The influence of driving cycle characteristics on the integrated optimization of hybrid energy storage system for electric city buses," *Energy*, vol. 135, pp. 91–100, Sep. 2017.

[31] A. Al Mamun, Z. Liu, D. M. Rizzo, and S. Onori, "An integrated design and control optimization framework for hybrid military vehicle using lithium-ion battery and supercapacitor as energy storage devices," *IEEE Trans. Transp. Electrif.*, vol. 5, no. 1, pp. 239–251, 2019.

[32] H. H. Eldeeb, A. T. Elsayed, C. R. Lashway, and O. Mohammed, "Hybrid Energy Storage Sizing and Power Splitting Optimization for Plug-In Electric Vehicles," *IEEE Trans. Ind. Appl.*, vol. 55, no. 3, pp. 2252–2262, May 2019.

[33] P. Saenger, N. Devillers, K. Deschinkel, M. C. Pera, R. Couturier, and F. Gustin, "Optimization of Electrical Energy Storage System Sizing for an Accurate Energy Management in an Aircraft," *IEEE Trans. Veh. Technol.*, vol. 66, no. 7, pp. 5572–5583, 2017.

[34] N. Javani, I. Dincer, G. F. Naterer, and B. S. Yilbas, "Exergy analysis and optimization of a thermal management system with phase change material for hybrid electric vehicles," *Appl. Therm. Eng.*, vol. 64, no. 1–2, pp. 471–482, Mar. 2014.

[35] S. M. Aceves, H. Nakamura, G. M. Reistad, and J. Martinez-Frias, "Optimization of a class of latent thermal energy storage systems with multiple phase-change materials," *J. Sol. Energy Eng.*, vol. 120, no. 1, pp. 14–19, Feb. 1998.

[36] A. Stupar, U. Drofenik, and J. W. Kolar, "Optimization of phase change material heat sinks for low duty cycle high peak load power supplies," *IEEE Trans. Components, Packag. Manuf. Technol.*, vol. 2, no. 1, pp. 102–115, Jan. 2012.

[37] D. Kong, R. Peng, P. Ping, J. Du, G. Chen, and J. Wen, "A novel battery thermal management system coupling with PCM and optimized controllable liquid cooling for different ambient temperatures," *Energy Convers. Manag.*, vol. 204, Jan. 2020.

[38] V. Shanmugasundaram, J. R. Brown, and K. L. Yerkes, "Thermal management of high heat-flux sources using phase change materials: A design optimization procedure," *32nd Thermophysics Conference*, 1997.

[39] G. P. Henze, R. H. Dodier, and M. Krarti, "Development of a predictive optimal controller for thermal energy storage systems," *HVAC R Res.*, vol. 3, no. 3, pp. 233–264, 1997.

[40] Y. Ma, A. Kelman, A. Daly, and F. Borrelli, "Predictive control for energy efficient buildings with thermal storage: Modeling, simulation, and experiments," *IEEE Control Syst. Mag.*, vol. 32, no. 1, pp. 44–64, 2012.

[41] J. A. Candanedo, V. R. Dehkordi, and M. Stylianou, "Model-based predictive control of an ice storage device in a building cooling system," *Appl. Energy*, vol. 111, pp. 1032–1045, Nov. 2013.

[42] H. C. Pangborn, C. E. Laird, and A. G. Alleyne, "Hierarchical Hybrid MPC for Management of Distributed Phase Change Thermal Energy Storage," *American Control Conference*, 2020.

[43] H. Mehrjerdi and E. Rakhshani, "Optimal operation of hybrid electrical and thermal energy storage systems under uncertain loading condition," *Appl. Therm. Eng.*, vol. 160, Sep. 2019.

[44] A. Baniasadi, D. Habibi, W. Al-Saedi, M. A. S. Masoum, C. K. Das, and N. Mousavi, "Optimal sizing design and operation of electrical and thermal energy storage systems in smart buildings," *J. Energy Storage*, vol. 28, Apr. 2020.

[45] M. Giuntoli and D. Poli, "Optimized thermal and electrical scheduling of a large scale virtual power plant in the presence of energy storages," *IEEE Trans. Smart Grid*, vol. 4, no. 2, pp. 942–955, 2013.

[46] M. M. S. Khan and M. O. Faruque, "Management of hybrid energy storage systems for MVDC power system of all electric ship," *Proceedings of the 48th North American Power Symposium*, 2016.

[47] T. Zimmermann, P. Keil, M. Hofmann, M. F. Horsche, S. Pichlmaier, and A. Jossen, "Review of system topologies for hybrid electrical energy storage systems," *J. Energy Storage*, vol. 8, pp. 78–90, 2016.

[48] C. T. Aksland, "Modular Modeling And Control of A Hybrid Unmanned Aerial Vehicle's Powertrain," MS Thesis, University of Illinois at Urbana-Champaign, 2019.

[49] M. A. Williams, J. P. Koeln, H. C. Pangborn, and A. G. Allenye, "Dynamical Graph Models of Aircraft Electrical, Thermal, and Turbomachinery Components," *J. Dyn. Syst. Meas. Control*, vol. 140, no. 4, pp. 1–17, 2018.

[50] J. P. Koeln, M. A. Williams, H. C. Pangborn, and A. G. Alleyne, "Experimental validation of graph-based modeling for thermal fluid power flow systems," *Dynamic Systems and Control Conference*, 2016.

[51] J. P. Koeln, "Hierarchical Power Management in Vehicle Systems," PhD Dissertation, University of Illinois at Urbana-Champaign, 2016.

[52] D. J. Docimo and A. G. Alleyne, "Electro-Thermal Graph-Based Modeling for Hierarchical Control with Application to an Electric Vehicle," *IEEE Conference on*

Control Technology and Applications, 2018.

[53] H. C. Pangborn, J. P. Koeln, M. A. Williams, and A. G. Alleyne, "Experimental validation of graph-based hierarchical control for thermal management," *J. Dyn. Syst. Meas. Control*, vol. 140, no. 10, pp. 1–16, 2018.

[54] H. C. Pangborn, "Hierarchical control for multi-domain coordination of vehicle energy systems with switched dynamics," PhD Dissertation, University of Illinois at Urbana-Champaign, 2019.

[55] H. E. Perez, J. B. Siegel, X. Lin, A. G. Stefanopoulou, Y. Ding, and M. P. Castanier, "Parameterization and validation of an integrated electro-thermal cylindrical lfp battery model," *Dynamic Systems and Control Conference*, 2012.

[56] L. Zubieta and R. Bonert, "Characterization of double-layer capacitors for power electronics applications," *IEEE Trans. Ind. Appl.*, vol. 36, no. 1, pp. 199–205, Jan. 2000.

[57] R. Carter, A. Cruden, and P. J. Hall, "Optimizing for efficiency or battery life in a battery/supercapacitor electric vehicle," *IEEE Trans. Veh. Technol.*, vol. 61, no. 4, pp. 1526–1533, 2012.

[58] Z. Li, O. Onar, A. Khaligh, and E. Schaltz, "Design, control, and power management of a battery/ultra-capacitor hybrid system for small electric vehicles," *SAE Technical Papers*, 2009.

[59] O. C. Onar and A. Khaligh, "A novel integrated magnetic structure based DC/DC converter for hybrid battery/ultracapacitor energy storage systems," *IEEE Trans. Smart Grid*, vol. 3, no. 1, pp. 296–307, 2012.

[60] L. Gao, R. A. Dougal, and S. Liu, "Power enhancement of an actively controlled battery/ultracapacitor hybrid," *IEEE Trans. Power Electron.*, vol. 20, no. 1, pp. 236–243, Jan. 2005.

[61] A. Santucci, A. Sorniotti, and C. Lekakou, "Power split strategies for hybrid energy storage systems for vehicular applications," *J. Power Sources*, vol. 258, pp. 395–407, Jul. 2014.

[62] J. Shen and A. Khaligh, "A supervisory energy management control strategy in a battery/ultracapacitor hybrid energy storage system," *IEEE Trans. Transp. Electrif.*, vol. 1, no. 3, pp. 223–231, 2015.

[63] B. Hredzak, V. G. Agelidis, and M. Jang, "A model predictive control system for a hybrid battery-ultracapacitor power source," *IEEE Trans. Power Electron.*, vol. 29, no. 3, pp. 1469–1479, 2014.

[64] S. Zhang, R. Xiong, and F. Sun, "Model predictive control for power management in a plug-in hybrid electric vehicle with a hybrid energy storage system," *Appl. Energy*, vol. 185, pp. 1654–1662, 2017.

[65]   M. E. Choi, J. S. Lee, and S. W. Seo, "Real-time optimization for power management systems of a battery/supercapacitor hybrid energy storage system in electric vehicles," *IEEE Trans. Veh. Technol.*, vol. 63, no. 8, pp. 3600–3611, Oct. 2014.

[66]   J. Cao, Z. Ling, X. Fang, and Z. Zhang, "Delayed liquid cooling strategy with phase change material to achieve high temperature uniformity of Li-ion battery under high-rate discharge," *J. Power Sources*, vol. 450, 2020.

[67]   S. E. Shafiei and A. Alleyne, "Model predictive control of hybrid thermal energy systems in transport refrigeration," *Appl. Therm. Eng.*, vol. 82, pp. 264–280, 2015.

[68]   A. Mawire and M. McPherson, "Experimental characterisation of a thermal energy storage system using temperature and power controlled charging," *Renew. Energy*, vol. 33, no. 4, pp. 682–693, 2008.

[69]   Y. Sun, S. Wang, F. Xiao, and D. Gao, "Peak load shifting control using different cold thermal energy storage facilities in commercial buildings: A review," *Energy Convers. Manag.*, vol. 71, pp. 101–114, 2013.

[70]   A. Tam, D. Ziviani, J. E. Braun, and N. Jain, "Development and evaluation of a generalized rule-based control strategy for residential ice storage systems," *Energy Build.*, vol. 197, pp. 99–111, 2019.

[71]   G. P. Henze, C. Felsmann, and G. Knabe, "Evaluation of optimal control for active and passive building thermal storage," *Int. J. Therm. Sci.*, vol. 43, no. 2, pp. 173–183, Feb. 2004.

[72]   G. P. Henze, R. H. Dodier, and M. Krarti, "Development of a predictive optimal controller for thermal energy storage systems," *ASHRAE Trans.*, vol. 104, 1998.

[73]   Y. Ma, F. Borrelli, B. Hencey, B. Coffey, S. Bengea, and P. Haves, "Model predictive control for the operation of building cooling systems," *IEEE Trans. Control Syst. Technol.*, vol. 20, no. 3, pp. 796–803, May 2012.

[74]   B. D. Skurdal and R. L. Gaigler, "Multimission electromagnetic launcher," *IEEE Trans. Magn.*, vol. 45, no. 1, pp. 458–461, Jan. 2009.

[75]   C. Laird, D. Docimo, C. T. Aksland, and A. G. Alleyne, "Graph-Based Design and Control Optimization of a Hybrid Electrical Energy Storage System," *Dynamic Systems and Control Conference*, 2020.

[76]   L. A. Zadeh, "Optimality and Non-Scalar-Valued Performance Criteria," *IEEE Trans. Automat. Contr.*, vol. 8, no. 1, pp. 59–60, 1963.

[77]   W. H. Press, Ed., *Numerical recipes: the art of scientific computing*, 3rd ed. Cambridge, UK ; New York: Cambridge University Press, 2007.

[78]   J. T. Betts, *Practical Methods for Optimal Control and Estimation Using Nonlinear*

Programming. Society for Industrial and Applied Mathematics, 2010.

[79] Advanced Cooling Technologies, "Phase Change Material (PCM) Selection."
      https://www.1-act.com/products/pcm-heat-sinks/pcmselection/.

[80] ExxonMobil, "Parvan - Fully Refined Paraffin Wax."
      https://www.exxonmobil.com/en/wax/fully-refined-paraffin-wax.

[81] RubiTherm, "PCM RT-Line."
      https://www.rubitherm.eu/en/index.php/productcategory/organische-pcm-rt.

[82] M. A. Williams, "A framework for the control of electro-thermal aircraft power systems,"
      PhD Dissertation, University of Illinois at Urbana-Champaign, 2017.

[83] D. Docimo, Z. Kang, K. James, and A. Alleyne, "Plant and Controller Optimization for
      Power and Energy Systems with Model Predictive Control," *J. Dyn. Syst. Meas. Control*,
      Mar. 2021.

APPENDIX: SELECTED FIGURES FROM TEXT

This appendix provides larger versions of selected figures from the text in the following order: Figure 3.4, Figure 3.7, Figure 3.8, Figure 4.1, Figure 4.5, and Figure 4.8.

Figure 3.4: Closed-loop HESS simulation results.
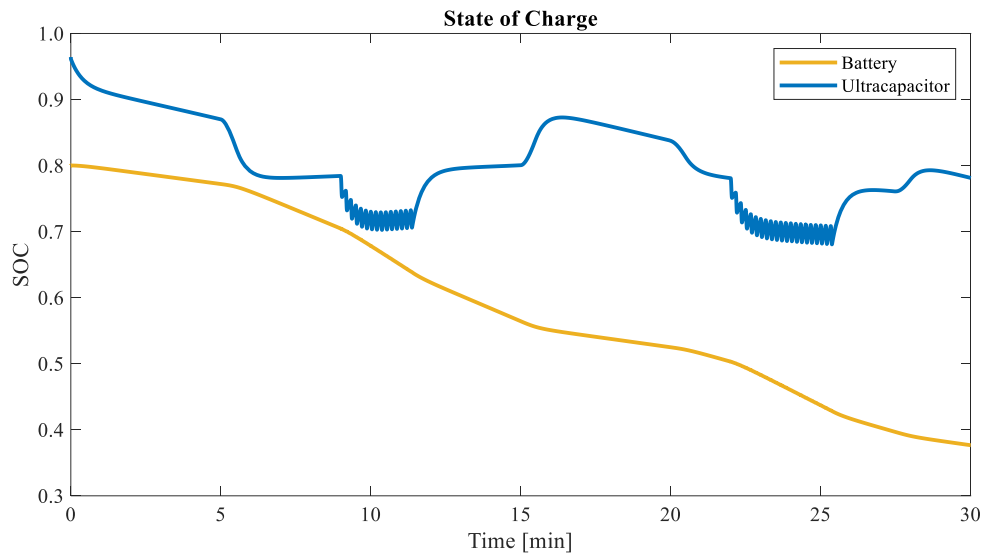
Figure 3.4 a) SOC of energy storage elements.
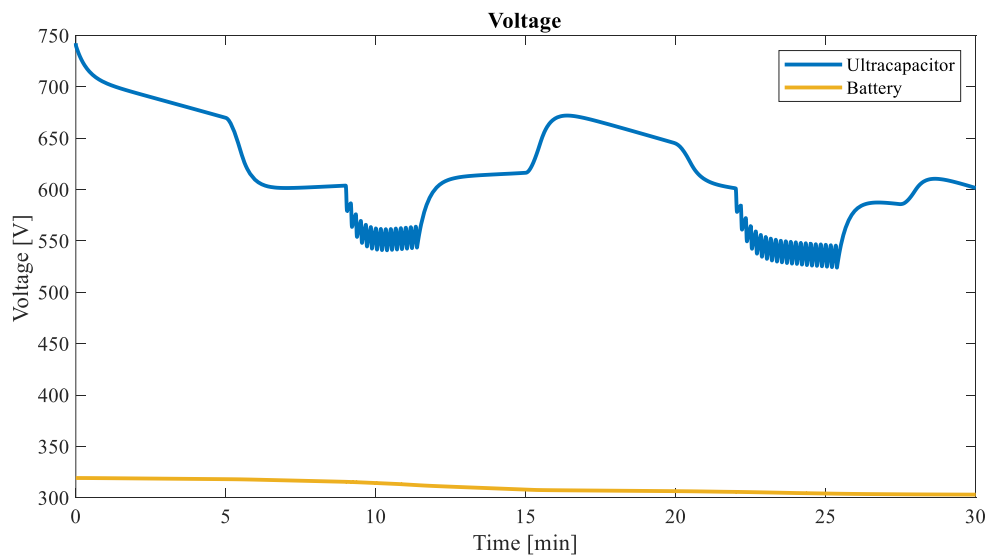
Figure 3.4 b) Voltage of energy storage elements.
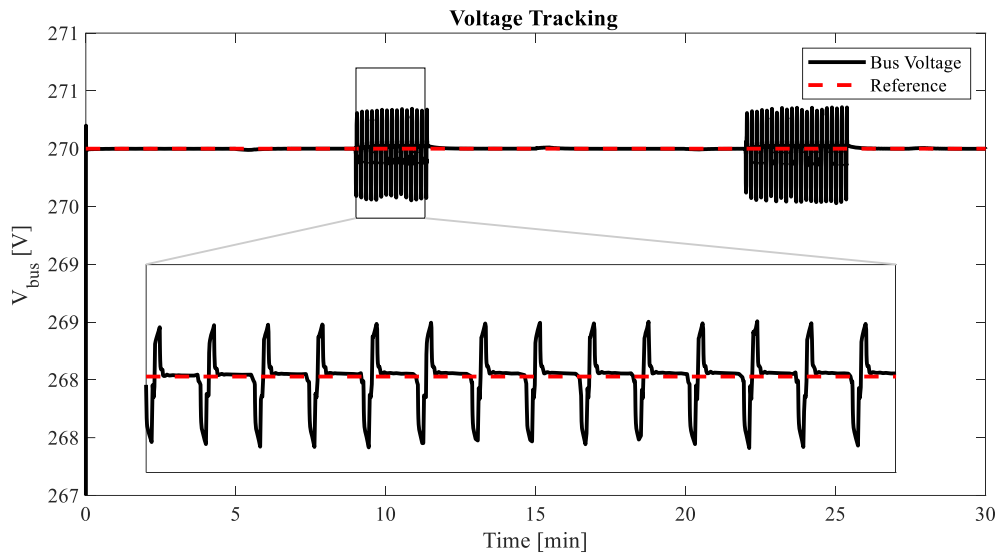
Figure 3.4 c) Bus voltage tracking performance of HESS.
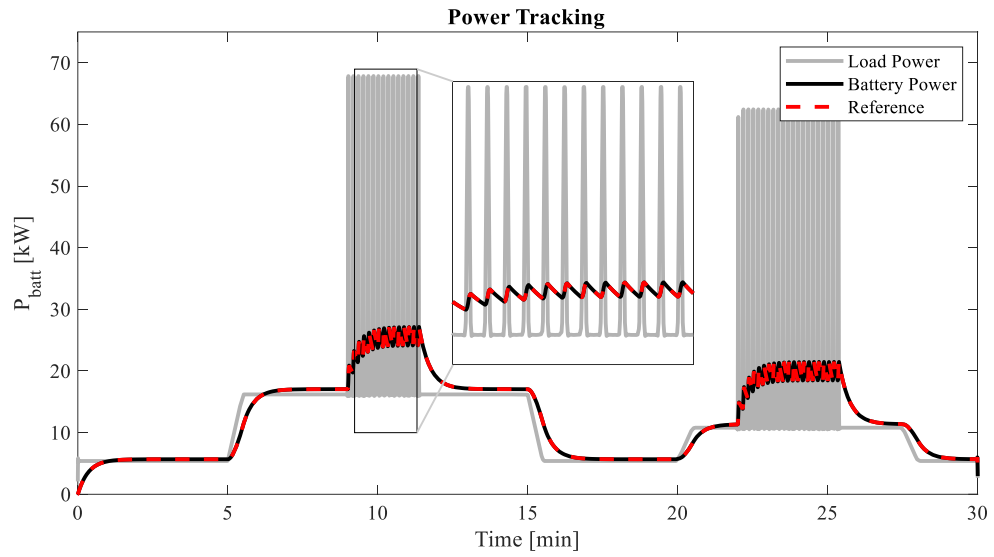
Figure 3.4 d) Battery power reference tracking performance of HESS.
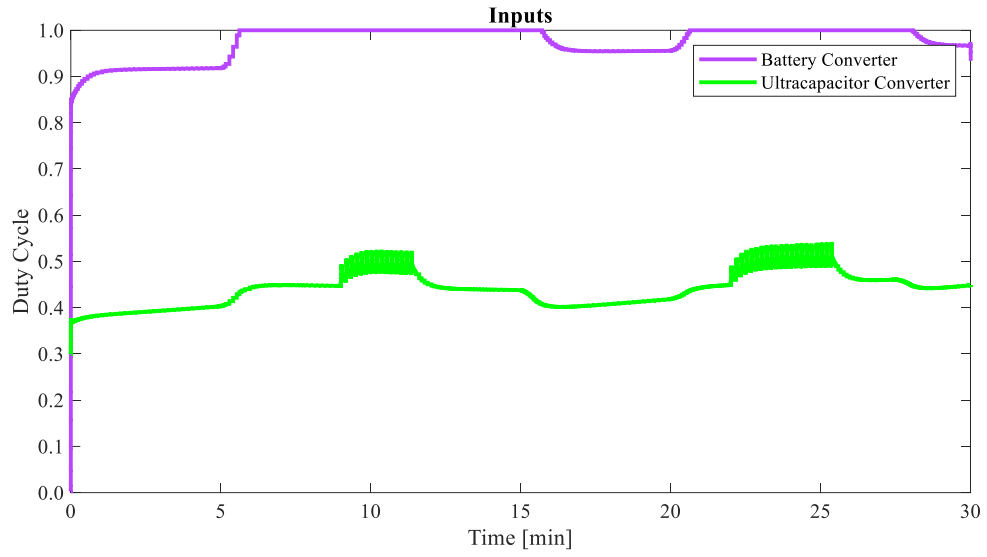
Figure 3.4 e) HESS control inputs (converter duty cycles).
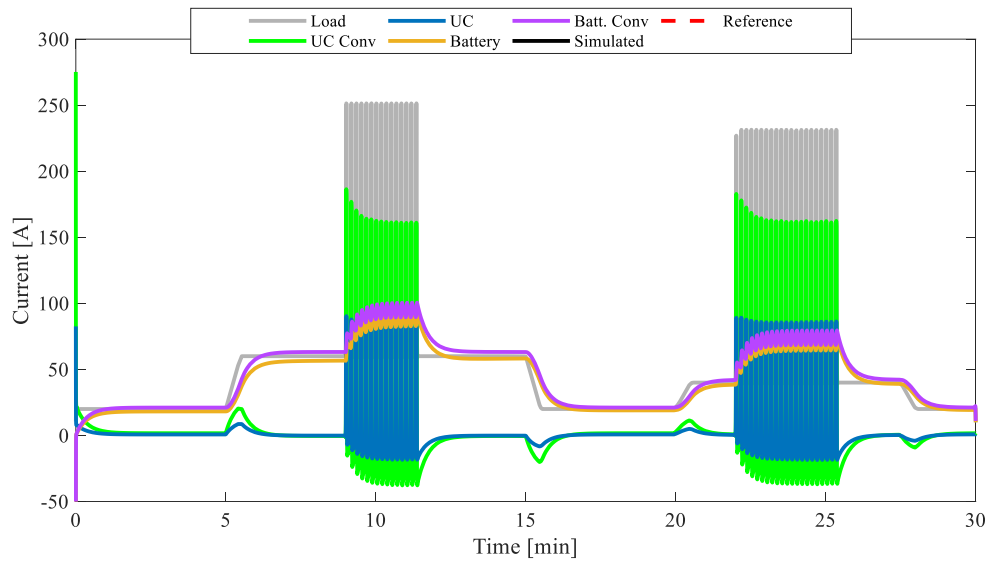
Figure 3.4 f) Currents of HESS components.

Figure 3.7: Closed-loop TESS simulation results.
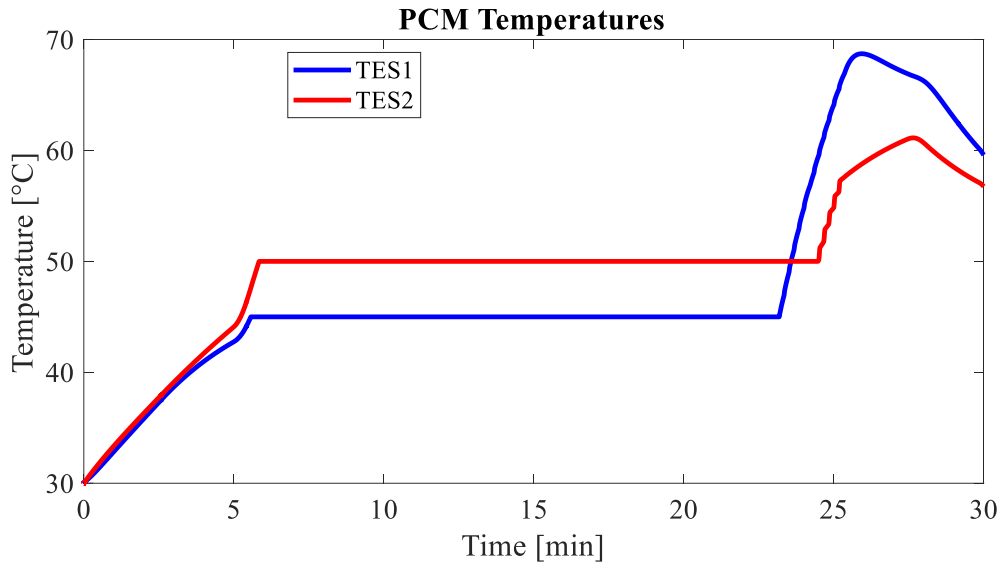
Figure 3.7 a) Temperatures of TES modules 1 and 2 in TESS.
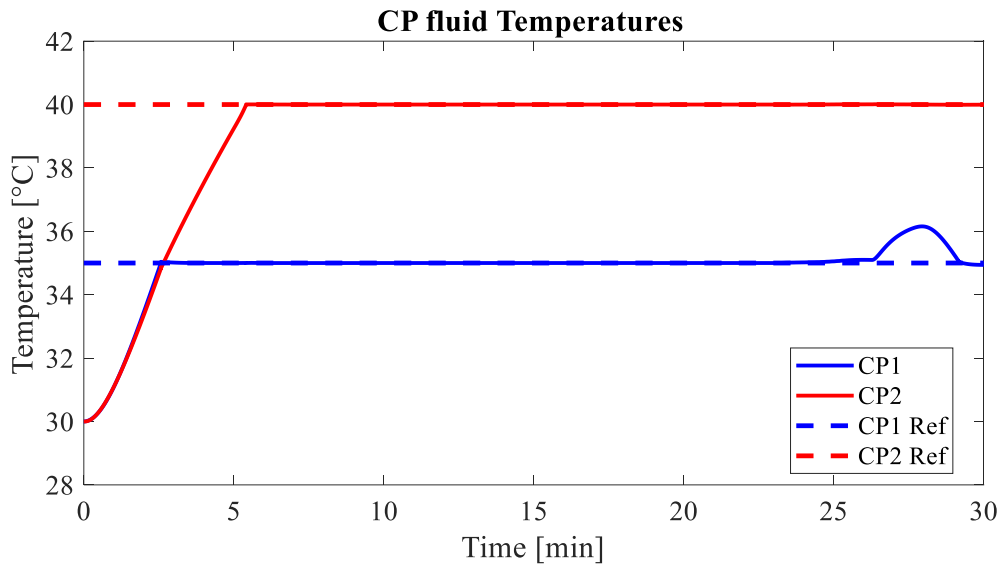
Figure 3.7 b) Fluid temperatures and reference temperatures of cold plates in TESS.
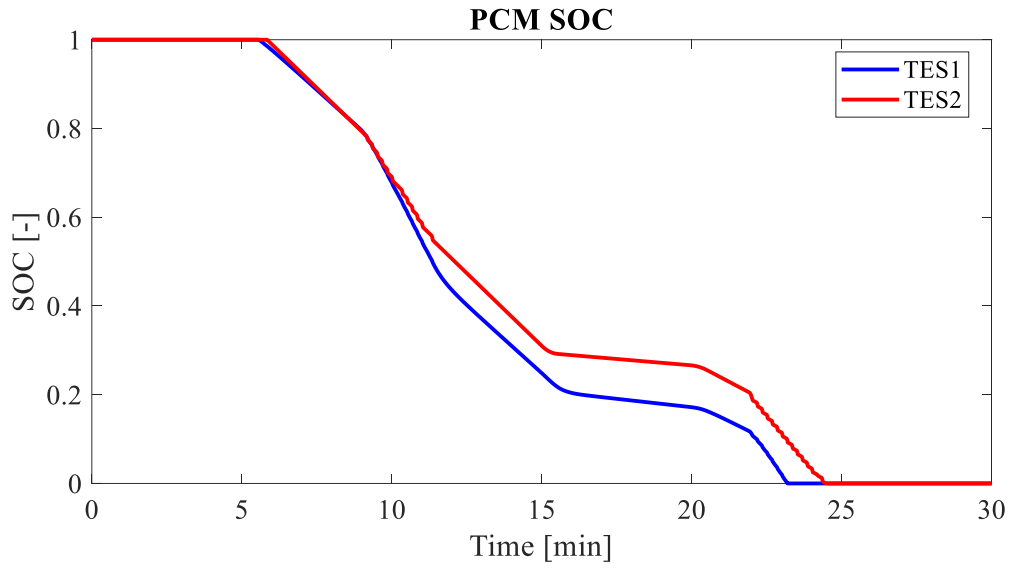
Figure 3.7 c) States of charge of PCMs in TES modules 1 and 2 in TESS.
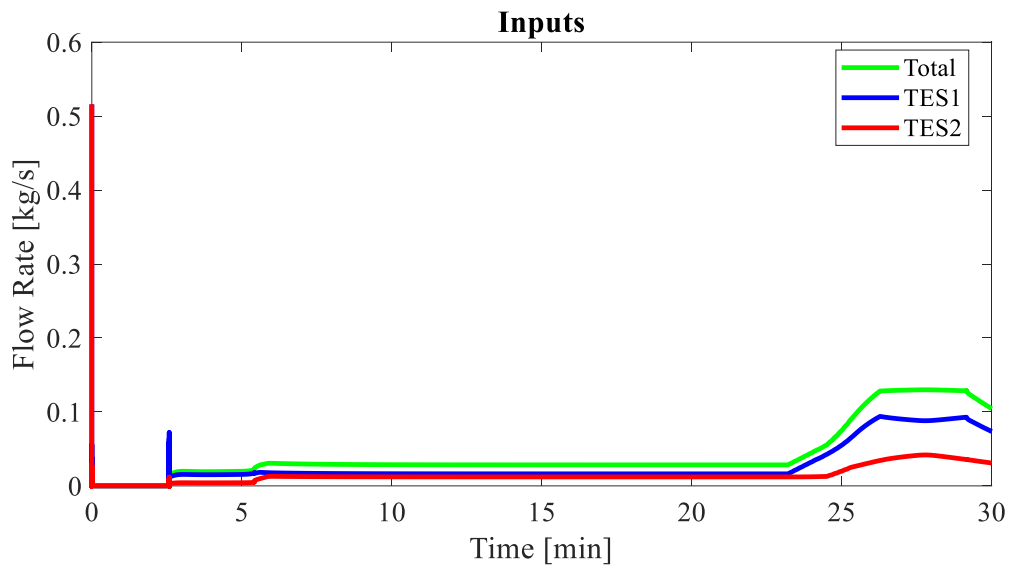
Figure 3.7 d) TESS control inputs (mass flow rates).

Figure 3.8: Closed-loop HETESS simulation results.
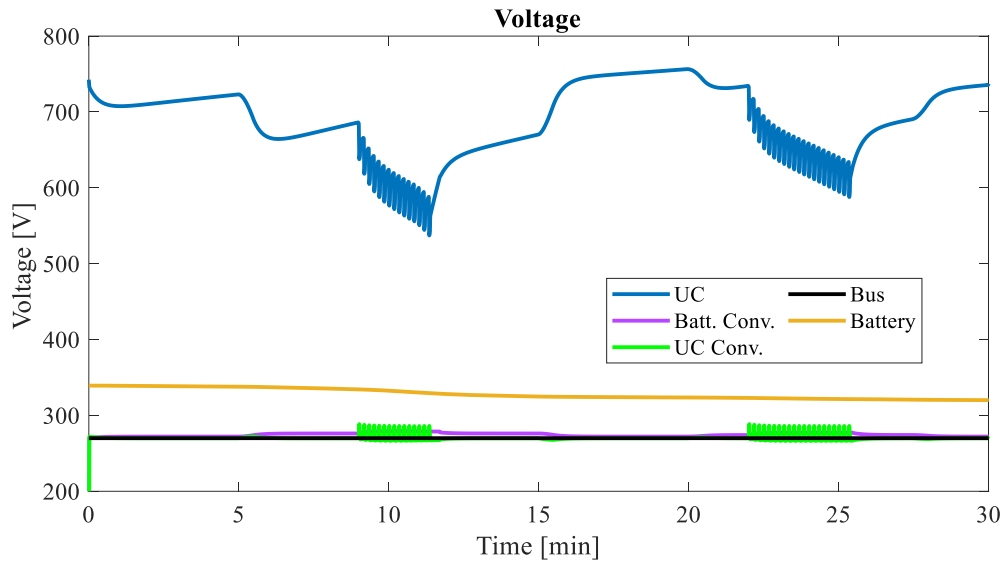
Figure 3.8 a) Voltages of electronic components in HETESS.
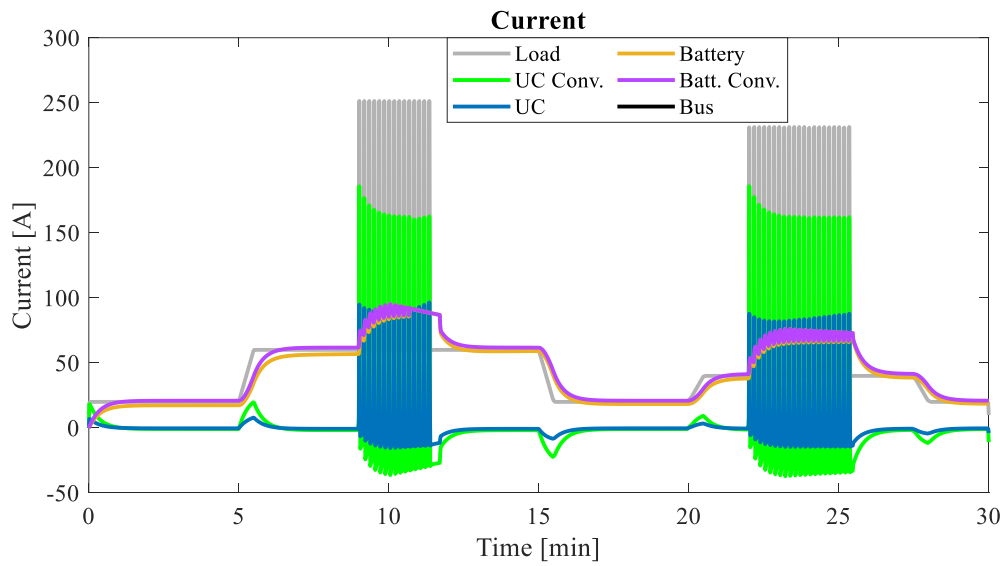
Figure 3.8 b) Currents of electronic components in HETESS.

122
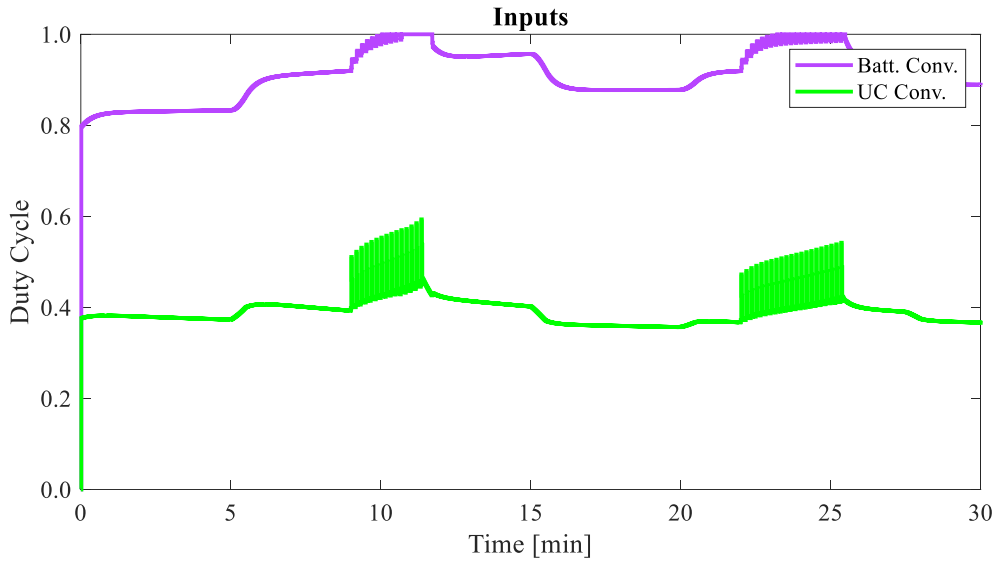
Figure 3.8 c) Converter duty cycles in HETESS.
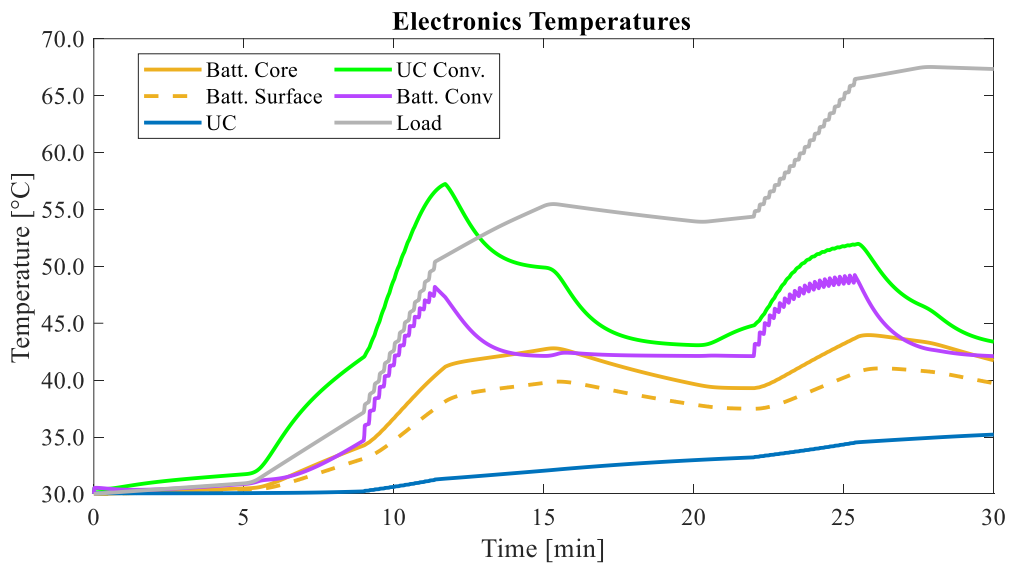
Figure 3.8 d) Temperatures of electronic components in HETESS.

123
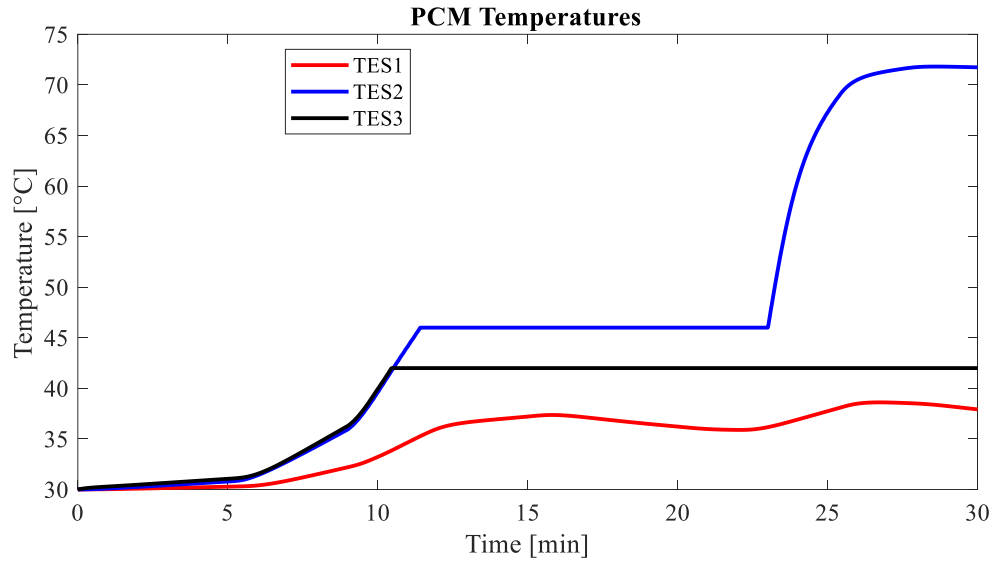
Figure 3.8 e) PCM temperatures of TES modules in HETESS.
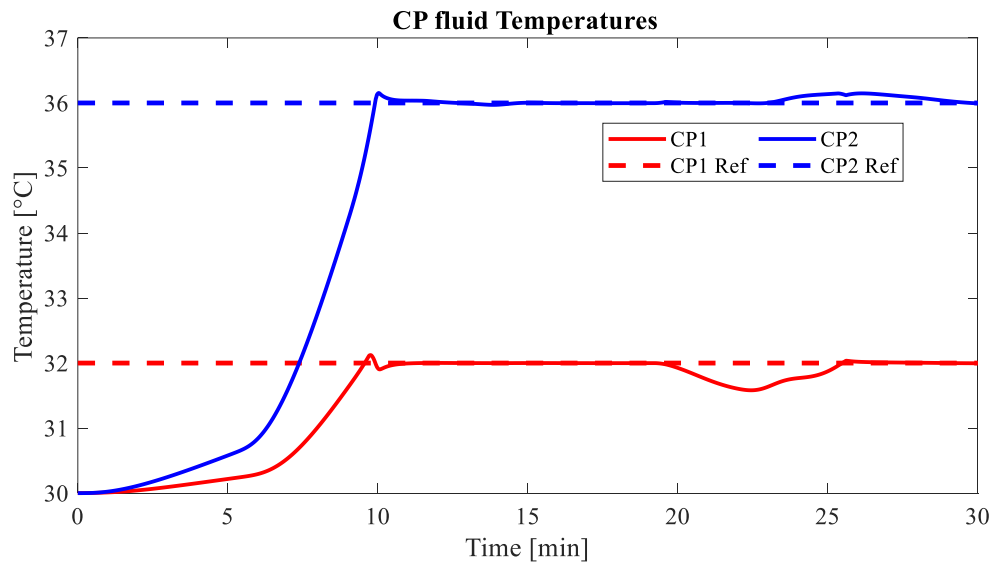
Figure 3.8 f) Fluid temperatures and reference temperatures of cold plates in HETESS.
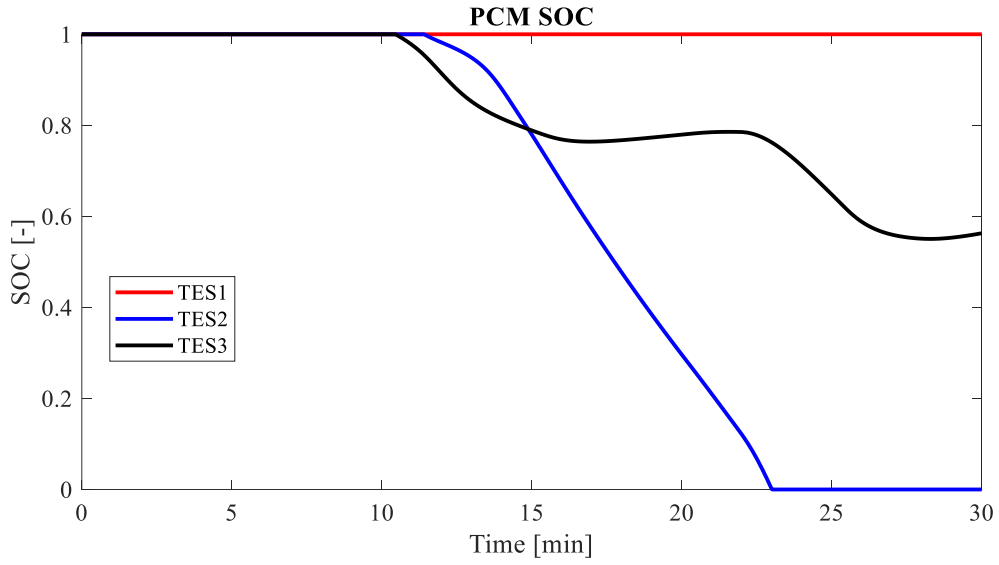
Figure 3.8 g) PCM states of charge of TES modules in HETESS.
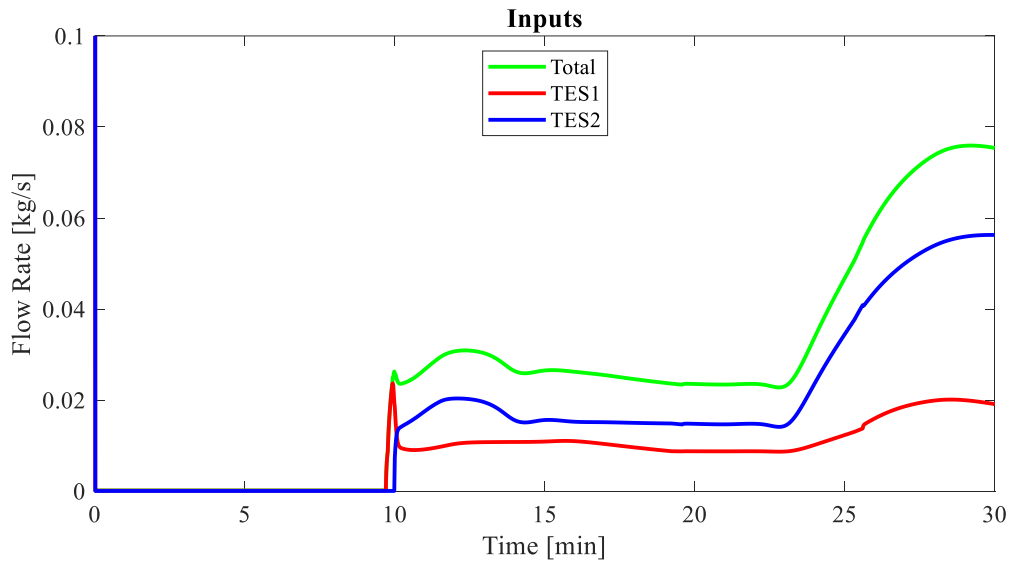
Figure 3.8 h) Flow rates in HETESS.

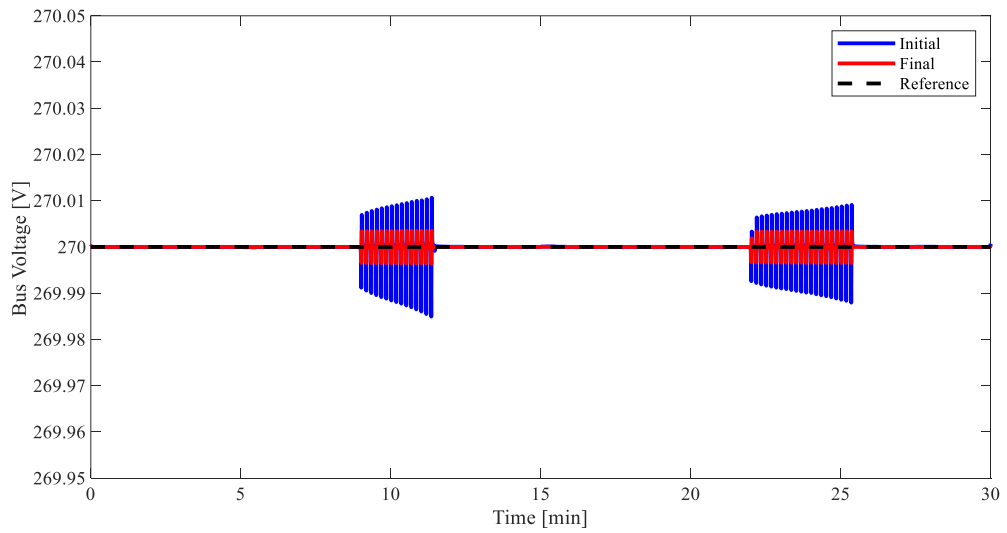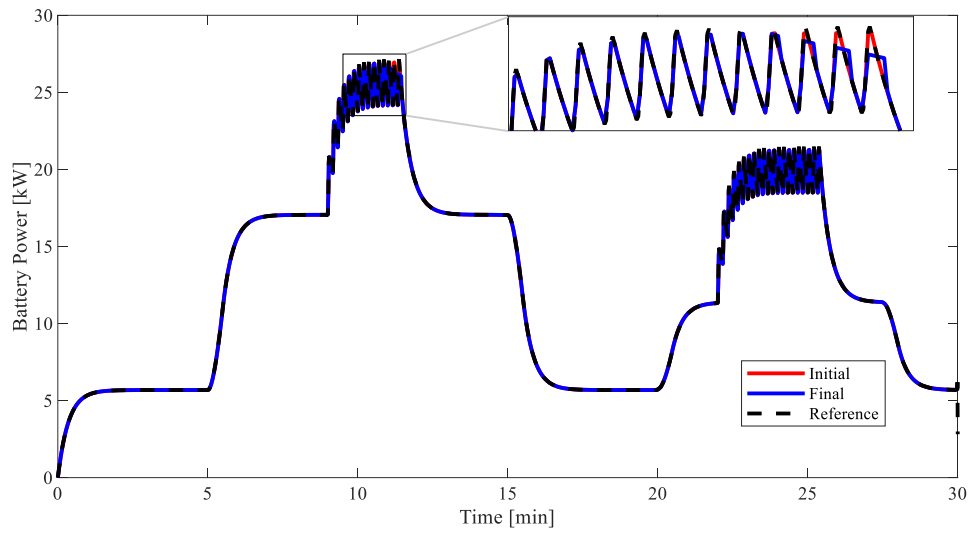**Figure 4.1: Comparison of initial and final HESS designs.**
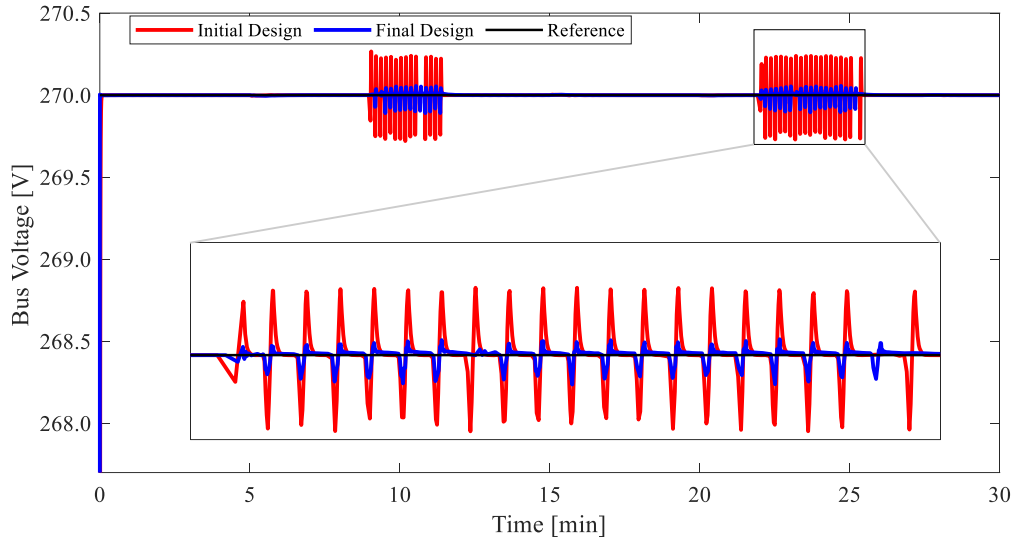
Figure 4.1 a) Comparison of voltage tracking performance of initial and final HESS designs.
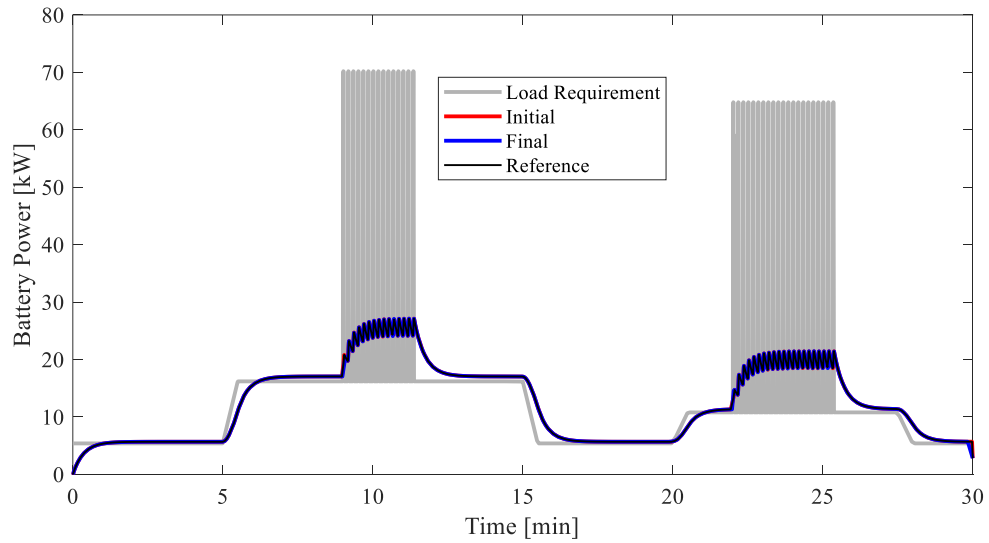
Figure 4.1 b) Comparison of battery power tracking performance of initial and final HESS designs.

**Figure 4.5: Comparison of selected trajectories of initial and final TESS designs.**
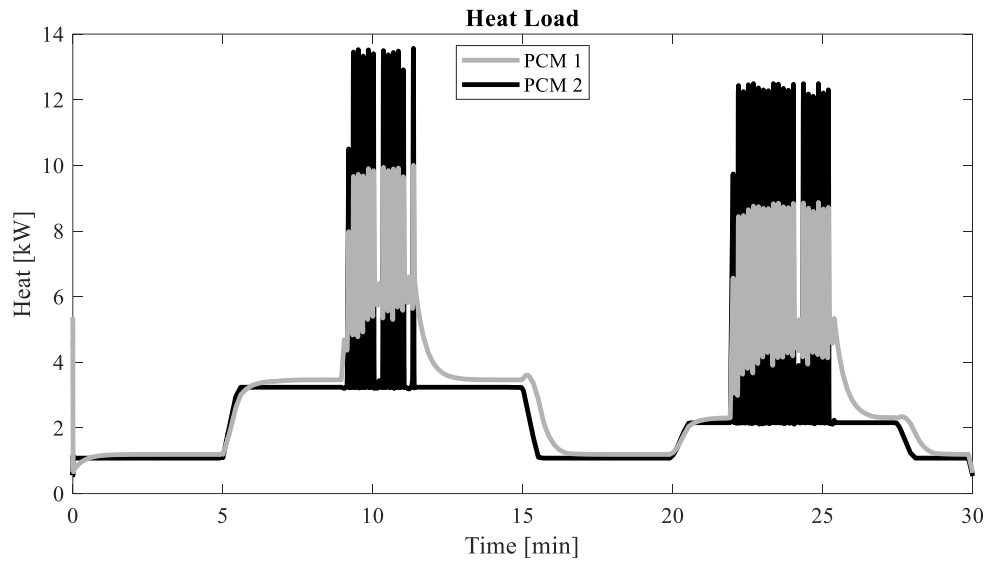
Figure 4.5 a) Heat load applied to TES modules in TESS.
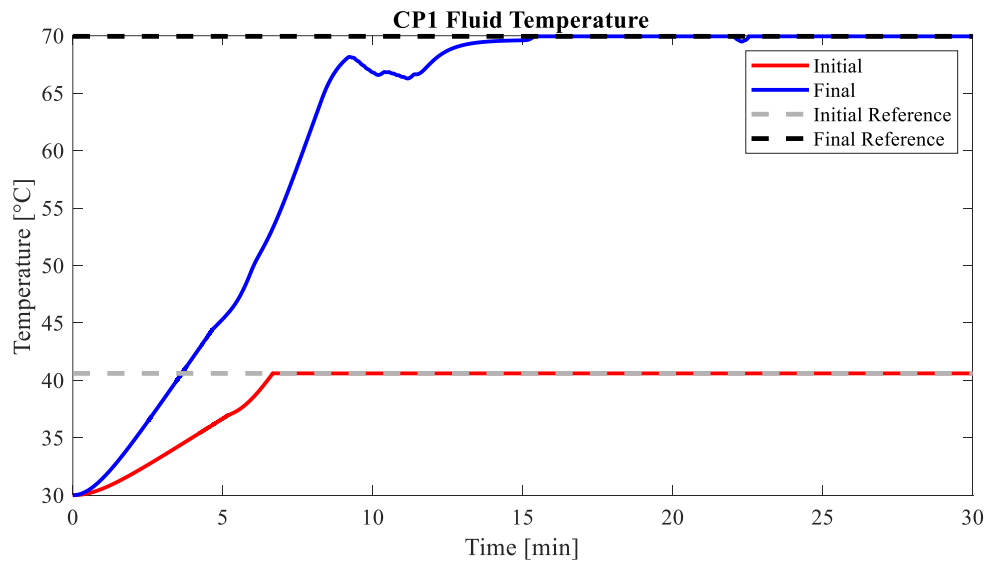
Figure 4.5 b) Cold plate 1 fluid temperature and reference temperature in initial and final TESS designs.
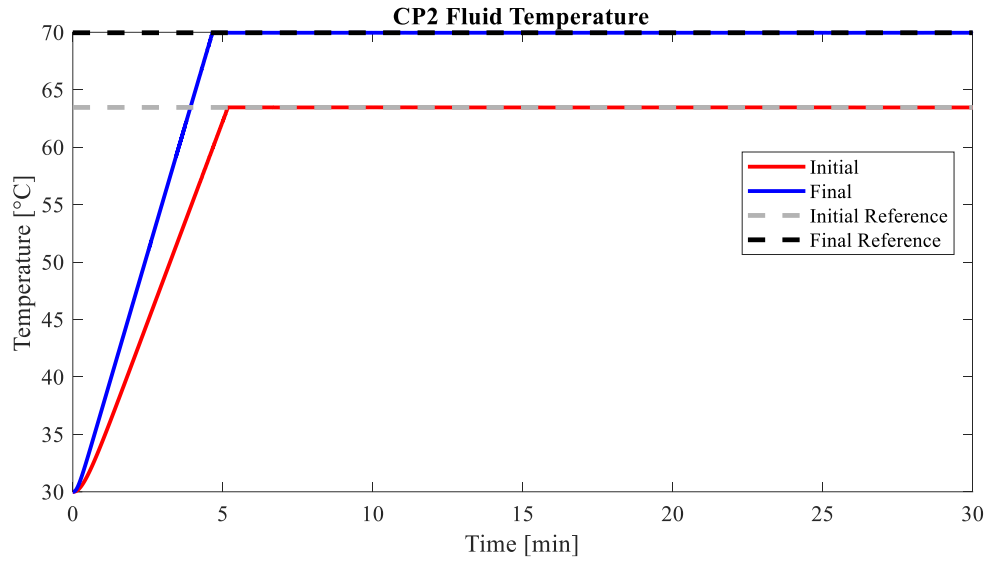
Figure 4.5 c) Cold plate 2 fluid temperature and reference temperature in initial and final TESS designs.
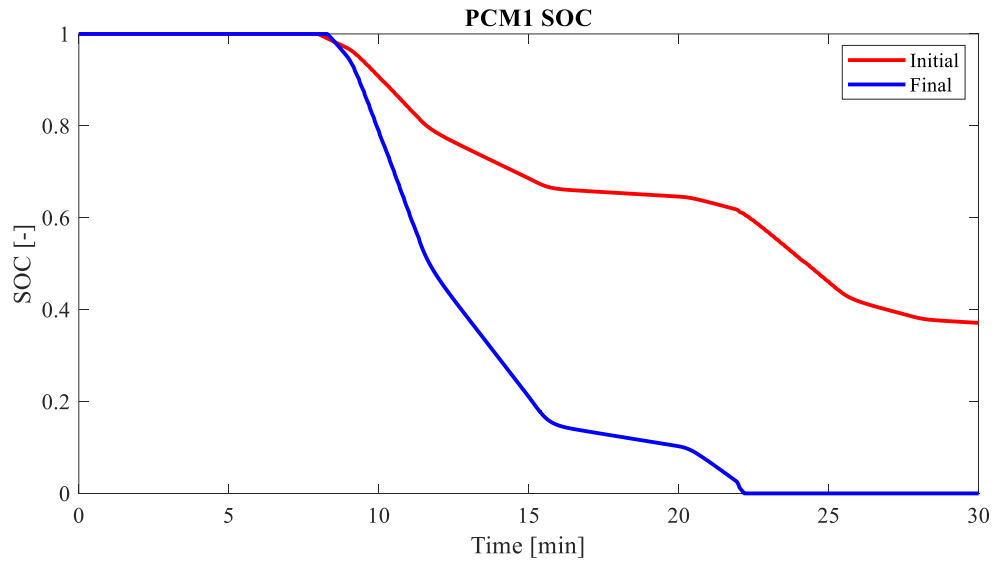
Figure 4.5 d) State of charge for PCM in TES module 1 in initial and final TESS designs.
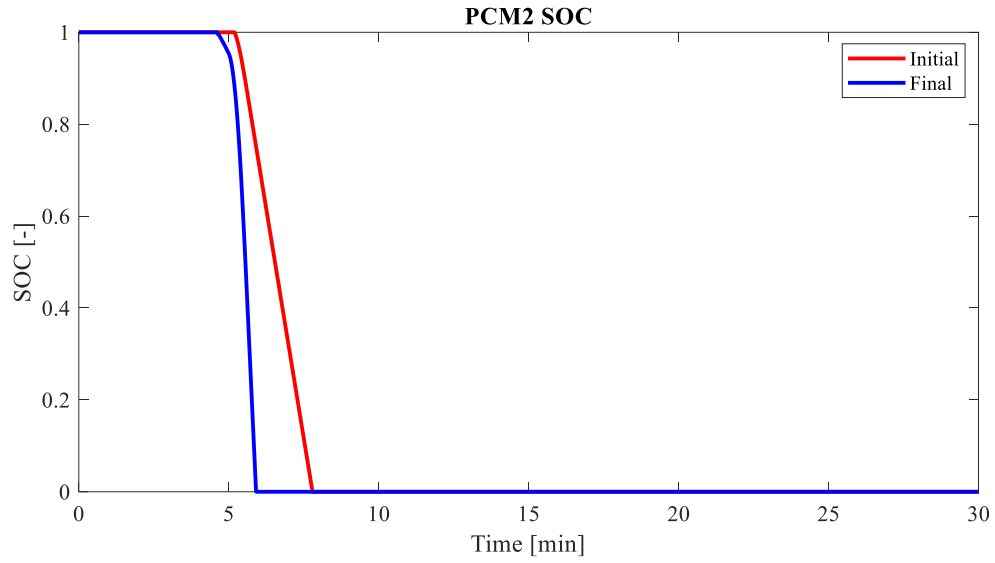
Figure 4.5 e) State of charge for PCM in TES module 2 in initial and final TESS designs.

Figure 4.8: Comparison of selected trajectories of initial and final HETESS designs.

**Figure 4.8 a) Comparison of voltage tracking performance of initial and final HETESS designs.**

Figure 4.8 b) Comparison of battery power tracking performance of initial and final HETESS designs.
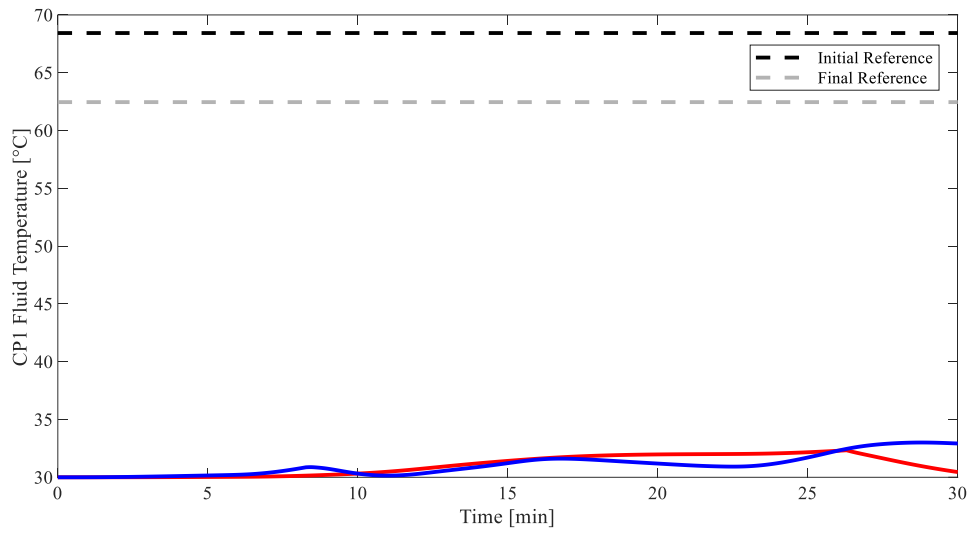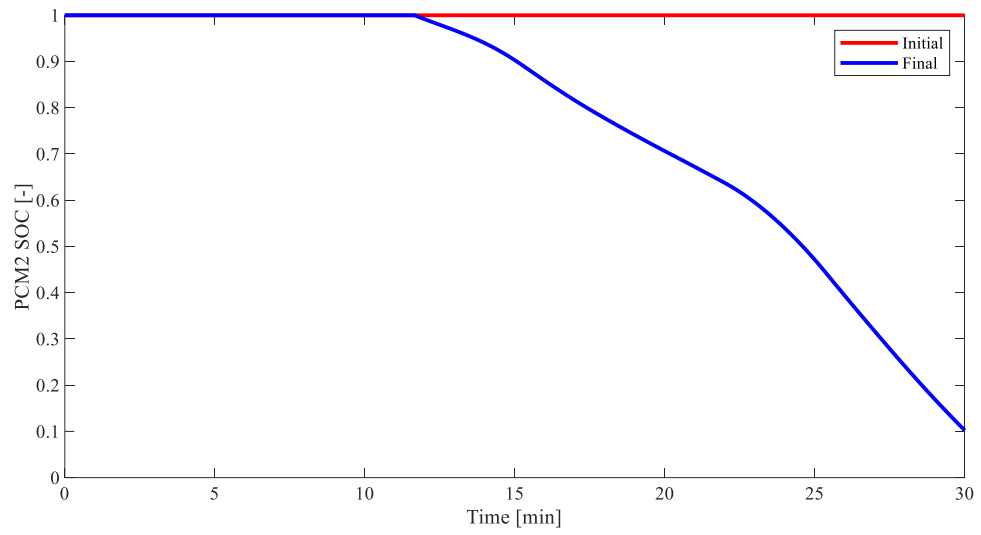

Figure 4.8 c) Cold plate 1 fluid temperature and reference temperature in initial and final HETESS designs.
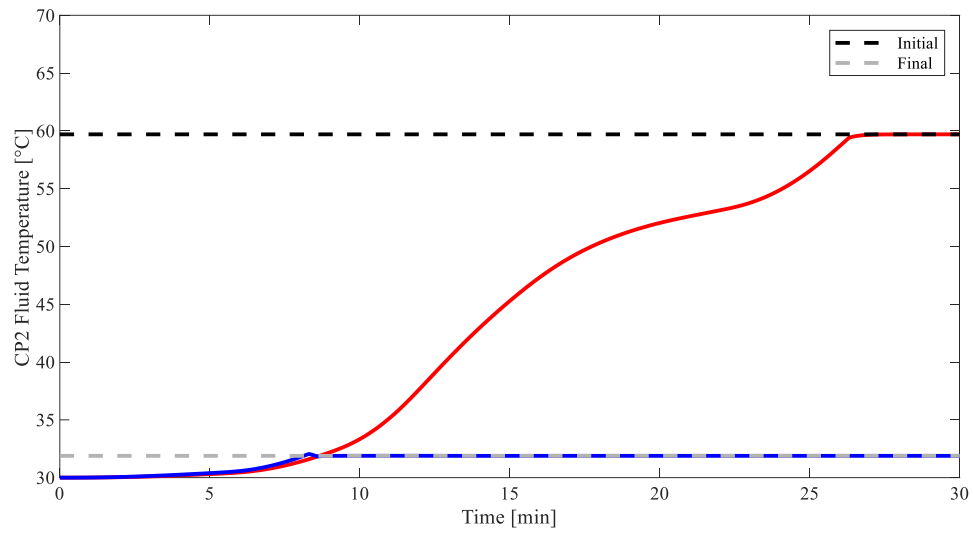
Figure 4.8 d) Cold plate 2 fluid temperature and reference temperature in initial and final HETESS designs.
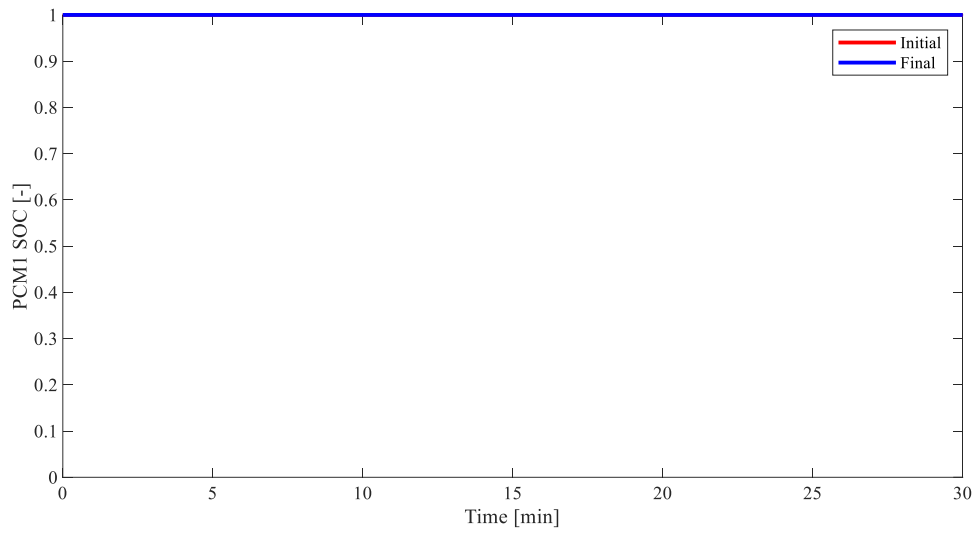
Figure 4.8 e) State of charge for PCM in TES module 1 in initial and final HETESS designs.

131

Figure 4.8 f) State of charge for PCM in TES module 2 in initial and final HETESS designs.